NORTHWESTERN UNIVERSITY

Oxides Surfaces and Novel Electronic Properties

IN PARTIAL FULFILLMENT OF THE REQUIREMENTS

SUBMITTED TO THE GRADUATE SCHOOL

for the degree

DOCTOR OF PHILOSOPHY

Field of Materials Science and Engineering

By

Pratik Koirala

EVANSTON, ILLINOIS

June 2017

ProQuest Number: 10280063

All rights reserved

INFORMATION TO ALL USERS
The quality of this reproduction is dependent upon the quality of the copy submitted.

In the unlikely event that the author did not send a complete manuscript
and there are missing pages, these will be noted. Also, if material had to be removed,
a note will indicate the deletion.

ProQuest 10280063

Published by ProQuest LLC (2017). Copyright of the Dissertation is held by the Author.

All rights reserved.
This work is protected against unauthorized copying under Title 17, United States Code
Microform Edition © ProQuest LLC.

ProQuest LLC.
789 East Eisenhower Parkway
P.O. Box 1346
Ann Arbor, MI 48106 – 1346

ProQuest Number: 10280063

All rights reserved

INFORMATION TO ALL USERS
The quality of this reproduction is dependent upon the quality of the copy submitted.

In the unlikely event that the author did not send a complete manuscript
and there are missing pages, these will be noted. Also, if material had to be removed,
a note will indicate the deletion.

ProQuest 10280063

Published by ProQuest LLC (null). Copyright of the Dissertation is held by the Author.

All rights reserved.
This work is protected against unauthorized copying under Title 17, United States Code
Microform Edition © ProQuest LLC.

ProQuest LLC.
789 East Eisenhower Parkway
P.O. Box 1346
Ann Arbor, MI 48106 – 1346

© Copyright by Pratik Koirala 2017

All Rights Reserved

ABSTRACT

Oxides Surfaces and Novel Electronic Properties

Pratik Koirala

The scope of this thesis extends to the study of surface structures and electronic properties in a number of complex oxides. The c(6×2) surface reconstruction on $SrTiO_3$ (001) was solved using a combination of plan view transmission electron microscopy imaging, atomic resolution secondary electron imaging, and density functional theory calculations. This work provided fundamental insights on the effects of dielectric screening in secondary electron generation. A thorough analysis on the limitation and functionality of transmission plan view imaging showed that the kinematical approximations used in the separation of top and bottom surfaces is only valid in thin samples ($\sim$ 5 nm or less for $SrTiO_3$). The presence of an inversion center in the surface structure also made separation of the top and bottom surfaces more robust.

Surface studies of two other oxides, $KTaO_3$ and $NdGaO_3$, provided understanding on the mechanism of surface heterogeneity and segregation. In the case of $KTaO_3$, selective ion sputtering and the loss of K resulted in large stoichiometric variations at the surface. Annealing of such samples led to the formation of a potassium deficient tetragonal phase ($K_6Ta_{10.8}O_{30}$) on the surface. A similar phenomenon was also observed in $NdGaO_3$.

Exploratory surface studies of the rare earth scandates ($ReScO_3$, Re = Gd, Tb, Dy) led to the observation of large flexoelectric bending inside an electron microscope. Thin rods of these scandates bent by up to 90° under a focused electron beam; the bending was fully reversible. Ex-situ measurements of flexoelectric coefficient performed by another graduate student, Christopher Mizzi, confirmed that the scandates have a large flexocoupling voltage (∼42 V).

Electronic structure of the lanthanide scandates was studied using temperature dependent X-ray photoelectron spectroscopy and hybrid density functional theory calculations. The amount of charging under X-ray illumination was greatly reduced with increasing temperature owing to the presence of oxygen vacancies and surface band gap reduction. These results also indicated that the 4f-electrons are active components of the valence band electronic structure. We believe that the lanthanide scandates are a rich playground of material properties and have potential for applications in electronic and nano-mechanical devices.

Approved by

Professor Laurence D. Marks

Department of Materials Science and Engineering

Northwestern University, Evanston, IL 60208, U.S.A.

Acknowledgements

First and foremost, I would like to acknowledge Laurie for his guidance and support over the years. He has not only been an adviser, a mentor but a role model; his passion for science pushed me to do my best. He has supported my scientific curiosity while challenging my ideas as the biggest critique and admirer. I am extremely grateful to my thesis committee - Prof. Peter Voorhees, Prof. James Rondinelli, Prof. Amanda Petford-Long, Dr. Dillon Fong and Dr. Jim Ciston for the engaged scientific discussion that has provided my work different perspectives.

A special thanks to all the past and present members of the Marks group: Yuyuan and Betty for getting me started on sample preparation and electron microscopy; Dr. Jim Ciston for collaboration on plan view imaging of oxide surfaces; Chuandao for collaboration on $SrTiO_3$; Danielle for collaboration on $LaAlO_3$; Lawrence for being an awesome friend, colleague and a computer guru who has rescued me many times; Ahmet for long nights on the JOEL ARM and all the help ; Chris for collaboration on all things DSO; Xiaoxiang, Say and Tassie for their help with DFT and experiments on the synchrotron beam line at the Advanced Photon Source; Emily and Yifeng for introducing me to the group. I also wish the younger members, Ryan, Chris, Tiffany, Alex and Zach all the best in their careers.

I would also like to thank Dr. Yimei Zhu and Prof. Amanda Petford-Long for hosting me at Brookhaven National Lab and Argonne National Lab, respectively, and providing me access to their low field JEOL2100F microscopes. This was critical in ruling out magnetic contributions to the observed bending in lanthanide scandates.

I would like to thank the staff at the Electron Probe Instrumentation Center (EPIC) at Northwestern University for their help with instruments and sample preparation. Dr. Jinsong Wu and Wenyun Li have provided me with any help I needed, be it in finding the right slurry to polish my samples or in troubleshooting almost every sample preparation equipment that tended to break ever so often. I would also like to thank Xinqi Chen at the KECK center for his continued help with the XPS system and letting me explore the capabilities of the system without imposing many rules!!

Above all, I can not thank my parents enough for who I am today. They have supported me at all times and stood firm by any decision that I have made. I would especially like to thank my dad for engaging me in mathematical reasoning at a very young age and letting me play with his fancy civil engineering tools.

I would also like to officially thank my funding. Majority of the work that was done as a part of this thesis was supported by the U.S. Department of Energy, Office of Basic Energy Sciences, Division of Materials Sciences and Engineering under grant number DE-FG02-01ER45945. Part of the work was also supported by the National Science Foundation under grant number DMR-1507101.

List of Abbreviations

ABF: annular bright field.

AES: auger electron spectroscopy.

AFM: atomic force microscopy.

ARPES: angle resolved X-ray photoelectron spectroscopy.

BF: bright field.

BHF: buffered hydrogen fluoride.

DF: dark field.

DFT: density functional theory.

DM: direct methods.

EDM: Electron Direct Methods.

EDS: energy-dispersive X-ray spectroscopy.

FFT: fast fourier transform.

GGA: generalized gradient approximation.

HAADF: high angle annular dark field.

HREM: high resolution electron microscopy.

HRSEM: high resolution secondary electron microscopy.

LAADF: low angle annular dark field.

LDA: local density approximation.

LEED: low energy electron diffraction.

LEIS: low energy ion scattering.

MTF: modulation transfer function.

REELS: reflection electron energy loss spectroscopy.

RHEED: reflection high energy electron diffraction.

SEM: scanning electron microscopy.

STEM: scanning transmission electron microscopy.

STM: scanning tunneling microscopy.

TED: transmission electron diffraction.

TEM: transmission electron microscopy.

UHV: ultra high vacuum.

UPS: ultraviolet photoelectron spectroscopy.

XPS: X-ray photoelectron spectroscopy.

XRD: X-ray diffraction.

Table of Contents

List of Tables

List of Figures

CHAPTER 1

Introduction

1.1. Background

Transition metal oxides are an interesting class of materials with a broad spectrum of structures and properties. The nature of metal-oxygen bonding can range from ionic to highly covalent [1]. The physics of these materials can be even more exotic because of the presence of d- and f-electrons which give rise to correlated electron interactions [2]. A sub-class of these oxides is the perovskite family. The lattice parameters and crystal structures of perovskites span a wide range and can be used for strain engineering of materials properties [3]. Perovskites are ABO_3 compounds, where A and B are cations and O is the anion. A prototypical oxide of this class is $SrTiO_3$, which has a cubic structure with corner sharing TiO_6 octahedral units. Depending on the choice of A and B there can be distortions such as the deviation of either the B site from the center of the octahedral unit or the oxygen atoms from the face centers. The amount of distortion for a given perovskite can be approximated using the Goldschmidt tolerance factor (t) [4] defined by equation 1.1.

$$t = \frac{r_A + r_O}{\sqrt{2}(r_B + r_O)} \tag{1.1}$$

where, r_A is the radius of the A-cation, r_B is the radius of the B-cation and r_O is the radius of oxygen. A cubic structure is favorable at tolerance values between 0.9 and 1. Tolerance values larger than 1 lead to hexagonal or tetragonal crystal structures and values less than 0.9 lead to orthorhombic or rhombohedral structures. Distortions in the crystal structure can also break inversion symmetry, giving rise to interesting structural and electronic phenomena such as ferroelectricity which is observed in a number of materials including $BaTiO_3$ [5] and $PbTiO_3$ [6].

The bulk crystal structure and electronic properties of these materials have been routinely studied. In contrast, surface structure and electronic properties have not received appropriate attention. Most studies assume bulk termination or a simple (1×1) reconstruction which only provides the lattice parameter for growth. The abundance of surface reconstructions observed on the prototypical perovskite, $SrTiO_3$ [7–12], indicate that these assumptions are incorrect. Understanding surface structures requires properly addressing the topics of surface chemistry, coordination environment, thermodynamics, valence and charge densities.

Nomenclature of surface reconstructions is assigned using Wood's notation. For instance, a (m×n) reconstruction implies a surface unit cell that is m and n times larger

than the bulk unit cell along the two in-plane lattice vectors. Similarly, the (n×1) homologous series on the $SrTiO_3$ (110) surface can be viewed as the ordering of corner sharing TiO_4 tetrahedral units on the surface. The number of tetrahedra in one direction is n (n = 2, 3, 4, 5, 6, ∞), and the periodicity in the orthogonal direction is same as the underlying bulk (see Figure 1.1).

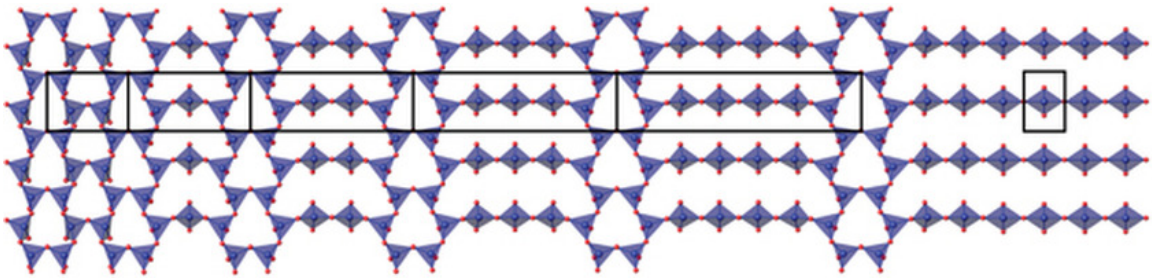

Figure 1.1. The surface structures of calculated members of the homologous series of (n×1) surface structures viewed perpendicular to the surface. For clarity, the bulk is omitted. TiO_4 tetrahedra are shown in blue, with anions in red. Unit cells are outlined in black; from left to right n=2, 3, 4, 5, 6, ∞ (Adapted from Ref. [13])

Many of these perovskite oxides are polar along different crystal directions. Although most papers in literature have modeled complex oxide surfaces as dipole with a fully ionic treatment of different atoms, the actual mechanism is much more complicated and requires the incorporation of more accurate charge densities. Parametrization of charge density from simple variables such as bond lengths and coordination is much better than one obtained from a neutral atom model [14]. There could also be several competing mechanisms such as nano-faceting, large stoichiometric variations, adsorption, surface reconstructions and phase segregation. Thus, a simple bulk truncation is highly unlikely.

Surface reconstructions are known to occur in many systems and drive the surface to a valence neutral state i.e. the sum of formal valence of all layers including the two surfaces and bulk is zero [7, 9–11]. These surface structures can be quite different from the corresponding bulk and have been known to exhibit unique structural and electronic properties [15, 16]. In addition to changes in epitaxy, surface reconstructions also alter the surface chemistry and resulting properties.

1.2. Motivation and Scope

Transition metal oxides have applications in many areas including optoelectronics [17], catalysis [18] and superconductivity [19]. Oxides materials are also widely used as substrates for the growth of other complex oxides [3] and noble metal nanoparticles [20]. For most applications, it is critical to understand the interactions at the interface [20, 21]. For thin film growth, substrate interfacial structure drives epitaxy and electronic properties. The widely known example of the $SrTiO_3/LaAlO_3$ [21] interfacial 2D electron gas emphasizes the importance of surface and interface structure. The 2D electron gas is only observed when the interface layers are TiO_2 and LaO. Oxygen vacancies also play an important role as charge carriers at the interface in these observations [22]. Similarly, the breaking of symmetry at the surface can lead to unique phenomena such as the surface piezoelectric effect [23]. As in the case of surface structure, electronic properties at surfaces have been largely unexplored. With better understanding, materials properties can be tailored for desired applications.

The scope of this thesis extends to the study of both structure and electronic properties of complex oxide surfaces. Complex surface structures and dynamics of segregation and vaporization were studied in $SrTiO_3$, $LaAlO_3$, $KTaO_3$, $NdGaO_3$ and $RScO_3$ (R = Tb, Gd, Dy). Exploratory surface studies conducted on the rare earth scandates led to the discovery of large flexoelectric response, even though the general consensus in the field has assumed that $DyScO_3$ would not have a large flexo-response owing to its relatively small dielectric constant (24 at room temperature). The implication of surface structure on the electronic properties of $RScO_3$ was also explored.

1.3. Organization

The thesis is organized with experimental and theoretical methods in Chapters 2. The results and analysis are presented in subsequent chapters. Details of the c(6×2) surface reconstruction on $SrTiO_3$ (001) are presented in Chapter 3 with plan view high resolution electron microscopy (HREM) and HRSEM imaging. The details of the functionality and limitations of plan view image analysis are presented in Chapter 4. In addition to surface reconstructions, there are other competing processes at the surface which result in surface heterogeneity and phase segregation. Surface dynamics of $KTaO_3$ and $NdGaO_3$ are presented in Chapters 5 and 6, respectively. Implications of surface structure on flexoelectric response are presented in Chapter 7. Finally, two ongoing projects and future directions are discussed in Chapter 8.

CHAPTER 2

Methods

A wide range of experimental and theoretical methods were used as a part of this work. The details of sample preparation, experimental characterization and theoretical methods are discussed in this chapter.

2.1. Experimental

2.1.1. Sample Preparation

Transmission electron microscopy (TEM) samples were made using the conventional method illustrated in Figure 2.1. Commercially available single crystalline substrates of dimensions 10mm $\times$ 10mm $\times$ 0.5mm were cut into 3 mm discs with a rotary disc cutter. These discs were then mechanically polished to a thickness of 120 μm using silicon carbide sandpaper and dimpled to a thickness of 5 μm at the center with a Gatan 656 Dimple Grinder and 0.5 μm diamond slurry. Finally, these samples were thinned using a Gatan Precision Ion Polishing System with $3-4.5$ keV Ar^+ ions at $10-30$ μA for $1-4$ hours to electron transparency. The milling angle was gradually decreased from 10° during initial milling to 4° for final polishing. Electron transparency was determined by using an optical microscope to identify the occurrence of a hole at the center (see Figure 2.2). Newton

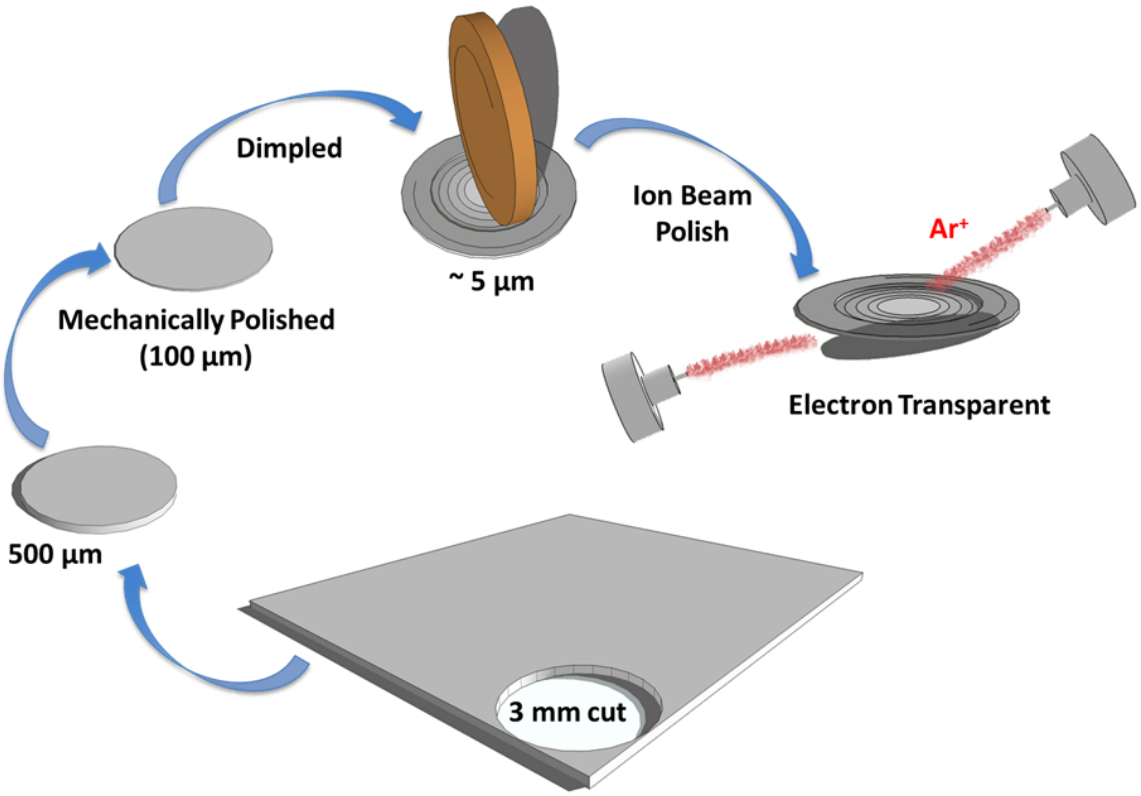

Figure 2.1. Schematic illustration of TEM sample preparation involving steps of cutting, polishing, dimpling and ion milling.

rings observed in the optical image (Figure 2.2) in some areas of the sample indicate thin areas suited for TEM analysis.

Besides the conventional sample preparation technique and cleaning procedure of ultrasonication in acetone and ethanol, wet chemical etching was used to obtain clean and crystalline samples. The etching solution was a mixture of commercially available buffered hydrogen fluoride (BHF) [24] and hydrogen peroxide(H_2O_2), 5:1 by volume. This method

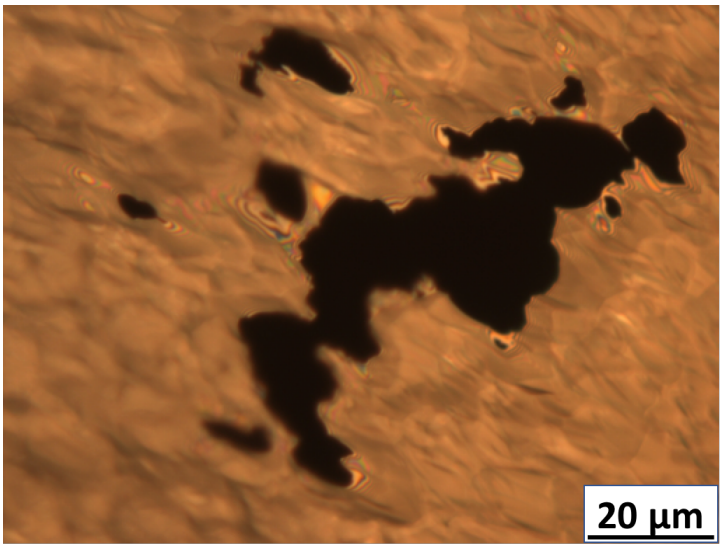

Figure 2.2. Optical image of hole in a TEM sample after ion beam milling. Areas around the hole show Newton's ring of different colors under unpolarized light.

was found to be highly effective in removing surface contamination and amorphous materials on the surface. HREM images of the sample in Figure 2.3 before and after etching show significant reduction in strain and surface damage after etching. This etching solution is known to produce TiO_2 terminated surface on $SrTiO_3$ (001).

These etched samples were annealed for surface recrystallization and ordering. Oxide samples undergo radiation damage during Ar^+ ion milling. Annealing under oxidizing condition will replenish oxygen vacancies and promote surface recrystallization. Annealing was usually done at ambient pressure or in flowing dry oxygen environment. Temperature was ramped from room temperature to $1050-1300^\circ$ at 5°C/min and held for $0.5-12$ hours. The dwell time is varied depending on the extent of surface damage and

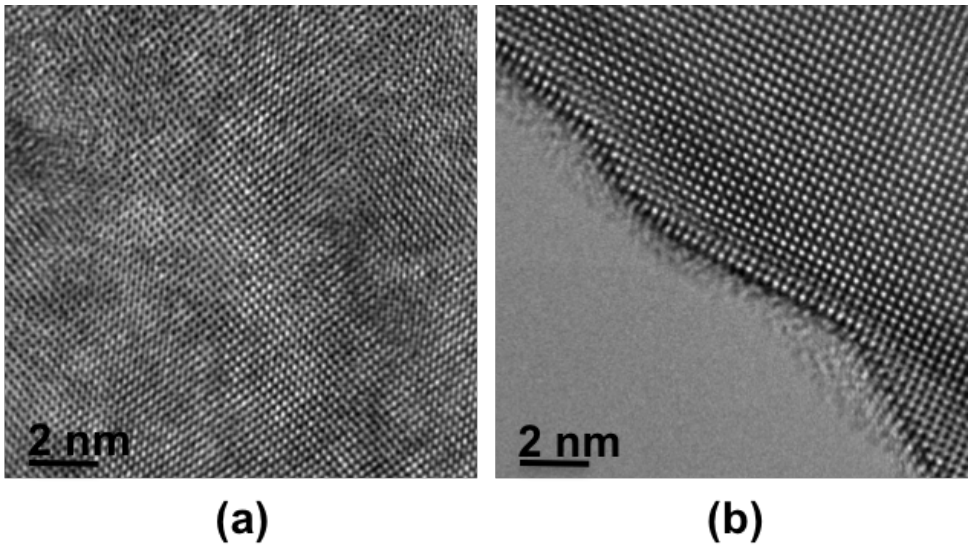

Figure 2.3. HREM image of (001) oriented $SrTiO_3$ after ion milling in (a) and after subsequent wet chemical etching in (b).

surface termination. The (110) termination of $SrTiO_3$ required an additional second dwell at a lower temperature (∼600°C) for surface ordering.

2.1.2. Electron Microscopy

High energy electrons have wavelengths smaller than even the H atom. Interactions of such high energy incident electrons and materials provide information on the crystal and electronic structure. The diffractive nature of these interactions can be used to determine the lattice, atomic structure, defects as well as chemical signatures that are specific to elements and local bonding environment. The multitude of signals that arise from electron specimen interactions are in the form of scattered electrons and radiation, from both elastic and inelastic interactions. A schematic of electron-specimen interactions is given in Figure 2.4. Secondary electrons are surface sensitive and can be used for

atomic resolution imaging [8]. Back scattered electrons provide surface topographical information. Characteristic X-ray signal can be used for elemental analysis. Similarly, electrons that have transmitted through the sample (both elastic and inelastic) provide information on crystal structure, bulk defects and energy loss events that are signatures of specific elements and bonding environments.

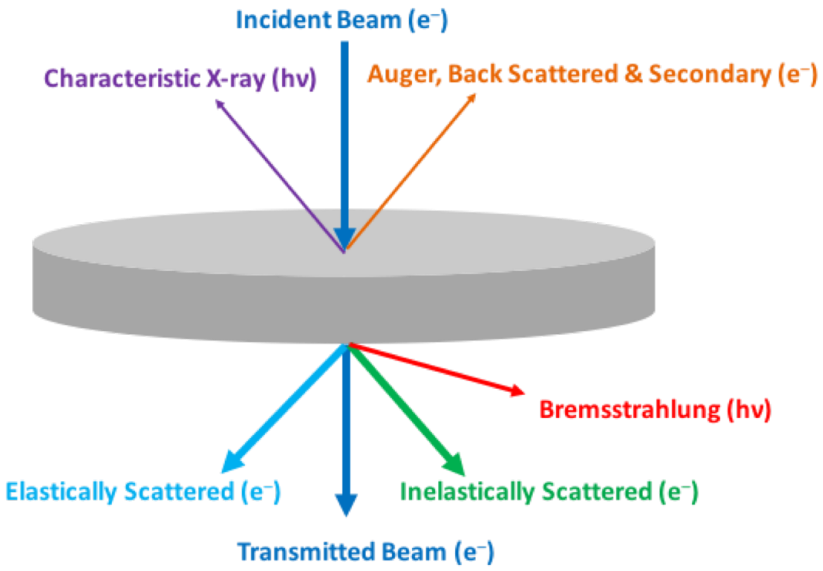

Figure 2.4. Electron-specimen interaction and the resulting signals.

TEM is one of the most effective characterization techniques as it provides simultaneous access to a multitude of signals discussed before. Results presented in this thesis are from the use of conventional bright field (BF), dark field (DF), transmission electron diffraction (TED), HREM in conjunction with chemical analysis using energy-dispersive X-ray spectroscopy (EDS). BF images are obtained by selecting the direct beam in the back focal plane using the objective aperture. In dark field imaging, a specific diffracted

beam in the back focal plane is used to form an image. HREM on the other hand is formed by many beams hence the image is rich in phase contrast resulting from the interaction of many beams. The details of HREM imaging are discussed in later chapters in the context of plan view imaging of surfaces. These imaging techniques are complementary for the study of surfaces.

Characterization was done using the Hitachi H8100, Hitachi HD2300 STEM, JEOL 2100F, JEOL ARM-200CF. The HRSEM experiments were performed at Brookhaven National Lab using the aberration corrected Hitachi 2700C STEM by Dr. Jim Ciston.

2.1.3. X-ray Photoelectron Spectroscopy (XPS)

XPS is a technique that uses the photoelectric effect to probe the electronic structure of a material. It uses an X-ray beam to eject electrons of different binding energies from the material. These ejected electrons have a range of kinetic energy and pass through a double hemispherical analyzer that slows down the electrons to a specific energy known as the pass energy. Electrons with an energy higher than the pass energy hit the outer hemisphere and ones with a lower energy hit the inner hemisphere. Only electrons with the right energy in the scanning window are allowed to pass through to the electron multiplier. Subsequently, scanning different energy windows allows for the acquisition of a complete spectrum. Since the incident energy of the X-ray beam and work function of the detector are known parameters, the kinetic energy of the ejected electron corresponds

to a specific element (calculated using equation 2.1) and bonding environment.

$$E_B = \mathrm{h}\nu - E_k - \phi_S \tag{2.1}$$

where, E_B is the binding energy of the photoelectron, hν is the incident photon energy, E_k is the kinetic energy of the ejected photoelectron, and ϕ_S is the workfunction of the spectrometer.

XPS is effective in obtaining chemical composition, local bonding, valence and other electronic and structural signatures of the sampled material. Extensive angle resolved XPS characterization was done as a part of this thesis to determine surface composition in flat single crystalline samples. This information can inform density functional theory (DFT) calculations and direct methods for surface refinement.

An X-ray beam is generated by rastering high energy electrons on a metal typically Al or Mg for XPS and Cu for structural analysis. The results presented here were acquired with Al K-alpha emission (1486.6 eV). Some additional XPS experiments were performed at Advanced Photo Source at Argonne National Lab with different incident energies due to the tunable nature of synchrotron radiation.

A majority of the XPS experiments were performed using the Thermo Scientific ESCALAB 250 Xi at Northwestern University. It is equipped with an Al K-alpha with spot size in the range of $200 - 900$ μm. Angle resolved XPS was performed to obtain surface sensitive information. All XPS spectra reported here have been corrected for charging

with reference to the adventitious 1s carbon peak. In addition, the reported peak areas are from the fitting of mixed Gaussian-Lorentzian functions (30% mixing). The fitting was performed with a convergence of 1×10^{-6} using a maximum of 20,000 iterations under the Powell and smart algorithm implemented in the *Thermo Avantage Software Package*.

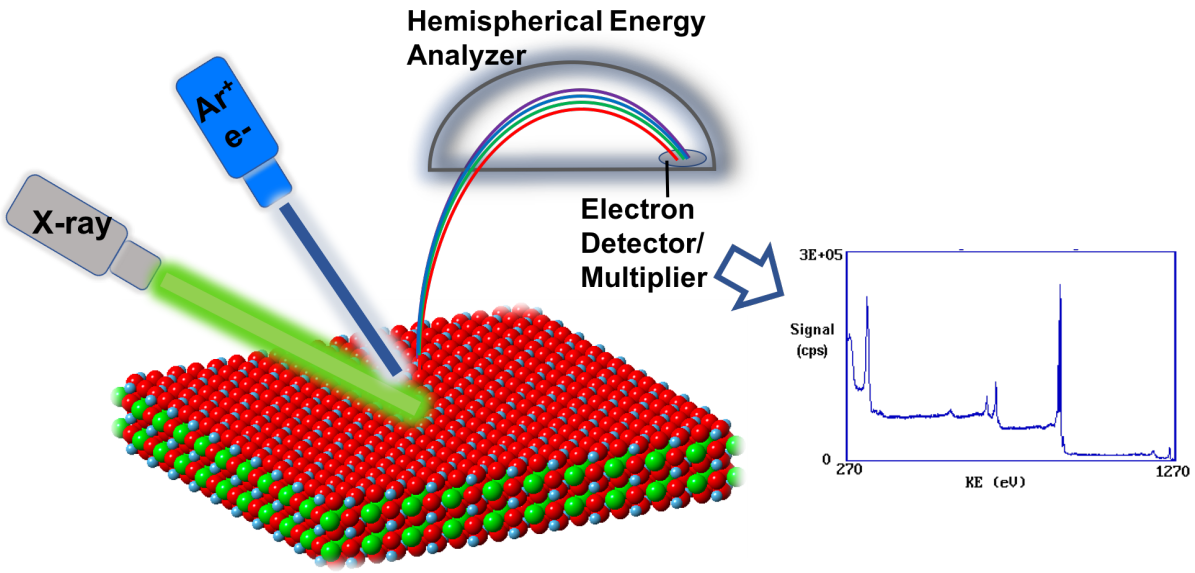

Figure 2.5. Schematic of X-ray photoelectron system depicting simultaneous exposure to X-ray beam and a charge compensation source used for insulating samples.

XPS can be used to quantify surface composition and termination of a flat single crystalline sample. The measurements rely on changes in the sample depth as a function of take off angle which was controlled by tilting the sample stage with respect to the analyzer. The sampling depth can be expressed by the well known Beer-Lambert law given in equation 2.2

$$I = I_0 \exp\left(\frac{-z}{\lambda \cos(\theta)}\right) \tag{2.2}$$

where z is the sampling depth, λ is the inelastic mean free path of the photoelectron and θ is the take-off angle of photoelectrons measured from the surface normal. Higher take-off angles increase attenuation and therefore sample relatively small depths. 95% of the total signal collected comes from 3λ. The analysis of flat samples is relatively simple as the attenuation is homogeneous in the sample.

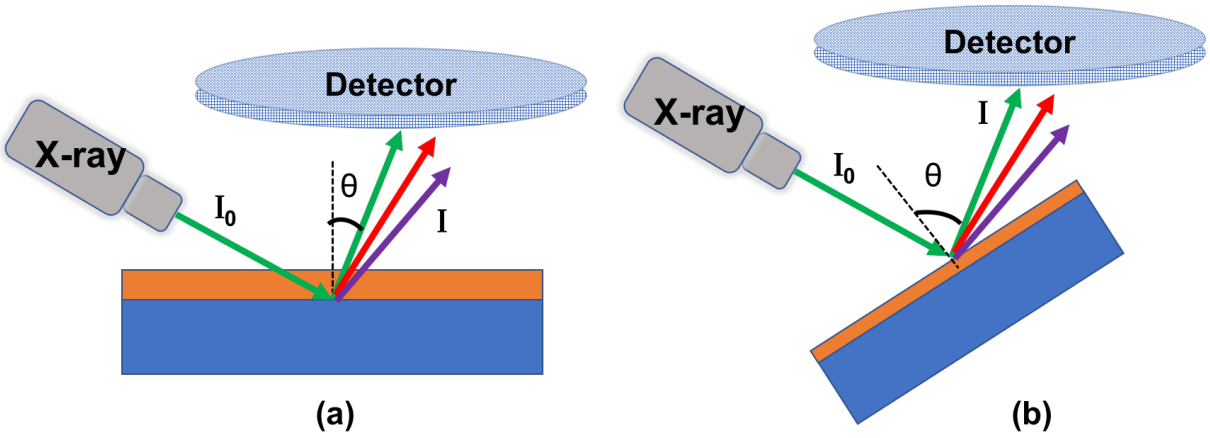

Figure 2.6. Schematic of angle resolved XPS with normal take off in (a) and grazing take off in (b). Grazing take off angle leads to a more surface sensitive spectra.

Attenuation analysis can also be extended to a complex perovskite material with different stackings along different crystallographic directions. For instance, for the case of $SrTiO_3$ along the [001] direction the stacking of layers is TiO_2 and SrO. To model such

stacking, layer by layer attenuation must be accounted for [25] using the spacing between planes and adding the relative intensity over the sampling depth ($\sim 5\lambda$).

2.1.4. Ultraviolet Photoelectron Spectroscopy (UPS)

ultraviolet photoelectron spectroscopy (UPS) spectra were taken using a high photon flux ($> 1.5 \times 10^{12}$ photons/second) UV source with a spot size of approximately 1.5 mm. The source energy was 21.22 eV for He-I and 40.8 eV for He-II. The relatively intensity of He-I and He-II was controlled by varying the base Ar pressure in the line. He-I emission dominated when the Ar pressure was higher than 8×10^{-7} Torr. The same hemispherical analyzer as the one described in the XPS section was used for UPS experiments.

UPS has a much smaller penetration depth ($\sim$2.5 nm) in comparison to XPS ($\sim$10 nm). In addition to the smaller penetration depth, it also provides a higher sensitivity in the valence region due to relatively high scattering cross section of states. However, UPS spectra usually suffer from a high secondary electron background.

2.1.5. Reflection Electron Energy Loss Spectroscopy (REELS)

Reflection electron energy loss spectroscopy (REELS) measurements were taken using an incident energy of 1 keV. The emission current was stabilized at 5 μA and a 150 μm aperture was used. A pass energy of 10 eV was used with steps size of 0.1 eV and 50 ms dwell time. The same hemispherical analyzer as the one described in the XPS section was used for measurements. This technique is well suited for use with insulators as it relies on reflected electrons which exhibit less charging artifacts than transmitted electrons.

2.1.6. Atomic Force Microscopy (AFM)

Atomic force microscopy (AFM) is a highly surface sensitive technique that relies on the interaction force between a sharp tip (usually of the order of few atomic radii) and the sample. The changes in interaction force correspond to a change in the separation between the tip and the sample surface. Hence, AFM can be used to obtain high resolution surface topography information. It can be used in different modes: contact mode, non-contact mode and tapping mode. The position of the tip is determined by tracking the tip cantilever with a laser. In tapping mode, the cantilever oscillates at frequencies slightly below or at resonance. The resonant frequency is dependent on the separation between the AFM tip and the substrate. AFM is very applicable to imaging large surfaces in conjunction with electron microscopy as TEM provides a 2D projection of the surface along with the bulk. The data presented in this work is from tapping mode AFM using the *Bruker Dimension Fastscan*.

2.2. Theory and Simulations

2.2.1. Direct Methods (DM)

Electron diffraction is a powerful technique for studying crystal structure in a wide range of materials. Amplitude and symmetry of a diffraction pattern contains information on the crystal structure however the phase information is lost. If both the phase and amplitude are known then a direct Fourier inversion would determine the structure. Direct methods (DM) [26–41] is a numerical approach to address this problem. It can be used

to establish phase relationship between reflections and therefore be used for a more direct solution of the phase. However, there are limitations on the thickness of the sample due to the requirements for a kinematical diffraction pattern in DM. The software used for this analysis is an in-house open source code, Electron Direct Methods (EDM) [42]. EDM measures intensities from digitized diffraction patterns and searches for the solution in phase space that is consistent with the set of measured intensities. EDM provides a 2D projection of the scattering potential and hence requires further refinement in the direction of the projection. In addition, oxygen positions are not easily obtained from DM as it is a weak scatterer compared to transition metal cations. In such cases, information on the bulk structure, preferred coordination of the cations and valence compensation is used to refine the oxygen position based on χ^2, which is defined as:

$$\chi^2 = \frac{1}{N-M} \sum \left(\frac{I_{meas} - I_{calc}}{\sigma} \right)^2 \tag{2.3}$$

where, I_{meas} is the measured intensity, I_{calc} is the calculated intensity, N is the number of reflections in diffraction pattern, M is the number of variable parameters, and σ is the measurement error. It is also essential to determine how the surface structure registers on the bulk.

2.2.2. Multislice Simulation

Multislice algorithm is commonly used in simulating HREM images. The confidence in an analysis performed on an experimental image is verified by repeating the same

on a simulated image. Hence, it is important to mimic the experimental conditions in simulations. The form of multislice [43–45] algorithm presented here has been adapted from "*High-Energy Electron Diffraction and Microscopy*"[44]. This information has also been added to a Wikipedia page on Multislice. The multislice algorithm is an approach to solving the time independent Schrödinger wave equation:

$$-\frac{\hbar^2}{2m}\frac{\partial^2\Psi(x,t)}{\partial x^2} + V(x,t)\Psi(x,t) = E\Psi(x,t) \tag{2.4}$$

In 1957, Cowley and Moodie [45] showed that the Schrödinger equation can be solved analytically to evaluate the amplitudes of diffracted beams. Subsequently, the effects of dynamical diffraction can be calculated and the resulting simulated image will exhibit good similarities with the actual image taken from a microscope under dynamical conditions. Multislice does not make any assumption about the periodicity of the structure, as a result this method can be used to simulate HREM images of aperiodic systems as well.

The Schrödinger equation can also be represented in the form of incident and scattered wave as:

$$\Psi(\mathbf{r}) = \Psi_0(\mathbf{r}) + \int G(\mathbf{r},\mathbf{r}')V(\mathbf{r}')\Psi(\mathbf{r}')d\mathbf{r}' \tag{2.5}$$

where $G(\mathbf{r}, \mathbf{r}')$ is the Green's function that represents the amplitude of the electron wave function at a point $\mathbf{r}$ due to a source at point $\mathbf{r}'$.

For an incident plane wave of the form $\Psi(\mathbf{r}) = \exp(i\mathbf{k} \cdot \mathbf{r})$ the Schrödinger equation can be written as:

$$\Psi(\mathbf{r}) = \exp(i\mathbf{k} \cdot \mathbf{r}) - \frac{m}{2\pi\hbar^2} \int \frac{\exp(i\mathbf{k} \cdot |\mathbf{r} - \mathbf{r}'|)}{|\mathbf{r} - \mathbf{r}'|} V(\mathbf{r}')\Psi(\mathbf{r}')d\mathbf{r}' \tag{2.6}$$

We then choose the coordinate axis in such a way that the incident beam hits the sample at (0,0,0) in the $\hat{z}$-direction. Now we consider wave-function with a modulation function $\phi(\mathbf{r})$ for the amplitude of the wave-function. The modulation function can be represented as:

$$\phi(\mathbf{r}) = 1 - \frac{m}{2\pi\hbar^2} \int \frac{\exp[i\mathbf{k}|\mathbf{r} - \mathbf{r}'| - i\mathbf{k} \cdot (\mathbf{r} - \mathbf{r}')]}{|\mathbf{r} - \mathbf{r}'|} V(\mathbf{r}')\phi(\mathbf{r}')d\mathbf{r}' \tag{2.7}$$

Now we make substitutions with regards to the coordinate system we have chosen.

$$\mathbf{k} \cdot (\mathbf{r} - \mathbf{r}') = k(z - z') \quad \& \quad |\mathbf{r} - \mathbf{r}'| \approx (z - z') + (\mathbf{X} - \mathbf{X}')^2/2(z - z') \tag{2.8}$$

$$\phi(\mathbf{r}) = 1 - i\frac{\pi}{E\lambda} \int_{z'=-\infty}^{z'=z} V(\mathbf{X}', z')\phi(\mathbf{X}', z') \frac{1}{i\lambda(z - z')} \exp\left(ik\frac{|\mathbf{X} - \mathbf{X}'|^2}{2(z - z')}\right) d\mathbf{X}'dz' \tag{2.9}$$

where $\lambda = 2\pi/k$ is the wavelength of the electrons with energy $E = \hbar^2 k^2/2m$, $\mathbf{X}$ is the coordinate in XY plane when the beam is oriented in the z-direction.

So far we have set up the mathematical formulation of wave mechanics without addressing the scattering in the material. The interaction constant is defined as

$$\sigma = \pi/E\lambda \tag{2.10}$$

We also need to address the transverse spread which is done in terms of the Fresnel propagation function

$$p(\mathbf{X}, z) = \frac{1}{iz\lambda} \exp\left(ik\frac{\mathbf{X}^2}{2z}\right) \tag{2.11}$$

In multislice simulation the thickness of each slice over which the integration is performed is usually small and as a result within a slice the potential field can be approximated to be constant $V(\mathbf{X}', z)$. Subsequently, the modulation function can be represented as: [46]

$$\phi(\mathbf{X}, z_{n+1}) = \int p(\mathbf{X} - \mathbf{X}', z_{n+1} - z_n)\phi(\mathbf{X}, z_n) \exp\left(-i\sigma \int_{z_n}^{z_{n+1}} V(\mathbf{X}', z')dz'\right) dX' \tag{2.12}$$

We can therefore represent the modulation function in the next slice

$$\phi_{n+1} = \phi(\mathbf{X}, z_{n+1}) = [q_n \phi_n] * p_n \tag{2.13}$$

where, * represents convolution, $p_n = p(\mathbf{X}, z_{n+1} - z_n)$ and $q_n(\mathbf{X})$ defines the transmission function of the slice.

$$q_n(\mathbf{X}) = \exp\{-i\sigma \int_{z_n}^{z_{n+1}} V(\mathbf{X}, z')dz'\} \tag{2.14}$$

The iterative application of the aforementioned procedure will provide a full representation of the sample in context. It should be reiterated that no assumptions have been made on the periodicity of the sample apart from assuming that the potential $V(\mathbf{X}, z)$ is uniform within the slice. As a result, it is evident that this method in principle will work for any system. For aperiodic systems in which the potential will vary rapidly along the beam direction, the slice thickness has to be significantly smaller than for a periodic system resulting in higher computational cost.

2.2.3. Density Functional Theory (DFT)

Structure, stability and electronic properties can be all described quantum mechanically by the Schrodinger's equation. Evaluating materials properties requires solving the N-particle Schrodinger's equation; the number of variables scales as N^3 for an N electron system. Time dependent Schröndinger's equation is of the form:

$$i\hbar\frac{\partial}{\partial t}\Psi(\vec{r}, t) = \left[\frac{-\hbar^2}{2\mu}\nabla^2 + V(r, t)\right]\Psi(r, t) \tag{2.15}$$

where, μ is the particle's reduced mass (in the quantum mechanical regime it would be the effective mass), $\Psi(r,t)$ is the time dependent wave function, $V(r,t)$ is the time dependent potential energy, the ∇^2 operator with a prefactor is the kinetic energy term.

For a system with large number of electrons, analytically solving the Schrödinger's equation is a daunting task. Hence, approximations are made and numerical recipes are used. DFT provides a means to solve the many body problem by simplifying it into many single body Schrödinger-like equation. This involves knowing the exact form of the potential energy term which can only be approximated; accurate simultaneous description of both exchange and correlation is challenging.

Hohenberg and Kohn established the foundations for modern day DFT. They proposed that there is a one-to-one mapping of the electron density to any observable property, given that the system is in its ground state. This theorem simplifies the many body Schrodinger's equation into many single body equations which are relatively easier to solve using computational approaches (see equation 2.16).

$$\left(-\frac{\hbar^2}{2\mu}\vec{\nabla}_m^2 + \frac{e^2}{4\pi\epsilon_0}\int\frac{\rho(\vec{r'})}{|\vec{r}-\vec{r'}|} + V_{xc} + V_{ext}\right)\Psi_m(\vec{r}) = \epsilon_m\Psi_m(\vec{r}) \tag{2.16}$$

The next challenge lies in properly defining the exchange-correlation functional (V_{xc}). The two widely used electron density functionals in DFT are local density approximation (LDA) and generalized gradient approximation (GGA) [47, 48]. The former assumes

a slowly varying electron density whereas the latter takes into account the gradient of electron density allowing for inhomogeneous variations and localization in the electronic structure. The spin resolved energy density functional for $E_{xc}[\rho]$ [48] under the two approximation is given as:

$$E_{xc}^{LSD}[n\uparrow, n\downarrow] = \int n(r)\epsilon_{xc}(n\uparrow(r), n\downarrow(r))d^3r \tag{2.17}$$

$$E_{xc}^{GGA}[n\uparrow, n\downarrow] = \int f(n\uparrow, n\downarrow, \nabla n\uparrow, \nabla n\downarrow)d^3r \tag{2.18}$$

The DFT calculations carried out as a part of this thesis were performed using WIEN2k package [49] which is a full potential linearlized augmented plane wave (LAPW)-code. This method uses augmented plane waves along with local orbitals (APW+lo). Local orbitals define the region inside the muffin tin, whereas plane waves are used to treat the outer region. Inside the muffin tin, the basis set is a combination of spherical harmonics, radial functions and local orbitals. There are certain constraints on the basis set from the fact that the wave function at the boundary of muffin tin has to be continuous. The product of the smallest muffin tin radius (R_{MT}) and largest k-vector (K^{max}) sets the accuracy of the code. A realistic compromise between the accuracy for a calculated property and computational expense is chosen.

CHAPTER 3

c(6×2) Surface Reconstruction on $SrTiO_3$ (001)

3.1. Introduction

Strontium titanate ($SrTiO_3$) is a prototypical perovskite material with a cubic symmetry. The unit cell of $SrTiO_3$ has O^{2-} at the face centers, Ti^{4+} at the center of the cube and Sr^{2+} at the corners as shown in Figure 3.1. Even though $SrTiO_3$ is cubic over a wide range of temperature and pressure, stress driven structural distortions [50–52] and doping [53, 54] can lead to the breaking of cubic symmetry and given rise to phenomena such as ferroelectricity. For instance, Ca doped $SrTiO_3$ shows a peak in permittivity and a crossover from a XY quantum ferroelectric state to a "diffusive character" can be induced by increasing the number of dopants [53, 55]. Heteroepitaxial growth can also lead to unique quantum confinement effects [56]. Even though early investigations of electronic properties also revealed polarization hysteresis loops below 50 K [50], for applications in ferroelectric devices, it is important to have good performance in the vicinity of room temperature. Recent works have demonstrated room temperature ferroelectricity in the presence of strain [57].

Besides the interesting bulk properties of $SrTiO_3$, a significant amount of work reported in literature has focused on studying the electronic properties of hetero-structured

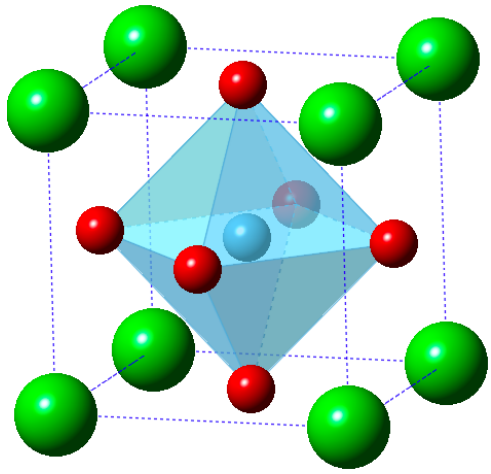

Figure 3.1. Unit cell of $SrTiO_3$. Green atoms are 12 coordinated site (Sr), blue atom is the octahedral site (Ti) and red are oxygen.

interfaces with other oxide materials. $LaAlO_3/SrTiO_3$ interface is one of the most widely studied oxide hetero-interfaces. This interface exhibits a high mobility electron gas [21, 58], deviating from the known bulk insulating behavior. Other studies have demonstrated oxygen vacancy driven interfacial superconductivity [59]. Many of the interesting properties arise due to structural and electronic differences at the surface in comparison to the bulk. As a result, atomic level understanding of the surface structure and electronic properties is essential for any application.

Numerous reconstructions have been observed on different surfaces of $SrTiO_3$. Even for something as simple as $SrTiO_3$, solving the atomic position on the surface is challenging and in most cases, involves the use of multiple characterization techniques aided by simulations and theoretical models. A summary of surface reconstructions that have been reported on $SrTiO_3$ is given in Table 3.1.

Table 3.1. Reconstructions on $SrTiO_3$ surfaces

Surface	Reconstruction	Reference
(001)	(2×1)	[10, 60–64]
	(2×2)	[65–71]
	$(\sqrt{5} \times \sqrt{5})$R26.6°	[63, 67, 72–74]
	c(4×2)	[11, 60, 64, 66, 67, 75–77]
	c(6×2)	[12, 62]
	$(\sqrt{13} \times \sqrt{13})$R33.7°	[7, 63, 67]
	c(4×4)	[60, 67, 71]
	(6×2)	[8, 76, 78]
	(9×2)	[78]
	(12×2)	[78]
	(7×4)	[78]
(110)	(2×1)	[79]
	$(n \times 1)$	[80, 81]
	(4×1)	[81]
	(2×8)	[81]
	(1×10)	[81]
(111)	$(n \times n)$	[82–84]
	$(\sqrt{13} \times \sqrt{13})$R13.9°	[85]
	$(\sqrt{7} \times \sqrt{7})$R13.9°	[85]

However, not all of them have been solved for detailed atomic positions. The works reported in literature use a variety of techniques such as scanning tunneling microscopy (STM), low energy electron diffraction (LEED), TED or a combination of these techniques assisted with DFT calculations. There are some theoretical models such as the Sr adatom model [86] which attempt to explain the thermodynamics behind surface reconstruction, although there is no evidence supporting the model. As a result, there is a need for better theories, models and surface sensitive characterization techniques.

A comprehensive analysis of the c(6×2) surface reconstruction on the $SrTiO_3$ (001) surface was performed and the results are discussed in the following sections.

3.2. c(6×2) Surface Reconstruction on $SrTiO_3$ (001)

The c(6 × 2) reconstruction on the (001) surface has been reported in literature [12, 62, 76]. A combination of techniques, including HRSEM and plan view HREM analysis was used in conjunction with DFT calculations to solve the structure.

3.2.1. Previous Studies

Early observations of the c(6×2) surface reconstruction were made using a combination of Auger electron spectroscopy (AES), LEED and STM, by Zegenhagen et al. [76]. The samples were made in two different ultra high vacuum (UHV) annealing conditions, both involving a pre-anneal at 1100°C for 3 hours in flow oxygen in a clean quartz tube:

(1) $H_2 : 5 \times 10^{-7}$ mbar at 950° for 2 hours

(2) $O_2 : 5 \times 10^{-8}$ mbar at 950° for 2 hours

It was also demonstrated that the final surface structure depends strongly on the surface condition of the $SrTiO_3$ crystal prior to UHV annealing. High resolution STM images were reported in the work by Zegenhagen (see Fig. 3.2). The preliminary evidence for the occurrence of c(6×2) was obtained from LEED as shown in Fig. 3.3.

Following the early works by Zegenhaen et al., a work detailing the atomic structure was proposed in literature by Lanier et al. [12]. This work employed a combination of TED, surface X-ray diffraction (XRD), DM analysis, computational combinatorial screening and DFT based calculations. Even though the work presented was convincing, it

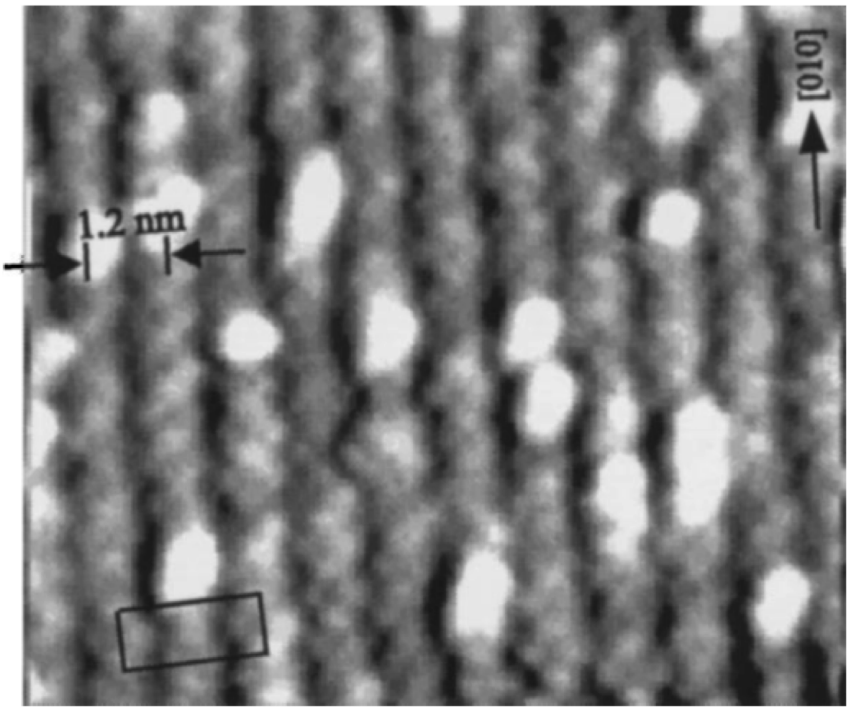

Figure 3.2. High resolution STM image of the c(6×2) reconstruction. The spacing of rows is 11.7 Å. A unit cell of the c(6 × 2) is outlined in the lower left corner of the image. (Adapted from [76])

missed subtleties of surface-bulk registry and most importantly Sr atom positions on the surface layer.

The c(6 × 2) surface structure was solved via an extensive collaboration: the sample was prepared by Dr. Yuyuan Lin; HREM and HRSEM imaging were done by Dr. Jim Ciston at Lawrence Berkeley National Laboratory, Brookhaven National Laboratory and the Hitachi laboratory in Japan; plan view analysis of HREM images was done by me; simulations of HRSEM images were done by Prof. Laurence Marks and collaborators at the University of Melbourne; DFT calculations and structure relaxations were done by Prof. Laurence Marks.

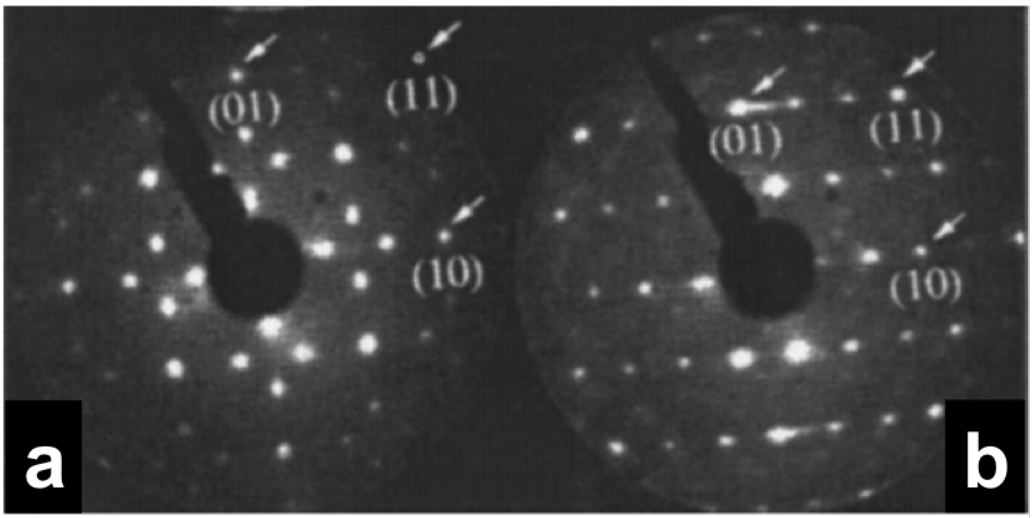

Figure 3.3. (a) Double domain c(6×2) reconstruction obtained by annealing a well-oriented and O_2 pre-treated $SrTiO_3$ (001) surface in UHV. (b) A single domain c(6×2) reconstruction stabilized on a vicinal [1.2° off (001) $SrTiO_3$ surface]. (Adapted from Ref. [76])

As a result, the work presented here is seminal with respect to the techniques it employs as well as the complexity of surface structure on the $SrTiO_3$ (001) surface. The details of the c(6×2) surface reconstruction using plan view HREM and HRSEM are discussed further in the following sections.

3.2.2. Plan View Image Analysis

Plan view image analysis was performed on HREM data obtained from a sample with c(6×2) surface reconstruction using the TEAM0.5 microscope at the National Center for Electron Microscopy (NCEM). The images were acquired by Dr. Jim Ciston from a sample prepared by a former group member, Dr. Yuyuan Lin. The sample was prepared following the normal procedure (see Chapter 2) along with BHF etching and annealing in dry O_2 at

approximately 1050°C. Plan view image analysis is a very powerful technique for studying surface structures, although it may sound counterintuitive at first. The capabilities of probing the surface comes from the fact that the surface structure is different from the bulk and hence has a different periodicity. A total of 41 images were taken with varying defocus values. The microscope parameters are given in Table 3.2. The defocus values for

Table 3.2. Microscope Parameters

Parameters	Voltage (kV)	C3 (μm)	Focal Spread (nm)	Convergence (mrad)
Values	80	16	1.4	0.2

the 41 images ranged from 30 nm to -12 nm with a step size of -1.05 nm. Careful analysis of each of these images was performed. Before detailed analysis, it was important to verify the experimental focus condition as the defocus values obtained from experiments may not be exact. Subsequently, HREM multislice simulations were performed for the entire focal series using MacTempas Code. A focal spread of 1.4 nm was used. Fresnel fringes at the two end of the focal spectrum, 30 nm and -12 nm, were analyzed to determine the accuracy of defocus values. The fringes on the experimental and simulated images in Figure 3.4 and 3.5 are qualitatively consistent. Further refinement showed that a defocus shift of 1 nm from experimentally determined values yielded the best match.

The first step on the interpretation of plan view images involves bulk removal. Bulk removal is implemented in EDM in reciprocal space. Hanning masked fast fourier transform (FFT) of the high resolution image is taken as illustrated in Figure 3.6.

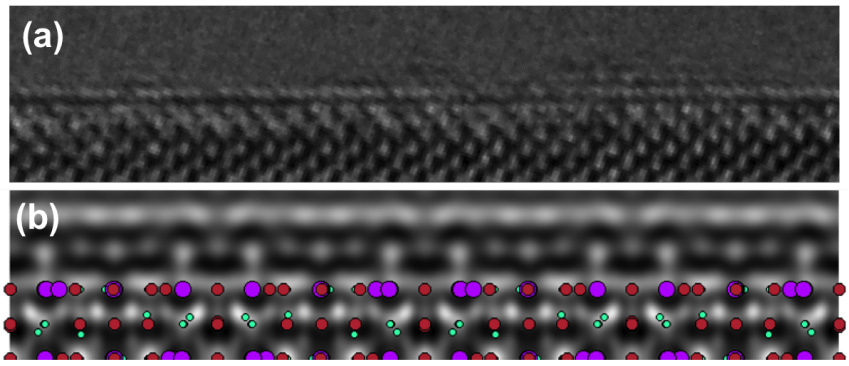

Figure 3.4. Fresnel fringe at the edge of (a) experimental image (b) simulated image at 30nm defocus with structure overlaid.

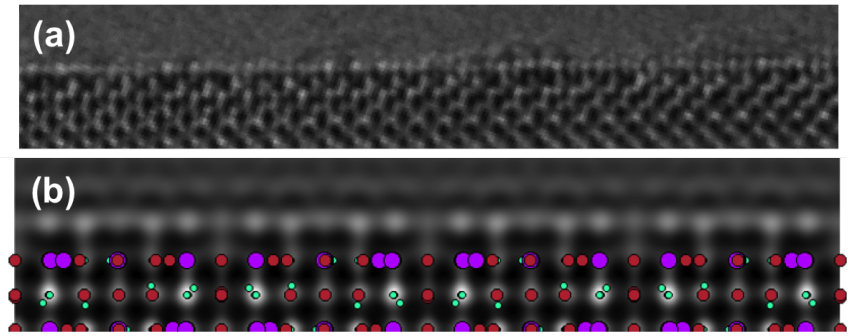

Figure 3.5. Fresnel fringe at the edge of (a) experimental image (b) simulated image at -12 nm defocus with structure overlaid.

The spots corresponding to bulk in the FFT are masked leaving behind only the surface spots. Although the bulk spots also contain some signal from the surface, for the convenience of analysis they are set to zero resulting in an incomplete data set. The data after bulk removal can be considered a superposition of intensities from the top and bottom surfaces. The separation of the top and bottom surface was done using the method outlined in Chapter 4. Bulk removal was followed by correction for the translation between the top and bottom surface. In addition, mechanical vibration of 0.4 Åwas added in both x and y directions to mimic the conditions in the microscope. Corrections to account for

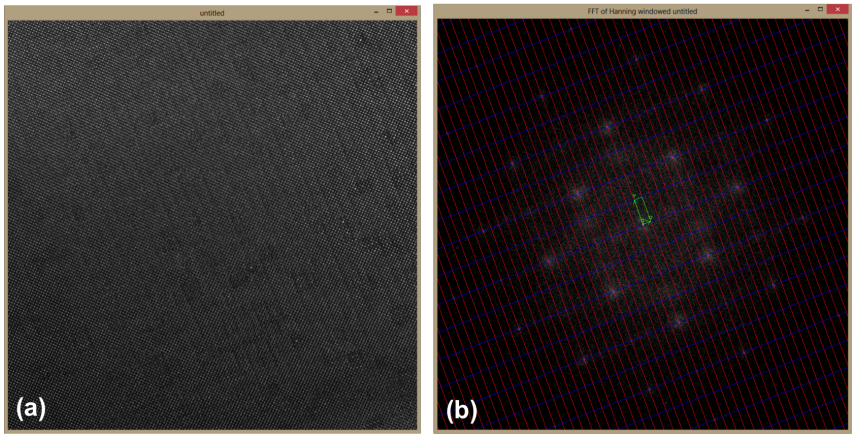

Figure 3.6. (a) A plan view HREM micrograph of a sample containing c(6×2) surface reconstruction (b) Hanning masked FFT of (a) showing one of the domains of c(6 × 2) unit cell in green.

the acquisition conditions in the Gatan 894 US1000 CCD detector were done using the modulation transfer function (MTF) (see Figure 3.7) of the Nyquist frequency. The MTF was used to damp the image. The resulting image along with the overlay of the structure

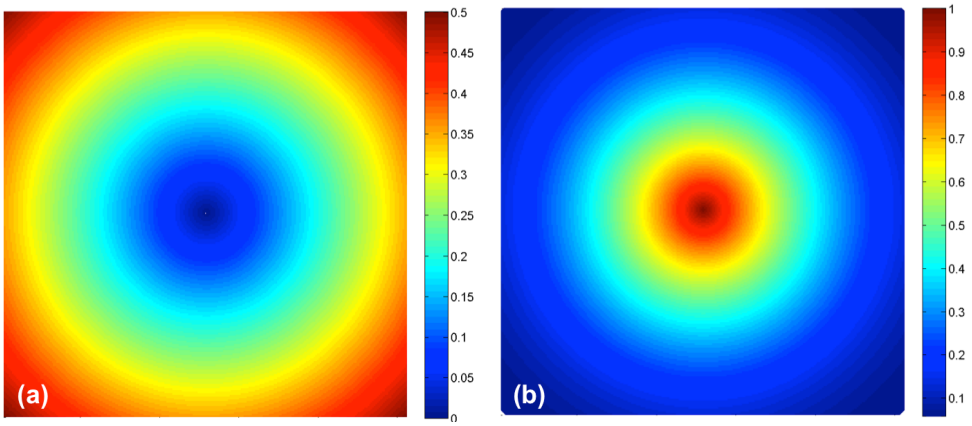

Figure 3.7. (a) Frequency distribution with blue (0) indicating low and red high (0.5) frequencies respectively (b) Modulation transfer function of (a) (Red indicated complete transmission and blue indicates complete damping.)

is given in Figure 3.8. The match between the simulated and experimental image is good

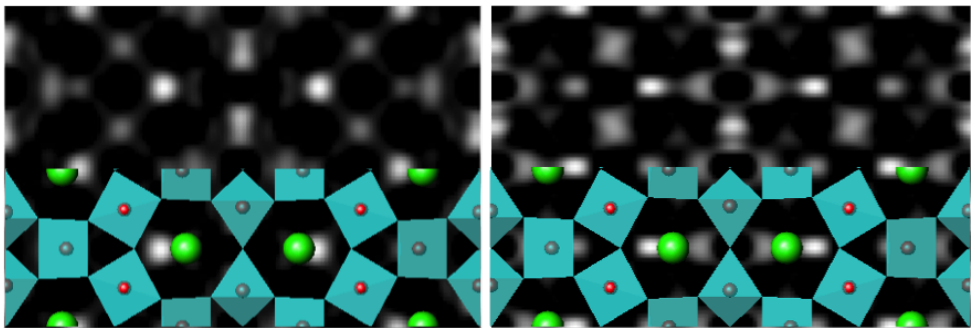

Figure 3.8. Experimental (left) and simulated (right) HREM images of the $SrTiO_3$ (001) c(6 × 2) surface reconstruction at a defocus of 0.55 nm with bulk subtraction and correction for top/bottom surface registry shift.

considering the low signal to noise in the HREM image. The positions of the Sr atoms on the surface are unambiguous and strong. The effective thickness of simulation is 5.3 nm.

The next section presents surface structure imaging with HRSEM. The experiments were performed at Brookhaven National Lab by Dr. Jim Ciston. The analysis was done by Prof. Laurence Marks in collaboration with Prof. Les Allen's group at the University of Melbourne. Structure relaxation and orbital band energies were calculated using DFT by Prof. Laurence Marks.

3.2.3. High Resolution Secondary Electron Microscopy

As discussed in Chapter 2, there are a multitude of signals that arise from electron specimen interactions including electrons and X-ray radiation. With advancement in electron sources, electromagnetic lenses and aberration correctors, it has become possible to routinely obtain resolutions in the sub-angstrom regime. This has been widely used in

scanning transmission electron microscopy (STEM) and TEM. The application to scanning electron microscopy (SEM) has only been recently realized.

Aberration corrected electron microscopy has opened new avenues for materials research by reducing the probe size to sub-angstroms. Aberration correctors used with secondary electron imaging can provide atomic resolution imaging with surface sensitivity [87].

In addition to advancements in aberration correctors and highly coherent electron sources, theoretical understanding of secondary electron generation and subsequent contrast mechanisms have been elucidated for quantitative comparison of experimental data and theoretical simulations. The first work [88] on this topic suggested that secondary electrons are generated by inelastic scattering given by an object function (equation 3.1) of the form,

$$L(r) = \frac{1}{1 + {r^2}/{r_0^2}} \exp\left(\frac{-2r}{{\hbar^2 k}/{mE}}\right) \tag{3.1}$$

where, k is the incident-electron wave number, m is the electron rest mass and E is the energy loss, r is the distance from the center of an atom, r_0 accounts for the cross section of the atom. Based on this principle intensities were calculated for Sr, Ti and O atoms in $SrTiO_3$. The calculated intensities indicated a $Z^{0.53}$ dependence, where Z is the atomic number.

The short comings of this method lie in the assumptions of how secondary electrons are ejected. The object function treats scattering in a crude way by just taking the distance from the center of the atom to be the key parameter; additional physics needs to be incorporated into the model to account for local inhomogeneity in the electronic structure Brown et al. developed a model that took into account ionization events as well as the angle-dependence of electron ejection [89]. This method was used for $YBa_2Cu_3O_{7-x}$ simulations and gave better qualitative match to experimental intensities.

For a quantitative comparison of experimental and simulated intensities additional physics that takes into account dielectric screening had to be incorporated. The details are discussed in the following section.

3.2.3.1. Incorporation of dielectric screening in HRSEM simulations. Low energy secondary electrons undergo multiple elastic scattering events before exiting the surface. These scattering events are critical to techniques such as LEED and angle resolved X-ray photoelectron spectroscopy (ARPES). Angular variations in the band structure additionally modulate the attenuation of secondary electrons. For our measurements of secondary electrons images, the angular and energy integration done by the in-lens detector greatly masks these effects. As a result, HRSEM is a incoherent imaging technique. Even though the energies associated with secondary electrons are sub 50 eV, the process is heavily skewed in the forward direction. Hence, the attenuation of electrons in this context is done as a function of inelastic mean free path to the surface (given by equation 3.2 [90]), with regards to take off angle and respective cross sections.

$$\lambda = \frac{2170}{E^2} + 0.72\sqrt{aE} \times n \tag{3.2}$$

where, E is the kinetic energy of the secondary electron, a is the monolayer thickness and n is the number of monolayers. In addition core, semicore and valence electrons were also incorporated into the model. Screening associated with nearby atoms and virtual plasmons are critical. The was accounted for by treating the surface dielectric screening like a surface charge. The solution to Poisson's equation for aloof scattering in the non-relativistic regime were used from the work by Hogan et al. [91]. The electrostatic potential $\phi(r)$ at some point r =(ρ,z) due to a point charge at (0,0,z_0) inside a continuum crystal is given by equation 3.3.

$$\phi(r) = \begin{cases} \frac{2e}{(\epsilon+1)|r-r_0|}, & z \leq 0 \\ \frac{e}{\epsilon}\left(\frac{1}{|r-r_0|} + \frac{\epsilon-1}{(\epsilon+1)\sqrt{\rho^2+(z+z_0)^2}}\right), & z > 0 \end{cases} \tag{3.3}$$

where, ϵ is the dielectric constant of the material. The potential deep inside the crystal (z>>0) reduces to a simple expression used for conventional screening [91]:

$$\textbf{for } z >> 0,\ \frac{\epsilon - 1}{(\epsilon+1)\sqrt{\rho^2 + (z+z_0)^2}} \approx 0, \rightarrow \phi(r) = \frac{e}{\epsilon|r - r_0|} \tag{3.4}$$

Similarly, the potential at the surface corresponds to $r_0 = 0$ given as:

$$\phi(r) = \frac{2e}{(\epsilon + 1)|r|} \tag{3.5}$$

For inelastic scattering processes one would use the imaginary part of the potential which is dissipative; here we use the real part. In addition, we use the frequency-dependent dielectric constant $\epsilon\left({}^{\Delta E}/_{\hbar,q}\right)$ where, ΔE is the energy loss and q is the wave number. As a consequence, the screening of the primary inelastic scattering event will be given as:

$$\textbf{Bulk Screening}(S_B) \propto \mathrm{Re}\left(\frac{1}{\epsilon\left({}^{\Delta E}/_{\hbar}\right)}\right) \tag{3.6}$$

$$\textbf{Surface Screening}(S_S) \propto \mathrm{Re}\left(\frac{2}{1 + \epsilon\left({}^{\Delta E}/_{\hbar}\right)}\right) \tag{3.7}$$

Subsequently, using the complex dielectric function reported in [92] the two limits of the screening were calculated (see Figure 3.9) and normalized to unity for energies larger than 60 eV.

The energy transfer term was the summation of the orbital band edge energies relative to the valence band edge as calculated from DFT and a secondary-electron escape energy of 10 eV. Consequently, for low escape energies such as the states near the Fermi are

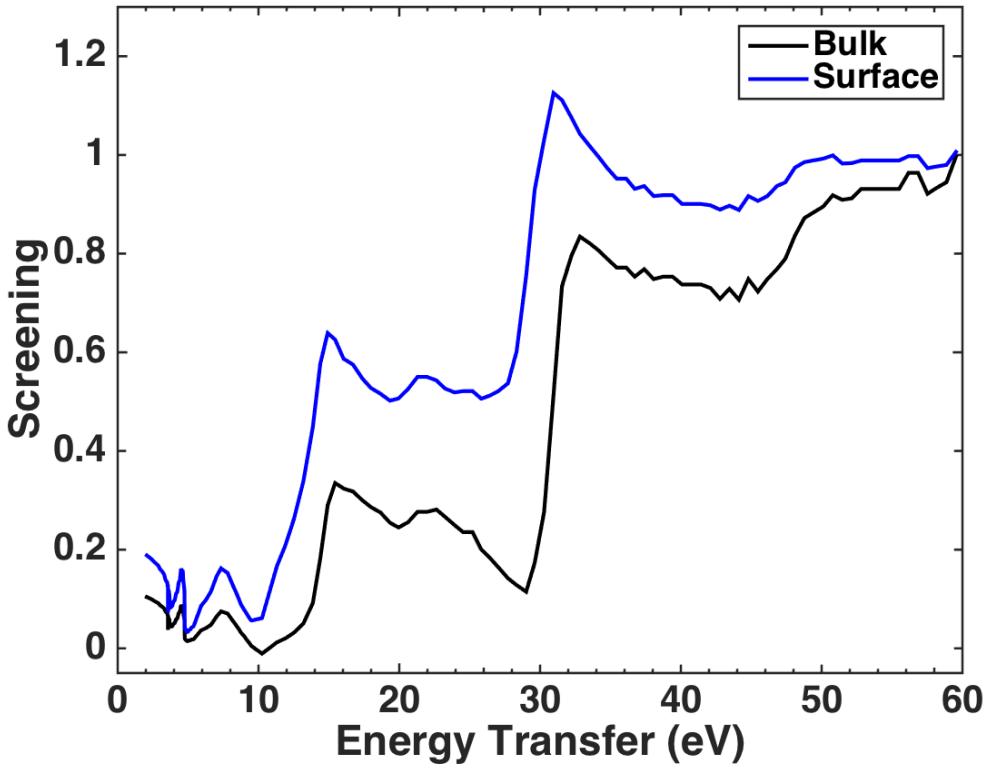

Figure 3.9. Energy dependent dielectric screening coefficients for bulk and surface limits of the dielectric screening in $SrTiO_3$.

strongly damped. On the contrary, the semicore and core states are minimally damped. As a consequence, images simulated without dielectric screening are dominated by oxygen signal (see Figure 3.10).

Taking into account dielectric screening provides a much better match with the experimental data. In addition, the HRSEM simulations take into account dynamical scattering of incident probe. Finite source size and loss of spatial resolution due to steps and terraces was taken into account by convolving a symmetric 2D Gaussian with a full-width half-maximum of 0.14 nm.

A Pearson product-moment correlation was calculated as:

$$c = \frac{\sum_{i=1}^{n}(S_i - < S >)(E_i - < E >)}{\sqrt{\sum_{i=1}^{n}(S_i - < S >)^2}\sqrt{\sum_{i=1}^{n}(E_i - < E >)^2}} \tag{3.8}$$

where, S and E are the simulated and experimental image pixel values, respectively. The Pearson product-moment correlation was calculated with different contributions to the dielectric screening by Dr. Colin Ophus. The model that accounts for screening from all states from core to the valence provides a much better match as indicated by the high correlation value of 0.95 (see Figure 3.11). These results clearly demonstrate the potential applications of HRSEM in direct imaging of complex surfaces in conjunction with high angle annular dark field (HAADF) for identifying the registration of surface with underlying bulk.

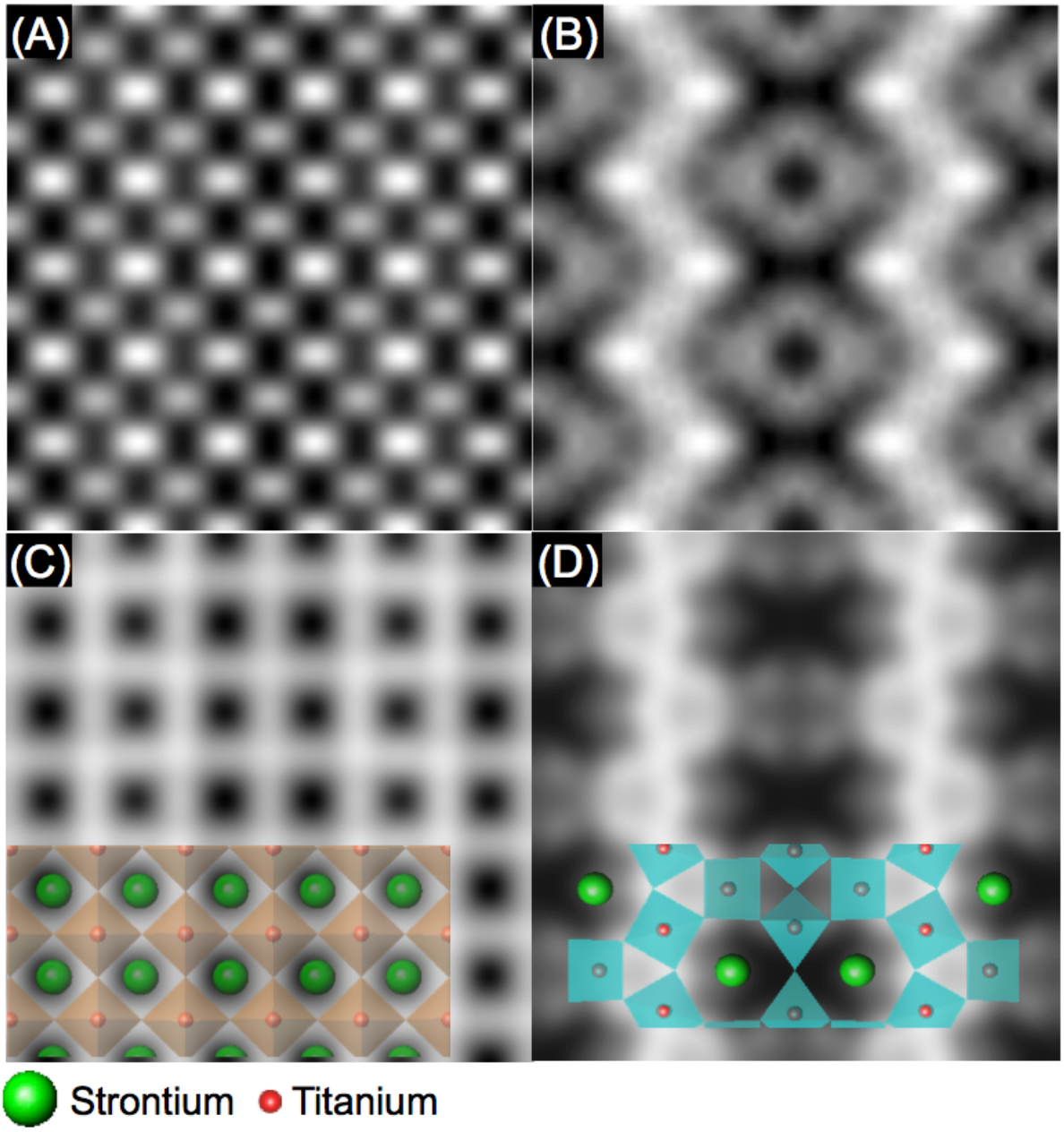

Figure 3.10. HRSEM experiment and simulation without dielectric screening terms: (a) Experimental image with translational 6×2 unit cell averaging with cmm symmetry applied (b) Bulk subtracted experimental image (c) Simulation image including contributions from all orbitals, but without the correction for local dielectric screening (with surface and bulk structure overlayed) (d) Bulk subtracted simulated image. ([8])

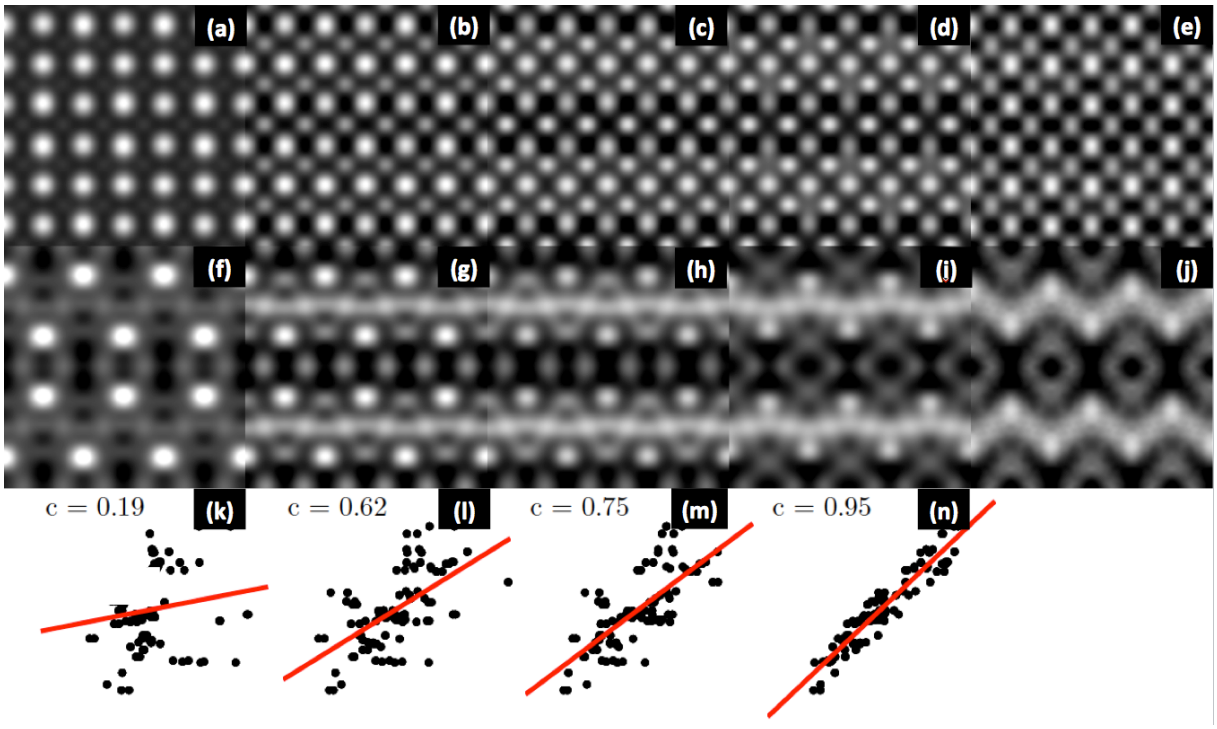

Figure 3.11. Comparison of HRSEM experimental and simulated images. (a-c) HRSEM simulations of the Sr7 structure including damping due to dielectric screening; (a) Using only core states (up to and including the 3d state in Sr, the 2p in Ti and 1s in oxygen). (b) Adding the 4s and 4p for Sr, the 3s and 3p for Ti and 2s for O. (c) Adding the contribution for a filled 2p orbital in O. (d) Shows the HRSEM simulation including all orbitals for the Sr7-effective structure. (e) Shows the experimental result with translational (6×2) unit cell averaging and c2mm symmetry applied. (f−j) In this, we show the corresponding bulk-subtracted results for a through e. (k−n) In this, we show the Pearson product-moment correlation of image intensities corresponding to f through j. ([8])

CHAPTER 4

Plan View Imaging

In Chapter 3, plan view imaging was used to solve the c(6×2) surface reconstruction on $SrTiO_3$ (001). However, the details of the method were not discussed. This chapter is specifically aimed at explaining the functionality and limitations of plan view imaging.

4.1. Introduction

Surfaces are ubiquitous and more complex than the underlying bulk; breaking of symmetry, dangling bonds and defects at the surface provide additional degrees of freedom. Even a simple material like Si can have highly complex surface structures [93]. The complexity in binary and ternary systems is significantly higher. Yet, we lack a universal tool for solving surface structures unambiguously. It is often the case that multiple techniques have to be simultaneously used.

A number of theoretical and experimental methods have been developed for solving complex surface structures. For conducting materials and simple unit cells, LEED [63, 65, 72, 76, 81, 94] and atomic resolution scanning probe methods[9, 60, 61, 67, 68, 70, 71, 73–77, 79, 84, 85, 95, 96] are commonly used. TED [66, 82] in conjunction with direct methods [7, 10–12], X-ray scattering studies [12, 97, 98], reflection high energy electron

diffraction (RHEED) [70, 99, 100] and recently HRSEM [8] have also been effectively used to study surface structures.

Many of these techniques have severe limitations with complex reconstructions and also insulators. This is particularly relevant for oxide materials which have an abundance of surface reconstructions; even the prototypical perovskite material $SrTiO_3$ has highly complex surface structures (see Table 3.1).

4.1.1. Plan and Profile View Imaging in TEM

As explained in Chapter 2, TEM is a powerful tool for imaging of complex surfaces. It is used in two different modes, plan view [93, 101–110] and profile view [108, 109, 111–129] which are defined with respect to the orientation of the sample surface. Imaging of nanoparticle surfaces is more suited to profile view imaging as has been demonstrated for gold and silver particles [111–121, 130, 131] and more recently for oxide nanoparticles[122, 123]. It can give out of plane relaxations but includes little to no information along the beam direction. This mode of imaging provides a one dimensional projection of a surface. Even though focal series analysis of a stack images can provide the complete 2D information, its implementation is not trivial.

On the other hand, plan view imaging provides two-dimensional information in the plane of the surface, although no information normal to the surface. In addition, there are additional complexities that arise due to the fact that the surface signal is superimposed

with a large bulk component. Hence, the interpretation of plan view images requires taking into account the two surfaces and a thickness dependent bulk signal.

4.1.2. Interpretation and Analysis of Plan View Images

Plan view images are projections of top and bottom surfaces along with the bulk. As a result, to obtain interpretable surface information one must deconvolve these contributions. The approach used to date is to assume a kinematical model and linear imaging theory; the image after bulk removal to be a simple addition of the top and bottom surface [93]. The resulting potential and intensity can be written as:

$$\psi(r) = 1 + \sigma[V(r) + V(d-r)] \tag{4.1}$$

$$I(r) = 1 + \int \sigma T(u)\{V(u)V^*(u)\exp(2\pi i d.u)\} \times \exp(-2\pi i u.r)du + \eta(r) \tag{4.2}$$

where $V(r)$ and $V(d-r)$ are the potentials of the top and bottom surface respective, d is the in plane translation vector between the top and bottom surfaces, σ is the relativistic interaction constant, $T(u)$ accounts for the microscope parameters, u is coordinate in reciprocal space and $\eta(r)$ is the noise in the image.

The resulting signal without the bulk component is not a true image of the surface but instead a surface sensitive difference closer to a difference map in a conventional crystallographic sense. One deals with a similar signal in direct methods. Surface reflections

that coincide with the bulk are ignored and only those reflections that are solely from the surface are used to search for a plausible phase relation. This approach has not proved to be an issue in the interpretation of potential maps [7, 10–12, 132].

While this method can work [8, 93], it ignores dynamical diffraction coupling with the bulk (e.g. [103–105, 107, 110]). This chapter discusses the limitations and functionality of plan view imaging with the context of $SrTiO_3$ reconstructions. These findings can be applied to other crystalline materials.

4.2. Methods

4.2.1. Sample Preparation

TEM samples were prepared using the method outlined in Chapter 2. Electron transparent samples were annealed in flowing dry oxygen at $1050-1200^{\circ}C$ for 10h in a quartz tube furnace. Samples were also baked in air at $300-500^{\circ}C$ for $1-4$ h directly before the imaging experiments.

4.2.2. Imaging Experiments

HREM experiments were performed on the TEAM 0.5 instrument (FEI Titan-class) at the National Center for Electron Microscopy (NCEM) by Dr. Jim Ciston. The (001) $SrTiO_3$ sample with c(6×2) surface reconstruction was imaged at an accelerating voltage of 80 kV with an energy spread of 0.1 eV, 0.2 mrad convergence angle, 1.4 nm defocus spread and the aberration corrector tuned to balance C_3 against the uncorrected residual

C_5 (C_3 = -16 μm, C_5 = 6 mm). A focal series of 41 images was acquired at defocus steps of -1.05 nm. The first image in the series was acquired at a defocus of 30 nm. The focal series was used for determining the appropriate defocus to maximally enhance bulk subtraction.

The $SrTiO_3$ (111) sample with the (3×3) surface reconstruction was imaged at an accelerating voltage of 300 kV with an energy spread of 0.1 eV, 0.15 mrad convergence angle, 0.7 nm defocus spread and the aberration corrector tuned to balance C_3 against the uncorrected residual C_5 (C_3=-15 μm, C_5=6mm). A focal series of 41 images was acquired at defocus steps of -1.72 nm. No significant beam damage was observed in either sample.

4.2.3. Simulations and Post Processing

HREM simulations were performed using MacTempasX Code [133] with experimental parameters. Post processing of images was done using the in house open source code Electron Direct Methods (EDM) [134]. Keys issues with the functionality of this method can be discussed with two parameters:

- Sample thickness: discussed with c(6×2) on $SrTiO_3$ (001) and the (3×3) on $SrTiO_3$ (111) as a model case
- Symmetry: discussed with (3×3) on $SrTiO_3$ (111) as a model case

4.3. Results

4.3.1. c(6×2) Surface Reconstruction on $SrTiO_3$ (001)

High resolution plan view images acquired from a region of the sample given in Figure 4.1 were processed using the method outlined earlier. The consistency of experimental parameters and defocus were cross checked with simulations from MacTempas. Removal of bulk was done by taking a fast Fourier transform of an image and removing all linear combination of the bulk reciprocal lattice vectors. An unavoidable consequence of this is that the overlapping surface and bulk spots are removed so this is strictly a difference map as mentioned earlier. This was followed by the separation of the top and bottom surface under kinematic assumptions. More detailed explanation of this method is given in Chapter 4. The resulting image for the surface structure acquired from one of the experimental image of defocus 6 Åis given in Figure 4.2 along with the corresponding DFT relaxed structure.

In the limits of linear imaging theory, the resulting image can be directly compared to the intensity of different atomic sites at the surface. The corresponding structure of the c(6×2) surface reconstruction (see Figure 4.2) is consistent with atomic resolution secondary electron images [8] as well as x-ray and scanning tunneling microscopy [76] data.

The correlation between the actual structure in Figure 4.2b and the relative intensities in the experimental image in Figure 4.2a is strong. Sr atoms appear brighter on the

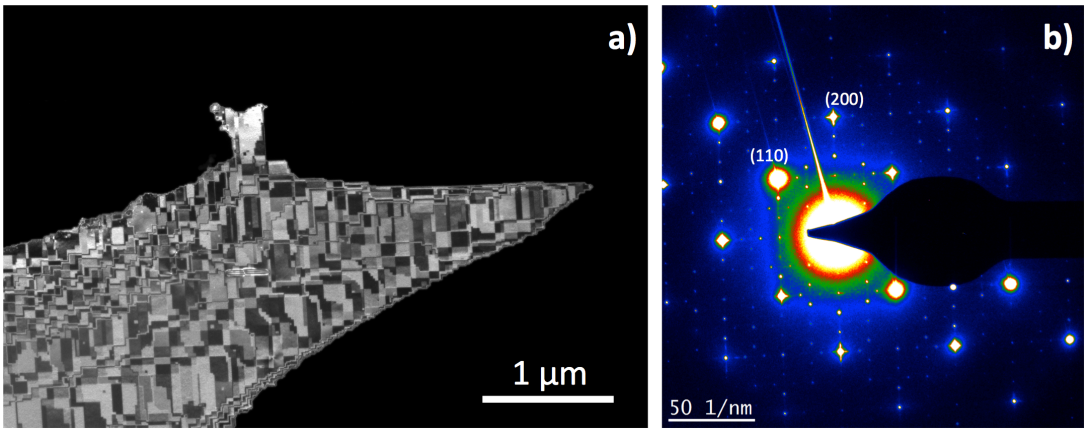

Figure 4.1. (a) Weak beam dark field image of $SrTiO_3$ 001 c(6×2) single crystal with g=(200) used for imaging and 3g=(600) strongly excited, (b). Transmission electron diffraction pattern of the c(6×2) reconstruction acquired approximately 3 degrees off-zone and away from both 2-beam and weak beam conditions to minimize bulk dynamical diffraction. Strong bulk reflections are labeled, while the weaker reflections of higher periodicity are due to the surface reconstruction. (Adapted from Ref. [8])

experimental image which is consistent with Sr being heavier than Ti and O. Separation of the top and bottom surface performed on all 41 images in the focal series show strong intensity at the Sr position with small modulations in the rest of the image. Simulations were performed using MacTempas with the structure in Figure 4.2b for varying bulk thicknesses. The results of the analysis at four different thicknesses and consequently different bulk contributions and dynamical scattering are given in Figure 4.3. The assumptions of linear imaging theory are no longer valid beyond a critical thickness. This critical thickness is material dependent. For instance, this method would work for relatively thicker samples of Si in comparison to $SrTiO_3$.

Surface signal intensity is highly sensitive to the thickness of the sample. Images simulated at 4.15 nm and 5.32 nm thickness show a strong surface signal evident after

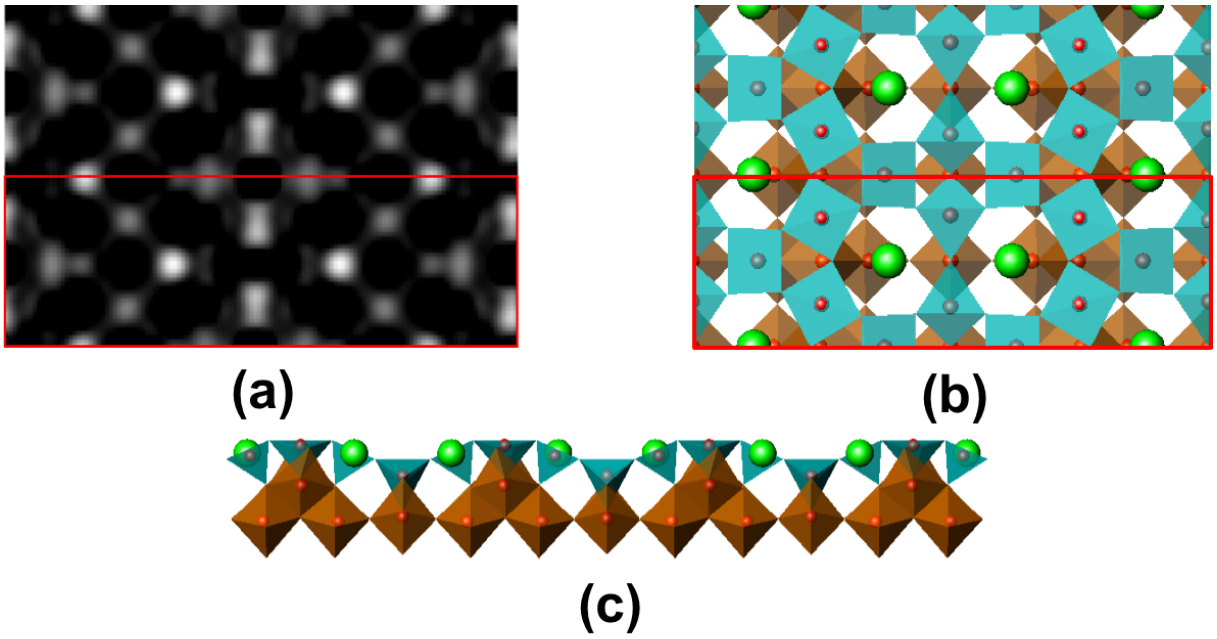

Figure 4.2. In (a) experimental image of the c(6×2) surface reconstruction after the removal of bulk and separation of top and bottom surface from high resolution plan view transmission electron microscopy image and the corresponding structure in (b) plan view and (c) profile view. (The unit cell is outlined in red.)

bulk subtraction. However, the images simulated at 6.49 nm and 7.66 nm thickness show weak surface signal. This is a clear demonstration that the thickness of the sample has to be in the kinematical regime, which for the case of $SrTiO_3$ is approximately 5 nm. The usable, kinematical thickness will vary with respect to the orientation, accelerating voltage and aberrations. For instance, the (111) orientation of $SrTiO_3$ has a higher in plane atomic density than the (100), thus resulting in an even smaller thickness for the kinematical approximation to be valid.

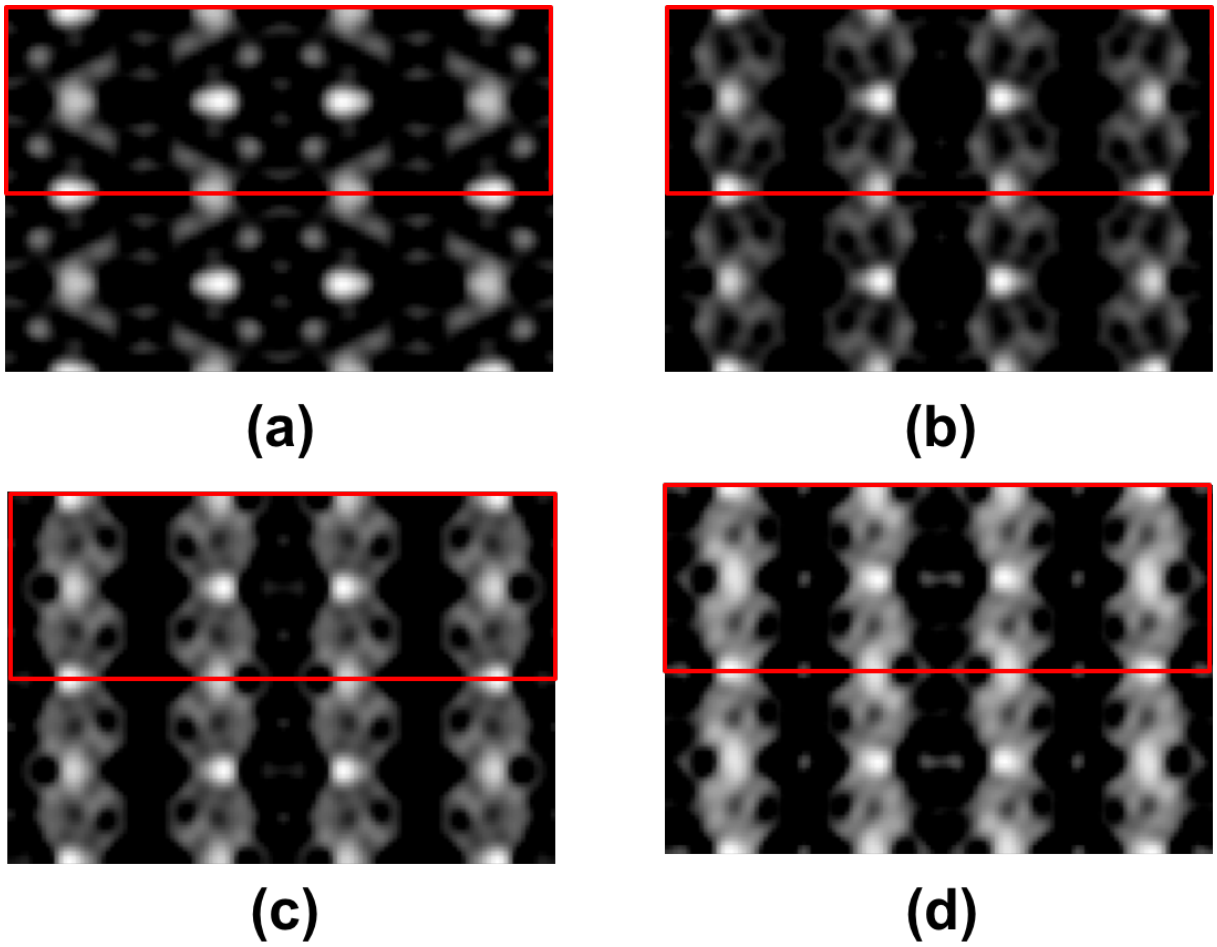

Figure 4.3. Simulated plan view images after bulk removal (defocus=6 Å) at thicknesses of (a) 4.15 nm, (b) 5.32 nm, (c) 6.49 nm and (d) 7.66 nm. Vibration of 0.4 Å (root mean squared) in the x- and y-directions has been added to all images to mimic experimental conditions. (The c(6×2) unit cell is outlined.)

In the case of c(6×2), the presence of an inversion center restricts the phase to either 0 or π and therefore allows for a more robust separation of the top and bottom surface. It is also worth noting that the phase is generally more important than the amplitude in obtaining representative images.

The implications of lacking an inversion center are discussed with the (3×3) surface reconstruction on $SrTiO_3$ in the following section.

4.3.2. (3×3) Surface Reconstruction on $SrTiO_3$ (111)

The separation of the top and bottom surface was done in two different plane group symmetries: p6mm and p3m1. While the actual structure is p3m1, the lack of inversion symmetry in p3m1 makes it difficult to interpret the resulting image. It is well established with direct methods of inverting diffraction data that sometimes higher symmetry space groups with inversion symmetry solve better, particularly if the symmetry reduction of the true structure is small; this was also found for surfaces [132].

Separation of the top and bottom surface was performed on the experimental image taken at a defocus of 5.4 nm. The resulting images in p6mm and p3m1 after the separation are given in Figures 4.4a and 4.4b, respectively. One common feature that is consistent across both the images is the high signal at the origin. In contrast, other experimental data including STM and DFT calculations [9] (see Figures 4.4c and 4.4d) show the opposite. This can be attributed to relatively thick samples, thicker than the sample on which the c(6×2) was observed. As seen in Figure 4.3, the restrictions on the thickness of the sample is strict and the higher in plane atomic density along (111) in comparison to the (001) direction is detrimental to the validity of kinematical assumptions.

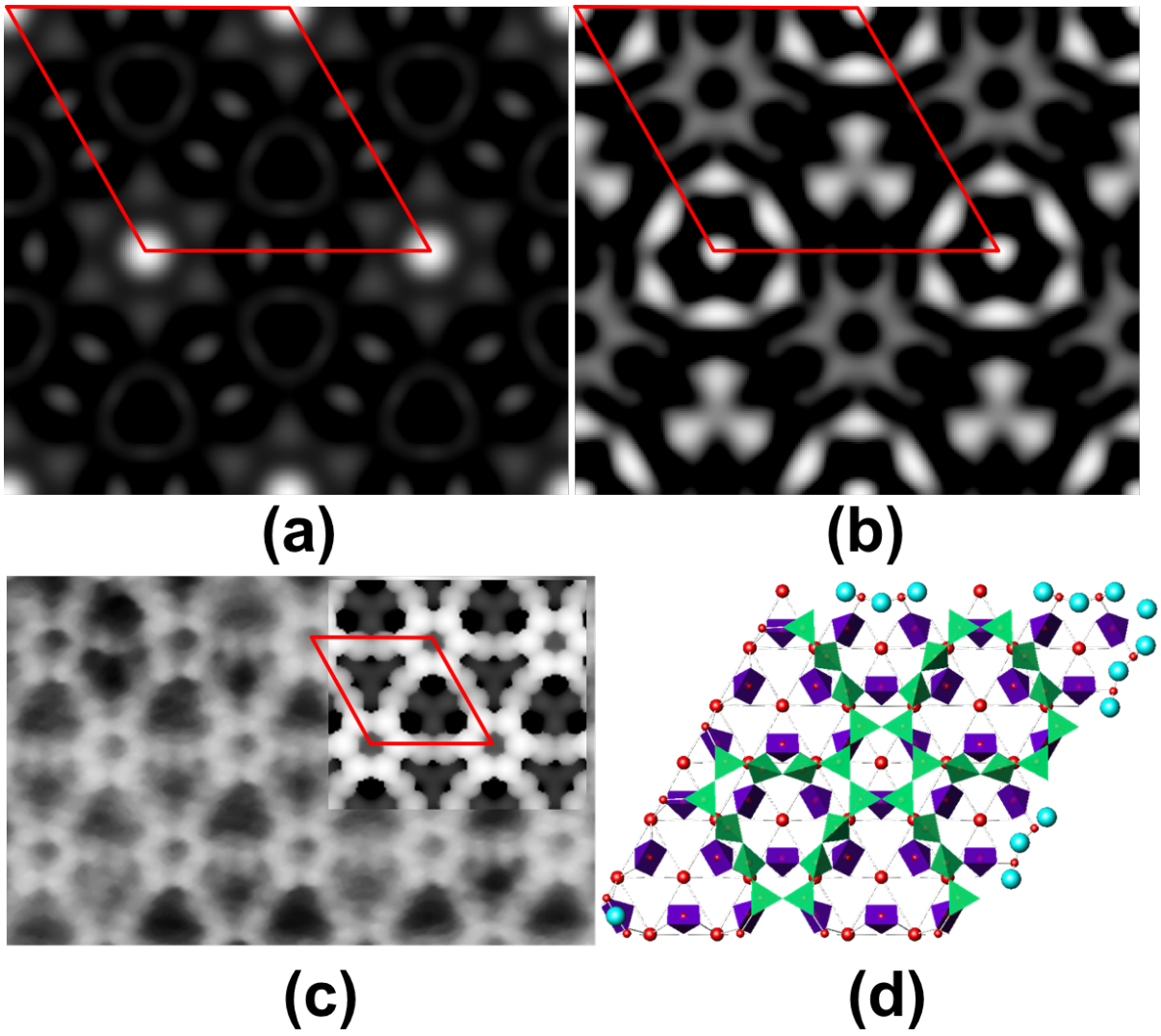

Figure 4.4. Experimental HREM image in (a) with p6mm symmetry and in (b) with p3m1 symmetry used for the separation of top and bottom surface after bulk removal. In (c) STM image with the simulation overlaid and (d) the corresponding structure of the (3×3) surface reconstruction on SrTiO3 on (111) [Subfigures (c) and (d) adapted from Ref. [9].] (The (3×3) unit cell is outlined in red.)

This was validated with HREM simulations performed on the (3×3). The simulations were performed with S3×3.cif (Supplemental Information in Ref. [9]) using the experimental parameters given in the methods section.

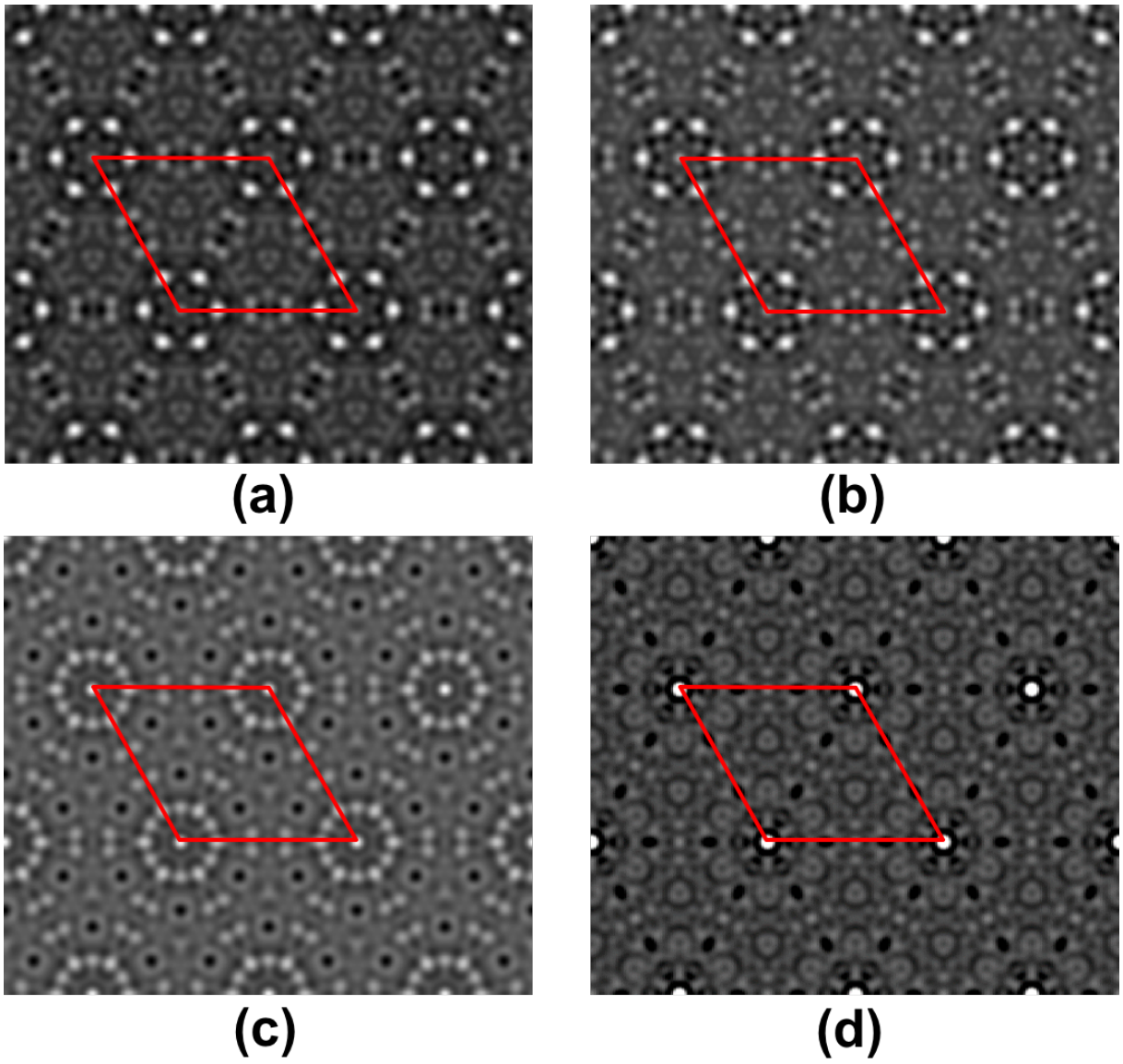

Figure 4.5. Simulated HREM images of the (3×3) surface reconstruction on $SrTiO_3$ (111) after bulk removal at varying thicknesses in (a) 5 nm, (b) 6.33 nm, (c) 7.7 nm and (d) 9.07 nm. (The (3×3) surface unit cell is outlined in red.)

The high intensity observed at the origin in the experimental plan view images is only seen in images of at least 6 nm thickness; the intensity at the origin increases with

thickness. Hence, the high intensity at the origin observed in the experimental image is the result of dynamical effects in thicker sample. In addition, the rotation of the six membered ring is not present in the simulated image below a thickness of 6 nm. The image simulated at 7.7 nm thickness starts to show intensity that is consistent with the 30° rotation of the hexagonal ring. Finally, the image simulated at a thickness of 9.07 nm shows the rotation of the six membered ring consistent with the inversion performed on experimental images. This further validates that the sample in the case of (3×3) was in the tens of nm.

For completeness, experimental images on the two extremes of the focal series were also analyzed to compare the separation under p6mm and p3m1. This is particularly important if there is inversion of phases during the separation and in some cases the resulting solution could be an example of Babinets principle, i.e. the inverse solution. The contrast on the two ends of the focal spectrum clearly demonstrate that the intensities are still consistent in p6mm. However, in the case of p3m1 there is a dramatic change in contrast. This can also be attributed to the presence of inversion center in p6mm thus making the intensities symmetric on both sides of the focal series.

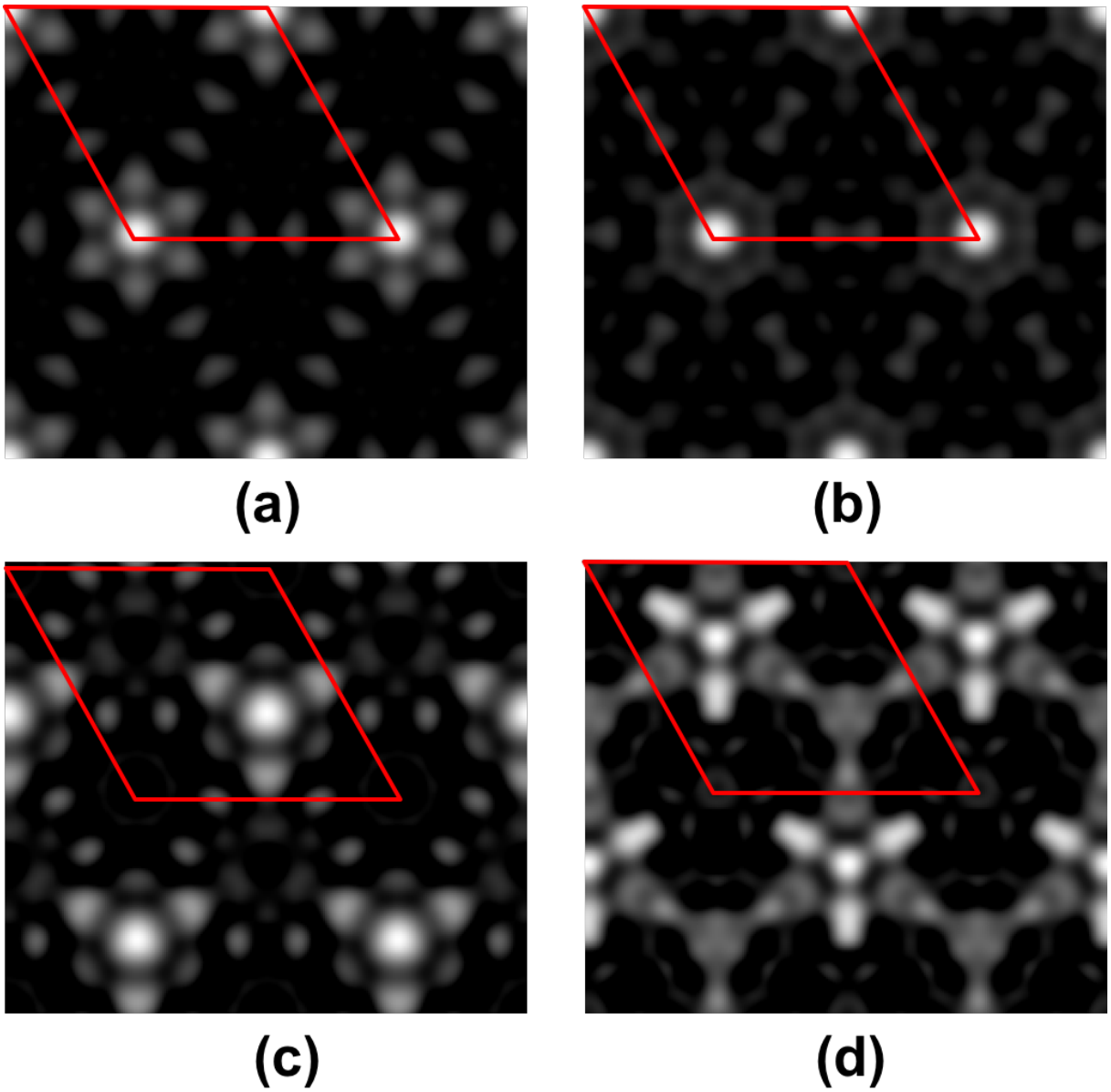

Figure 4.6. Experimental images after bulk removal and separation of top and bottom surface: with p6mm symmetry in (a) and (b) with defocus of experimental image at 41.3 nm and -27.5 nm respectively and with p3m1 symmetry in (c) and (d) with defocus of experimental image at 41.3 nm and -27.5 nm respectively.

4.4. Discussion

The primary limitation of the inversion method lies in the assumptions that the scattering is in the kinematical regime which as we have seen in the case of the (3×3) is not always valid. Implementation of dynamical scattering theory would be essential going beyond surface structures with inversion symmetry or a thin sample.; while this has been done to refine surface diffraction data (e.g. [103, 135–137]), it is rather tedious. Another challenge would be to account for differences in the top and bottom surface. There can be coexisting domains as well as different overlapping periodicities. While the inversion may still work if the surface structure of concern occupies a majority of the surface area as the plan view method works with the average of domains, this is not always the case. This gives rise to inconsistency in the results even for images acquired from the same sample but from different areas. For instance, different (n×n) reconstructions have been found to coexist on the $SrTiO_3$ (111) surface along with other difficulties due to long range disorder in the sample and glass like behavior of some of the surfaces [9]. Similarly, issues with the signal to noise (S/N) ratio from the surface is critical. It could well be that beyond a certain thickness, the S/N from the surface is insufficient for extracting any useful information.

Defocus difference between the top and bottom surfaces can also be incorporated into the kinematical model. Simulated HREM images of the (3×3) surface structure given in Figure 4.6 shows significant differences in contrast at 41.3 nm defocus and -27.5 nm defocus in p3m1 symmetry. The differences between images simulated at the same two

defocus values are minor in p6mm symmetry. This further reiterates the importance of inversion symmetry in the separation of top and bottom surface. Additionally, non-uniform beam damage on the top and bottom surface could also account for differences in the resulting contrast.

Plan view imaging possesses good surface signal, $1-3\%$ of the total signal, if the sample is thin. This method has been used for four systems, (7×7) on silicon (111) [93], (5×2)-Au on silicon (111) [106], (2×1) on $SrTiO_3$ [10] and c(6×2) on $SrTiO_3$ (001) [8], successfully. However, there are restrictions, the first being on the thickness of the sample. The second requirement which is subtler pertains to having inversion symmetry. The requirements for inversion symmetry can be thought of as imposing restriction on the sets of phases for different reflections thus making the method more robust and the resulting intensities more reliable. Thus, plan view imaging on the zone axis is a powerful tool when applied to imaging surface structures with proper address to the limitations and functionality of the method. An alternative is to tilt off the zone axis which will reduce dynamical effects, but introduces additional issues as the signal is weaker [110].

CHAPTER 5

Surface Heterogeneity in (001) oriented $KTaO_3$

Previous chapters have established that surface reconstructions on $SrTiO_3$ surface are a widely occurring phenomenon. $SrTiO_3$ is a "242" oxide according the formal valence of constituent species. It is also non-polar along the (001) direction. In spite of it being non-polar, the (001) surface still exhibits a number of complex surface structures. The next step in this work was to study the surface of polar oxides with different valence configuration. $KTaO_3$ is a "152" oxide and polar along the [001] direction. Subsequently, the (001) surface of $KTaO_3$ was studied.

5.1. Introduction

In recent years, there has been substantial interest in perovskites materials for various technological applications. Potassium tantalate ($KTaO_3$) is also a member of the ABO_3 family. In addition to being an incipient ferroelectric that does not undergo phase transition even down to 0 K [138], its dielectric constant monotonically increases to a value of about 4500 at liquid He temperatures [139]. A wide range of applications in catalysis [140, 141], growth [142–144], tunable microwave devices [139, 145–155] and air treatment [156] have been reported in literature. In addition, high interfacial conductivity has also been realized in $KTaO_3/LaTiO_3$ [157].

Defects and impurities play an important role in tuning the electronic properties of $KTaO_3$ [158–161]. Even though the crystal retains cubic symmetry ($a_0 = 3.898$ Å), it can develop polar microscopic regions [158] due to intrinsic defects such as Ta^{3+} or Ta^{4+} and oxygen vacancy [162] or impurities. Doping of $KTaO_3$ with Li, Na, Nb, Sr and Ca can result in the formation of a solid solution [158], thus changing the properties and resulting in ferroelectric behavior with variations in the Curie temperature.

Quantitative literature on the surface structures of $KTaO_3$ is close to non existent. Helium atom diffraction studies show the occurrence of a metastable periodic structure after cleaving (see Fig. 5.1). Diffraction experiments performed at different times after cleaving show diminishing intensities of the metastable phase [163]. However, no characterization of the metastable phase was done. Two stable domains of (2×1) reconstruction on $KTaO_3$ (001) surface have been predicted from theoretical calculations [163]. A recent work also reported precipitation of a tetragonal phase [164], but the origins of the precipitation were not explored.

In this work, the (001) surface of $KTaO_3$ along with the role of defects on the nucleation of secondary phases on the surface was explored. The origins of surface segregation and nucleation was studied primarily with TEM and complemented with other surface sensitive techniques. Finally, a wet chemical etching approach was taken to prepare clean, crystalline surfaces.

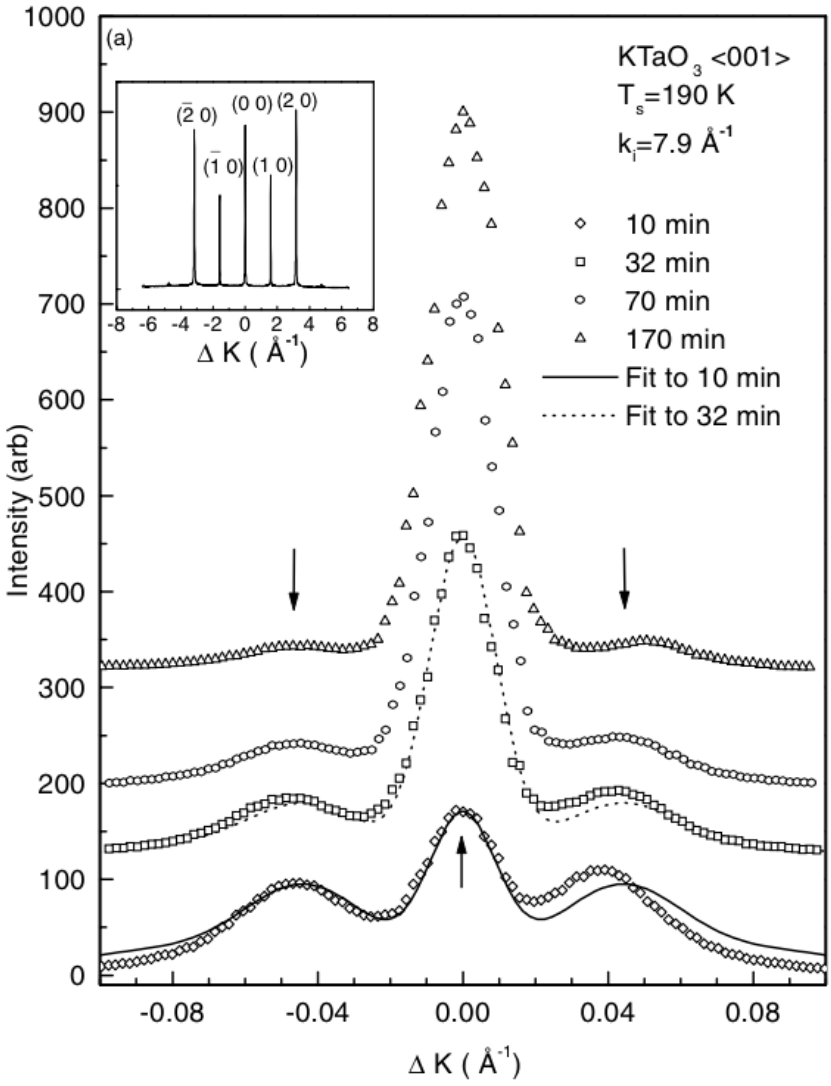

Figure 5.1. Four He diffraction scans (offset by 100 units) measured around the main peak at 10, 32, 70 and 170 min after cleaving (Adapted from Ref. [163])

5.1.1. Materials and Methods

Electron transparent samples were prepared from commercially available single crystalline substrates of (001) oriented $KTaO_3$ using the conventional method outlined in

Chapter 2. Electron microscopy was performed using Hitachi 8100, Hitachi HD-2300, JEOL2100F and JEOL JEM-ARM200CF instruments. AFM characterization was done using a Bruker FastScan. XPS characterization was performed using the Escalab 250 Xi system with a monochromated Al K-alpha.

5.1.2. Surface Characterization (001) $KTaO_3$

Electron transparent samples of $KTaO_3$ were first studied using TEM. Ion milled sample shows continuous thickness fringes in bright field and dark field images (Figure 5.2). Diffuse ring in the diffraction pattern indicates that the surface suffers from lattice damage and is disordered and amorphous (see Figure 5.2c).

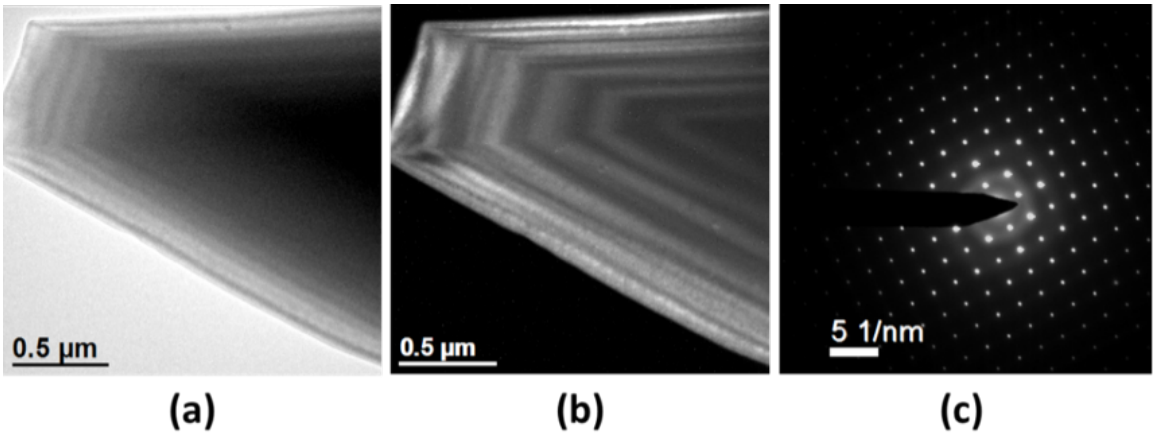

Figure 5.2. Bright field and dark field transmission electron microscopy images in (a) and (b) respectively, along with the corresponding transmission electron diffraction pattern in (c) of $KTaO_3$ (001) showing diffuse ring originating from the disordered surface after Ar+ ion milling.

Lattice damage is commonly observed in ion bombarded samples and some combination of chemical etching and annealing is used to clean and heal the surface. The samples

after ion milling were annealed at different temperatures in air to replenish the oxygen content in the material. Samples annealed at 500°C for 10 hours showed an amorphous and disordered surface (Figure 5.3a). On increasing the annealing temperature to 600°C (6 hours), the surface showed improved crystallinity with early signs of step-terrace nucleation (see Figure 5.3b). On further increase of the annealing temperature to 620°C (6 hours), formation of a second phase was observed (see Figure 5.3c).

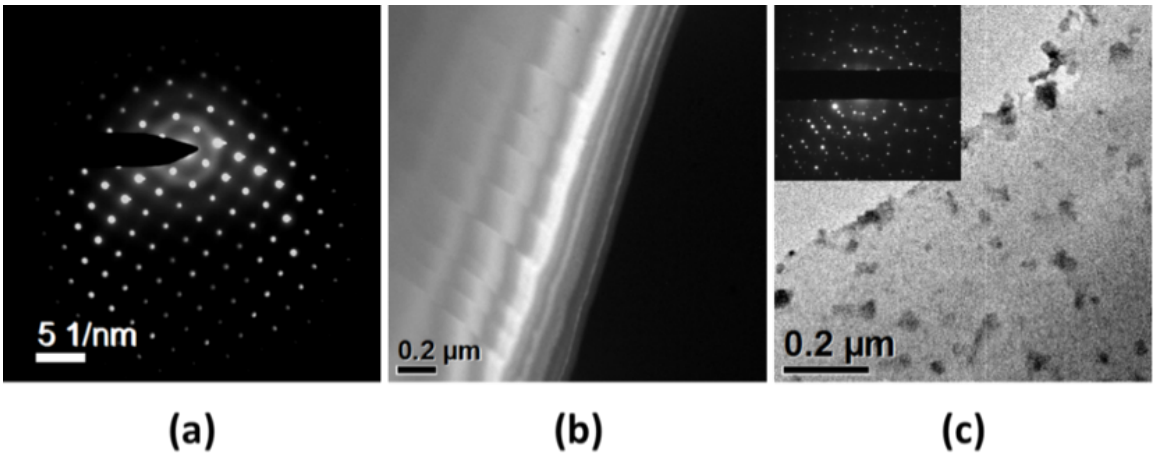

Figure 5.3. Off-zone diffraction pattern in (a) of a $KTaO_3$ (001) sample showing disorder of the surface after annealing at 500°C in flowing oxygen for 10 hrs. Dark field image of an area of a sample after annealing at 600°C in (b) showing some order and in (c) area of a sample annealed at 625°C showing the segregation of a second phase which appear as dark spots on the image. (The corresponding diffraction pattern is inset in (c)).

To further understand segregation and nucleation of the secondary phase, samples were subjected to a longer anneal at a higher temperature of 650°C. This resulted in the nucleation of well-defined nanoparticles on the surface as shown in Figure 5.4. Rod shaped precipitates are formed preferentially along the [100] and [010] directions on the

cubic substrate, and precipitation occurs only at the surface, i.e. island growth. (Referred hereafter as islands)

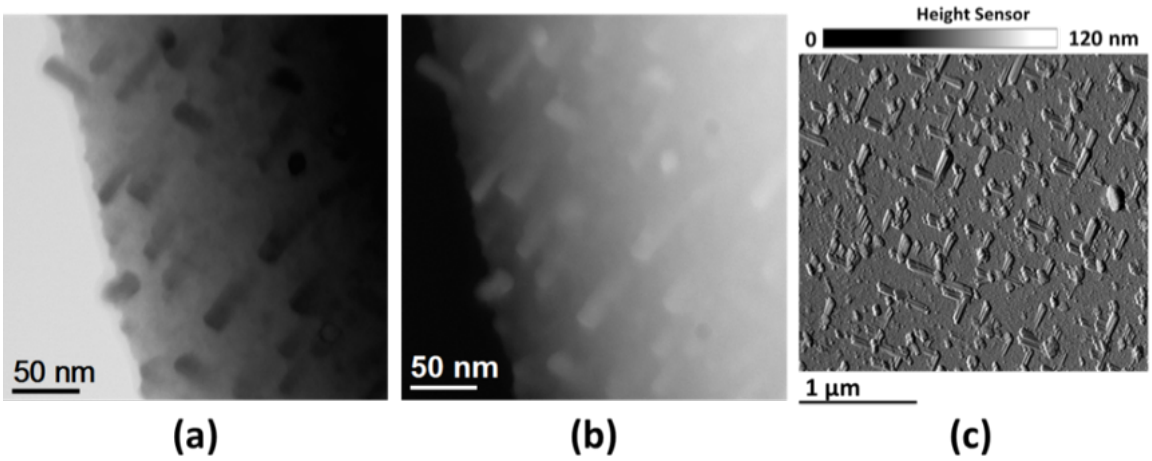

Figure 5.4. Bright field and annular dark field images in (a) and (b), respectively, of an area of a sample of $KTaO_3$ (001) after annealing in flowing oxygen for 12 hours at 650°C and atomic force microscopy image in (c) of the same sample (at lower magnification).

To better define the shape of the precipitates samples were annealed for an additional 12 hours. This resulted in well faceted, rod shaped islands (Figure 5.5). These islands covered approximately 5−10% of the surface as seen in the low magnification image in Figure 5.5a. These islands were 2−15 μm long and 20 nm to 1 μm wide.

Subsequently, TED was performed to identify the phase of these islands. Diffraction patterns along three different zone axis are given in Figure 5.6 along with the corresponding simulated kinematical diffraction pattern inset. The islands have a tetragonal crystal structure, and EDS indicated that the precipitates are potassium deficient (12−14 atomic %) and rich in oxygen (70−72 atomic %) and tantalum (21−23 atomic %). This

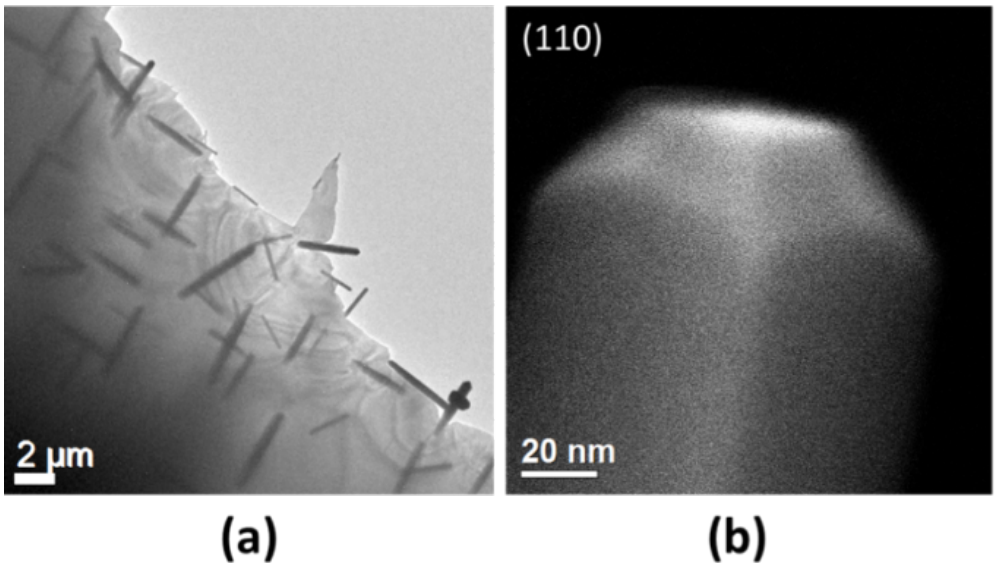

Figure 5.5. Low magnification image of an area of sample of $KTaO_3$ (001) with second phase after annealing at 650°C in flowing oxygen for 12 hours in (a) and the corresponding secondary electron image of one of the rods of the second phase is in (b) and shows faceted surfaces.

is consistent with the potassium deficient tetragonal phase, $K_6Ta_{10.8}O_{30}$ (a=12.569 Å, c= 3.978 Å) [165].

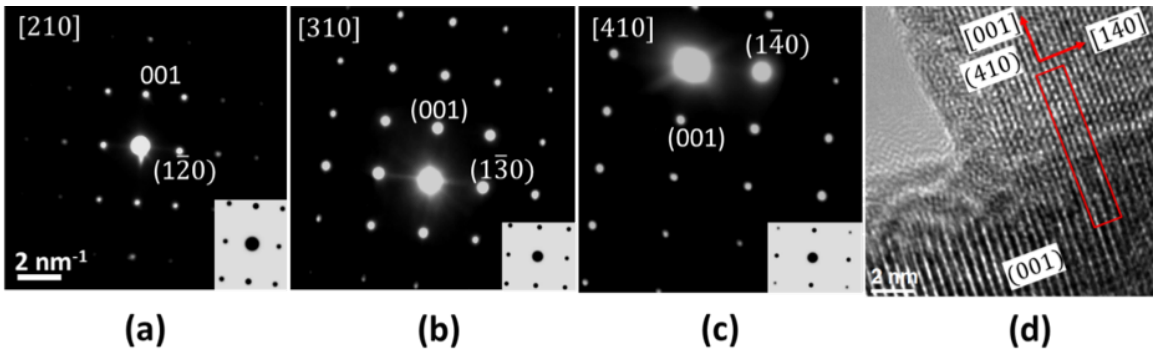

Figure 5.6. TED pattern along three different orientations (labeled in the top left of each frame) in (a) - (c) and the simulated kinematical diffraction pattern inset for the tetragonal phase – $K_6Ta_{10.8}O_{30}$. The corresponding HREM image in (d) shows the epitaxy between the tetragonal phase and cubic $KTaO_3$. (The red box marks the interface with 4:3 lattice match.)

Segregation of the tetragonal phase ($K_6Ta_{10.8}O_{30}$) accommodates the K deficiency and induced strain. The ratio of Ta:O is 1:3 in both the islands and underlying bulk $KTaO_3$. The in-plane orientation of the tetragonal phase was along $[1\bar{3}0]/[001]$ which provided a good lattice match with the [001] spacings of $KTaO_3$ (less than 1% strain).

The origin and mechanism of surface segregation were investigated by heating the samples in-situ in an electron microscope. Four TEM images along with the corresponding diffraction patterns are given in Figure 5.7 and the temperature is listed at the top of each frame. The actual temperature at the sample is likely lower as the thermocouple is closer to the heater than the sample. The frames show continuous changes in strain contrast with increasing temperature. As the temperature reaches 700°C, there is precipitation of islands on the surface. Segregation of the second phase relieves strain, equilibrates surface stoichiometry and minimizes interfacial and surface energies. This process is also assisted by vaporization of KO_x which has a vapor pressure of 10^{-9} Bar at 600°C [166] and atmospheric pressure. It is important to note that vaporization is significantly higher in ion milled samples in comparison to bulk samples with minimal surface damage. The rings in diffraction pattern from the second phase show spacings consistent with the tetragonal phase discussed earlier.

Buffered HF is often used to etch oxides crystal for creating a crystalline surfaces and also to create a specific termination. BHF etch has been reported to create atomically flat surfaces with unit cell steps in $KTaO_3$ [167]. Ion milled samples were etched with BHF and subjected to in-situ heating in an electron microscope to compare the differences in

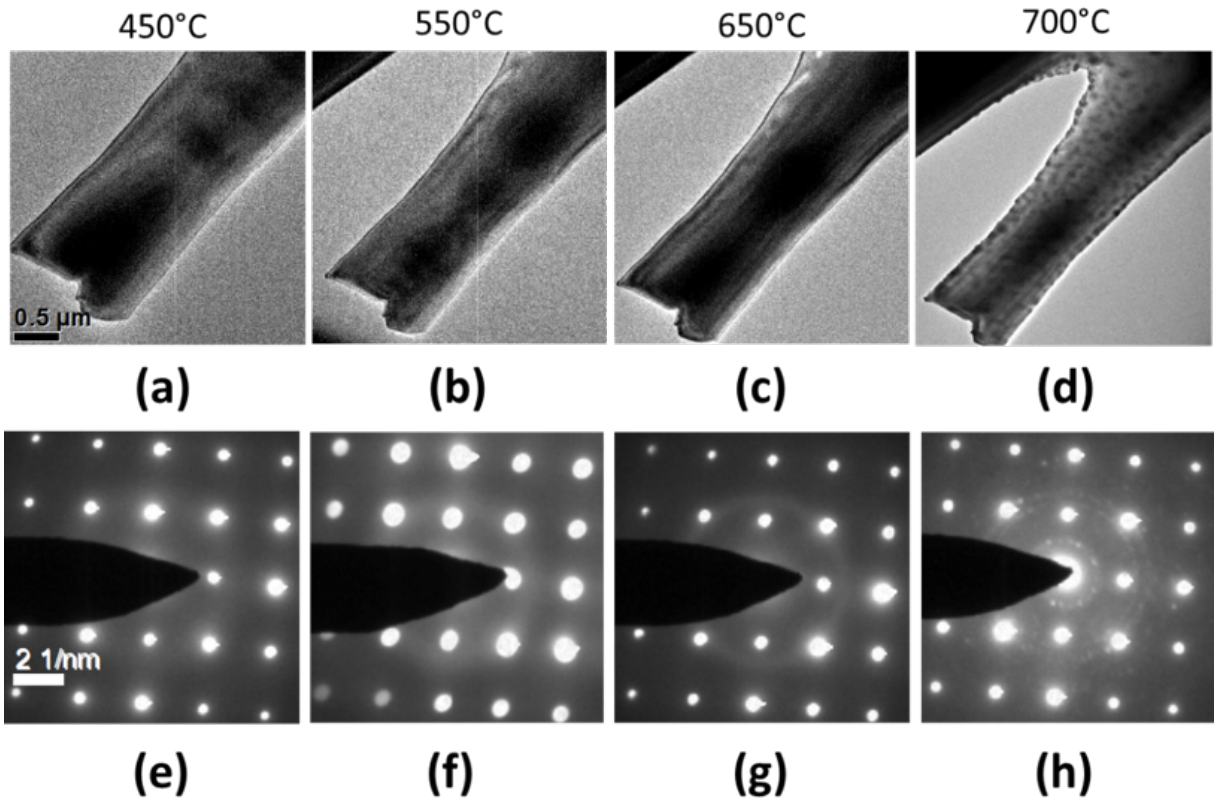

Figure 5.7. Bright field TEM images in (a)−(d) from in-situ annealing with the temperature listed on the top of each frame. The corresponding diffraction patterns are given in (e)−(h). Extra spots appear in the diffraction pattern in (h), corresponding to the segregation of island in (d) at 700°C.

surface morphology and segregation of the secondary phase on the surface with the as prepared sample. The TEM images in Figure 5.8 along with the corresponding diffraction patterns show gradual strain relief without the formation of the secondary phase even at much higher temperatures. This proves that the surface disorder in ion milled samples is the cause of KO_x vaporization and subsequent nucleation of second phase on the surface on annealing.

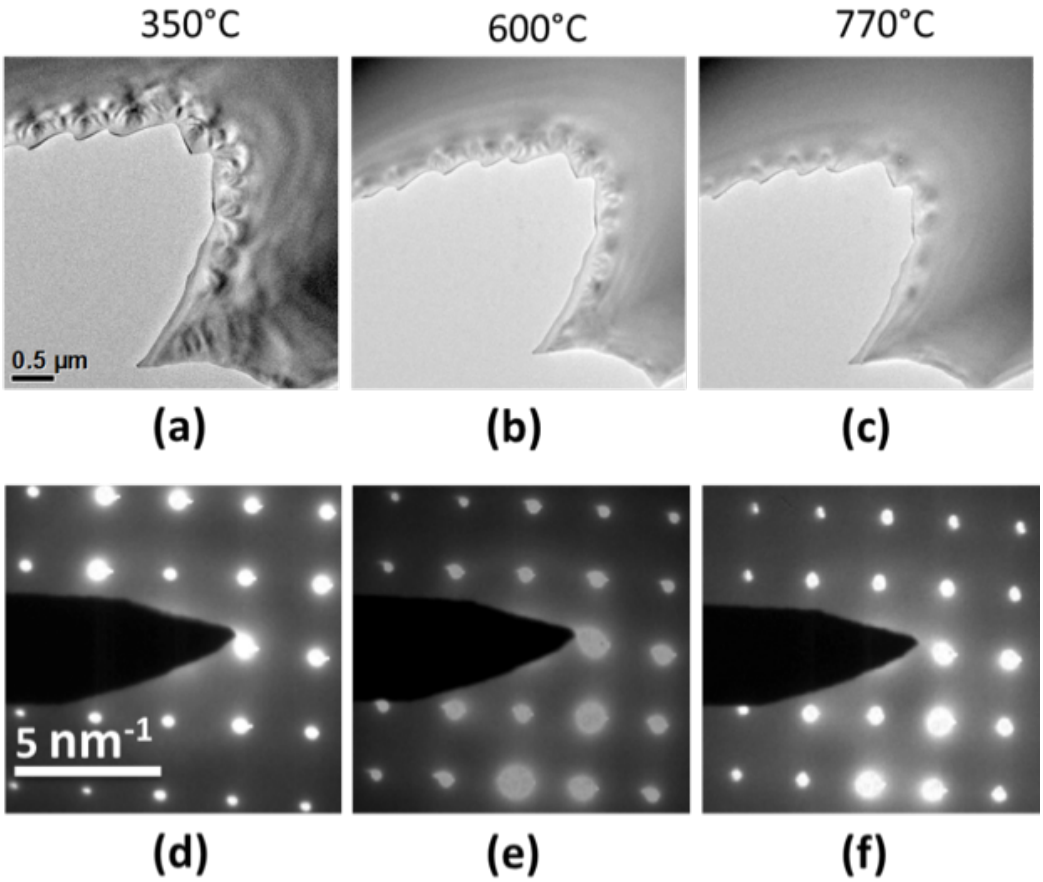

Figure 5.8. Bright field TEM images in (a) - (c) from in-situ annealing of BHF etched $KTaO_3$ (001) sample with the temperature listed on the top of each frame. The corresponding diffraction pattern of (a) - (c) is given in (d) - (f), respectively.

5.2. Conclusion

Surface heterogeneity in oxides and other binary compounds is a general phenomenon. In the case of $KTaO_3$, this happens in two steps involved in processing these samples: ion milling and annealing. Ar^+ ion milling is widely used to create thin samples for electron microscopy or to clean samples. The energies used in ion milling (2 - 6 keV) is detrimental to the surface stoichiometry and creates defects and disorder. These defects are

usually eradicated by etching or annealing techniques. The choice of etchant and annealing conditions will vary depending upon the material. In-situ annealing experiments in $KTaO_3$ demonstrate the role of surface disorder and off-stoichiometry on the precipitation of secondary phase. EDS results indicate depletion of K, whereas the ratio of Ta to O remains the same as in $KTaO_3$. This suggests that the ordering of second phase is driven by the deficiency in K which results from preferential sputtering of K during ion milling and vaporization of K in the form of an oxide during annealing.

CHAPTER 6

Surface Studies of (110) Oriented Neodymium Gallate

The previous chapter demonstrated some of the complexities that arise due to selective ion sputtering and surface damage during sample preparation in $KTaO_3$. Neodymium gallate ($NdGaO_3$) is another "332" oxide that was studied as a part of this dissertation. Surface dynamics similar to $KTaO_3$ were also observed on $NdGaO_3$; the underlying mechanism of surface heterogeneity was different.

6.1. Introduction

Neodymium gallate is commonly used for applications in growth [168–171] and optoelectronics [172]. It has a $GdFeO_3$ type structure with in plane lattice constant of 3.86 Å. There are distortions in the GaO_6 octahedron which drive the structure to orthorhombic symmetry (space group 62) [173] (see Figure 6.1). (110) oriented $NdGaO_3$ has been used as growth substrate for a number of oxides including (La,Ca)MnO_3 [168, 169] and $LaBaCo_2O_{5.5+\delta}$ [171]. $LaBaCo_2O_{5.5+\delta}$ has been extensively studied for its exotic electronic and magnetic properties resulting from the mixed valence states of Co and the ordering of CoO_5 or CoO_6 [170]. Anisotropic strain at the interface of $LaBaCo_2O_{5.5+\delta}$ on (110) oriented $NdGaO_3$ exhibits directional metallicity [170]. It also exhibits a metallic interface with other perovskites including $SrTiO_3$ [174] and $NdNiO_3$ [175].

For growth applications, it is essential to have a good lattice match and stability at high temperatures ($\sim$600$-$800°C). $NdGaO_3$ is the only lanthanide gallate that does not undergo a structural phase transition below 900°C [176]. Furthermore, the low dielectric loss tangent of $NdGaO_3$ makes it an ideal substrate for semiconductor growth and electronic applications [177]. In spite of the wide range of applications and interesting electronic properties, literature on surface studies of $NdGaO_3$ is lacking.

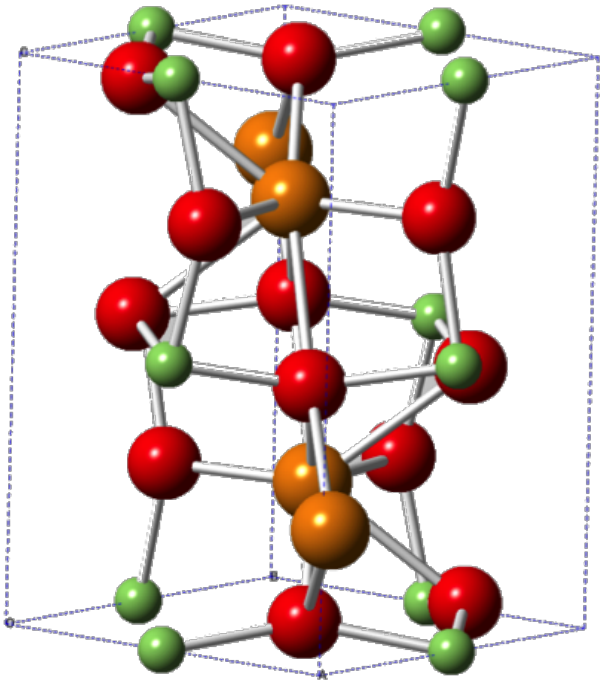

Figure 6.1. Unit cell of $NdGaO_3$. (Ga in green, Nd in orange and O in red)

6.2. Previous Surface Studies

A few chemical treatments and annealing results have been reported in the literature but the analysis is mostly qualitative [178–180]. A recent work by Cavallaro et al. [180]

indicated that the (110) surface of $NdGaO_3$ is A-site terminated following a high temperature anneal. Their conclusions were based on low energy ion scattering (LEIS) integrated intensity ratio of Ga peak to Nd peak as a function of annealing time at 1000°C (see Figure 6.2). These studies ignore the presence of any reconstruction even though their sample preparation involves annealing at 1000°C.

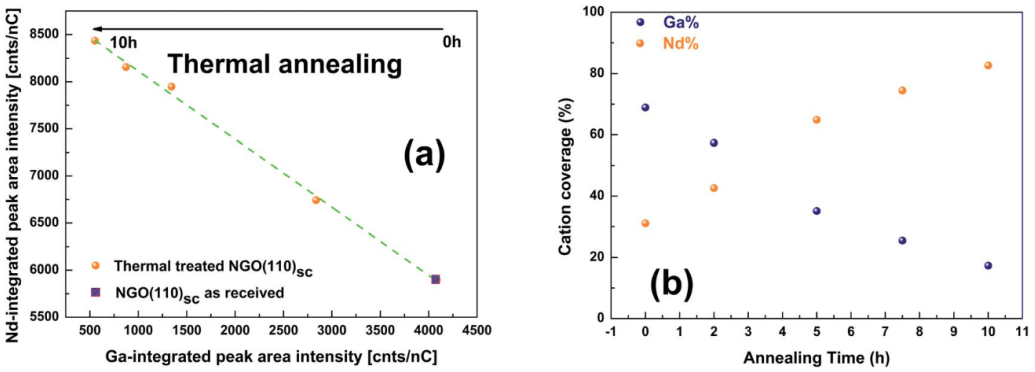

Figure 6.2. Four single crystals treated in static air at 1000°C for 2, 5, 7.5 and 10 hours respectively analyzed by 5 keV Ne^+ primary ion species. (a) shows the LEIS integrated area-intensity of neodymium peak with respect ot gallium peak for each sample. The integrated peak area intensity of the gallium has been corrected by a calibration factor (k=3) and used to calculate the cation coverage percentage of the sample surfaces (b). (Adapted from Ref. [180])

It is clear that annealing of $NdGaO_3$ samples at 1000°C results in the enhancement of Nd concentration on the surface. However, the underlying mechanism by which the surface accommodates Nd enrichment was not explored. The work done as a part of this thesis used TEM, AFM and XPS in conjunction with in-situ TEM to study surface phenomena in (110) oriented $NdGaO_3$.

6.3. Results

Electron transparent samples were prepared using the conventional method outlined in Chapter 2 from (110) $NdGaO_3$ oriented single crystals of dimension $10\times10\times0.5$ mm^3.

TEM characterization of samples after ion milling showed unusually periodic strain fields around the edge of the sample in both BF and DF images (see Figure 6.3).

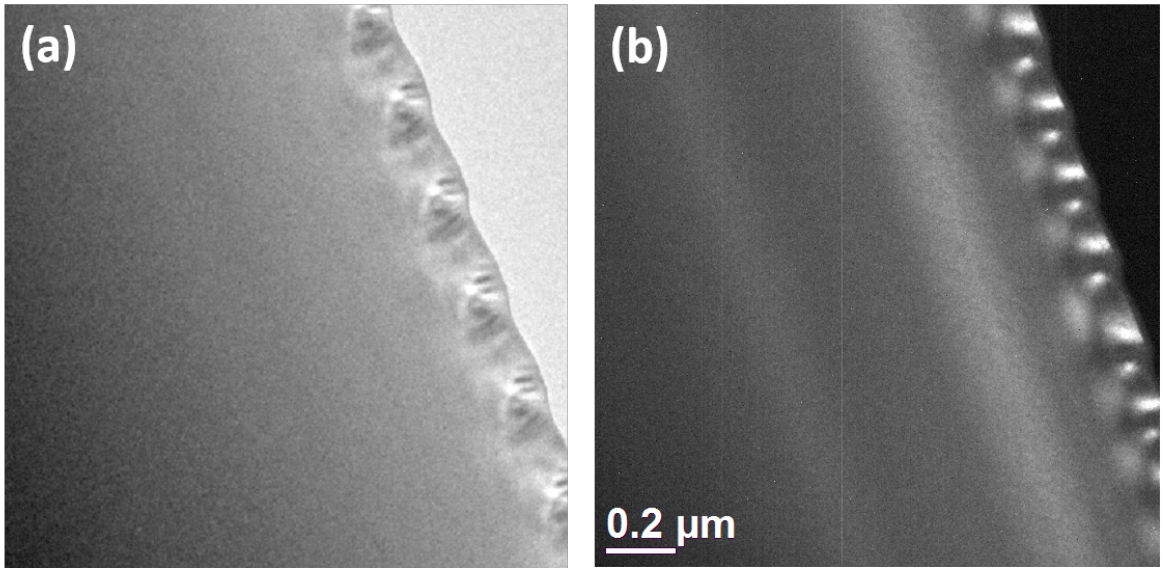

Figure 6.3. (a) Bright field and (b) dark field TEM images of (110) $NdGaO_3$ sample after Ar^+ ion beam milling.

Lattice damage and bend contours are commonly seen in ion milled samples. However, it is unusual for the resulting strain fields in the sample to be periodic. The period of bends are of the order of 100 nm. Electron diffraction pattern acquired from the area of the sample shown in Figure 6.3 is given in Figure 6.4. A diffuse ring in the diffraction pattern indicated that the surface was amorphous and disordered owing to the damage imparted during ion milling. There are no additional spots in the diffraction pattern

that would indicate the segregation of a second phase. As a consequence, the intensity oscillations seen in the images are only due to strain in the sample.

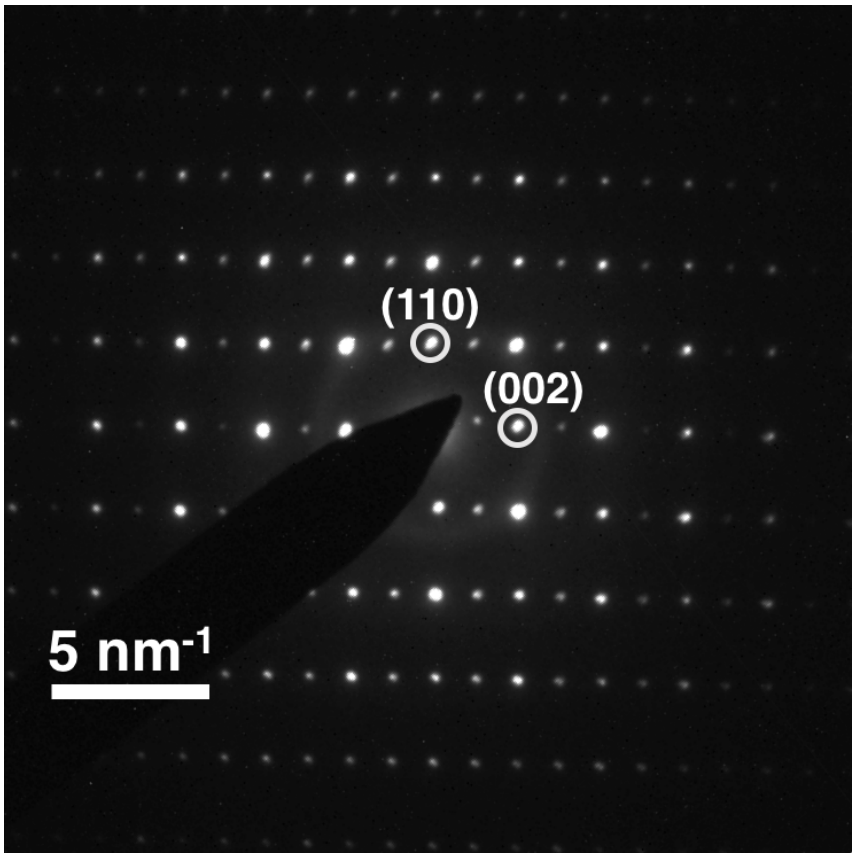

Figure 6.4. Transmission electron diffraction pattern of a (110) oriented single crystalline sample of $NdGaO_3$ after ion beam milling. Diffuse ring in the diffraction pattern is indicative of an amorphous surface. Labeled reflections in the diffraction pattern are marked with white circles.

After ion beam milling these samples were etched in BHF to clean the surface. BHF is widely used for cleaning of $SrTiO_3$ surfaces and also for preferential TiO_2 surface termination [24]. Electron diffraction of etched $NdGaO_3$ samples showed a clean and crystalline surface. Angle resolved XPS showed that the surface was stoichiometric which implies

that the BHF etching is not preferential towards either Nd or Ga. These samples were subjected to annealing at 1050°C for 10 hours in flowing O_2.

Annealed samples of $NdGaO_3$ showed a high degree of surface heterogeneity with segregation of a second phase as islands. These island ranged from $10 - 100$nm (see Figure 6.5). Even though there is no preferred orientation for the growth of these islands, their density is greater at the edges of the sample. It is likely that the stoichiometric changes and damage in the material has greater effects at the edge and hence segregation at the edge is preferred.

Surface segregation could also couple with the periodic strain present in ion milled samples. In many cases the segregated island maintained the same periodic interfacial strain with the substrate as seen in ion milled samples. (see Figure 6.6)

The density of islands on the surface was found to increase with annealing time. Additional experiments were performed to determine if the segregation primarily arises from the amorphous material on the surface or if island growth and nucleation is supported by bulk diffusion. First samples were etched in BHF for 30 sec and annealed for a short duration (∼30 min) at 1000°C. TEM imaging of such samples reveled two important findings:

(1) Loss of Ga is significant at elevated temperatures in highly strained samples

(2) The nucleation of a second phase initiates at the edge with periodic strain modulations.

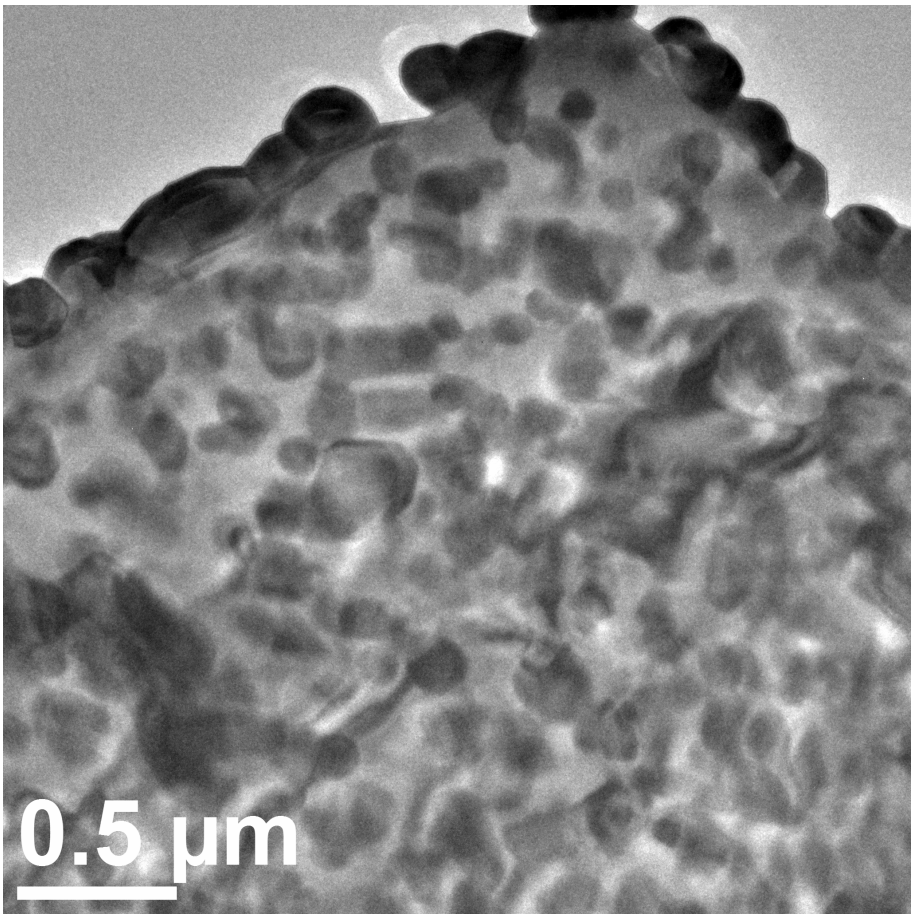

Figure 6.5. Surface segregation of islands on (110) oriented $NdGaO_3$ after annealing at 1050°C for 10 hours in flowing oxygen. The sample was ion milled to electron transparency prior to annealing.

6.3.1. Loss of Gallium

Even though the melting point of $NdGaO_3$ is 1600°C [178], stress can induce significant loss of Ga in samples with amorphous surface and lattice damage. This phenomena is well known in Sn alloys and solders where stress induced whisker and hillock formation is commonly observed [181–183]. Ga loss can be seen in some areas of a sample that was annealed for a short duration (indicated by red arrows in Figure 6.7b). Radiation damage

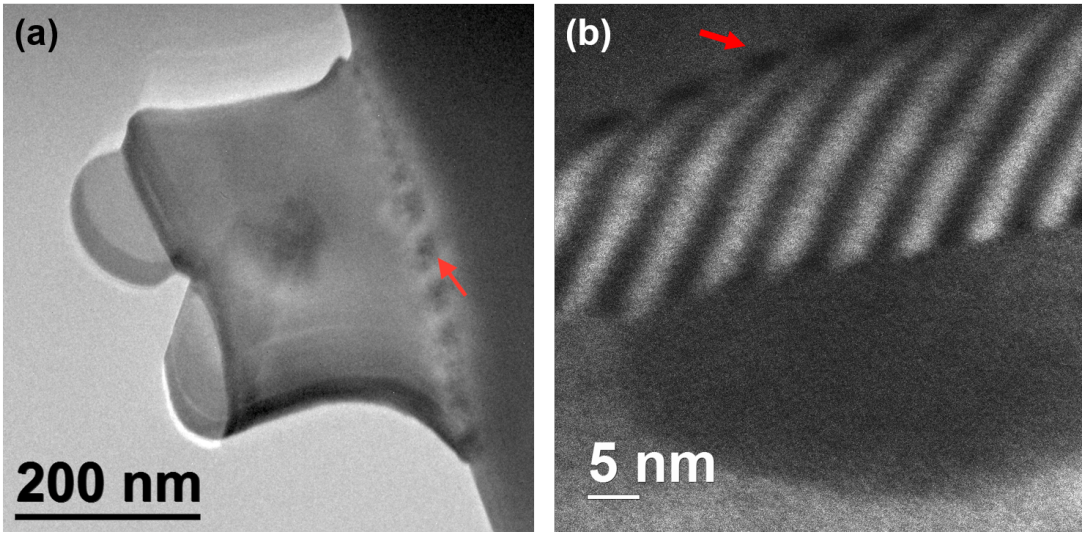

Figure 6.6. Segregation of islands on (110) oriented $NdGaO_3$ after annealing at 1050°C for 10 hours in flowing oxygen. In (a) low magnification BF TEM image and in (b) high magnification LAADF image showing Moiré fringe due to the superimposition of the lattice of the second phase and the substrate. (The strain at the edge of the substrate is marked by a red arrow.)

due to the electron beam can also be detrimental to the Ga content in the material (see Figure 6.7a). A whisker marked by a red arrow in Figure 6.7a was seen to grow in real time inside the microscope. Segregation of second phase is therefore directly linked to the loss of Ga from the material.

6.3.2. Nucleation of Surface Islands

Samples annealed for 30 min also provide information on the early stages of nucleation and growth. The growth primarily initiates at edge of the sample where lattice damage is severe. Segregated island maintain the same periodicity as the strain fields seen in samples after ion milling.

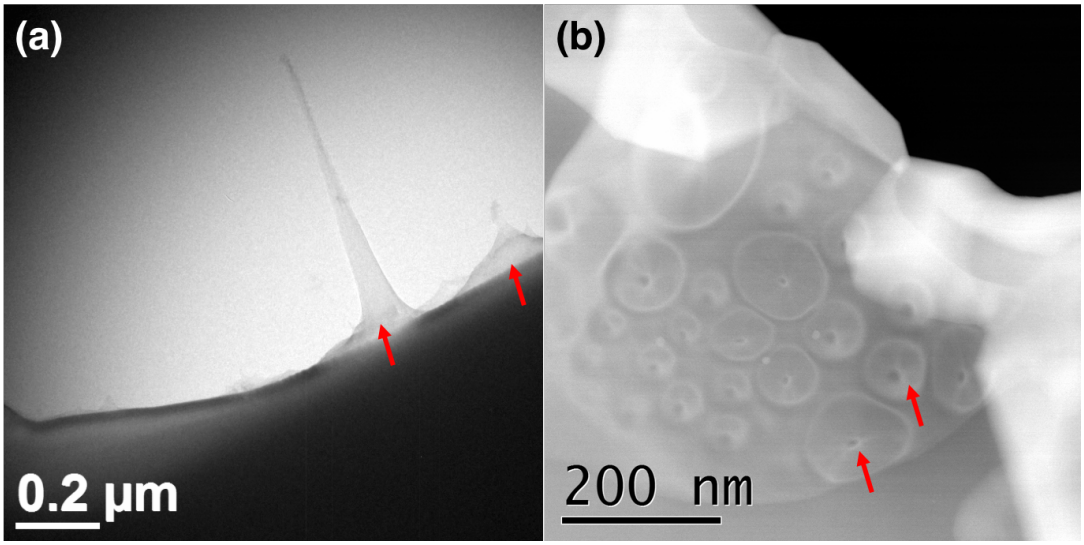

Figure 6.7. In (a) BF TEM image of an area of a sample of $NdGaO_3$ showing stress induced Ga whisker formation and (b) LAADF image showing Ga whiskers at multiple areas of the sample. (Some of the whiskers are marked by a red arrow.)

Even though the sample shows island growth at the edge, areas further away from the edge show clear ordering in the form of steps and terraces (see Figure 6.8). This leads to an important conclusion that for ordering the surface of $NdGaO_3$, anneals of 30 min or even less are sufficient.

Finally, identification of the phase of the island was done using TED and HREM imaging. The phase that segregates is a result of Ga depletion and stoichiometric heterogeneity on the surface. All reported structures with Nd, Ga and O as the constituent elements were checked with the experimental data. The diffraction pattern in Figure 6.9 and the HREM images in Figure 6.10 were consistent with a hexagonal structure with Si impurity and no Ga. The stoichiometry and space group of the new compound was found to be $Nd_{9.33}(SiO_4)_6O_2$ and $P6_3/m$, respectively. The structure of the phase is given in Figure

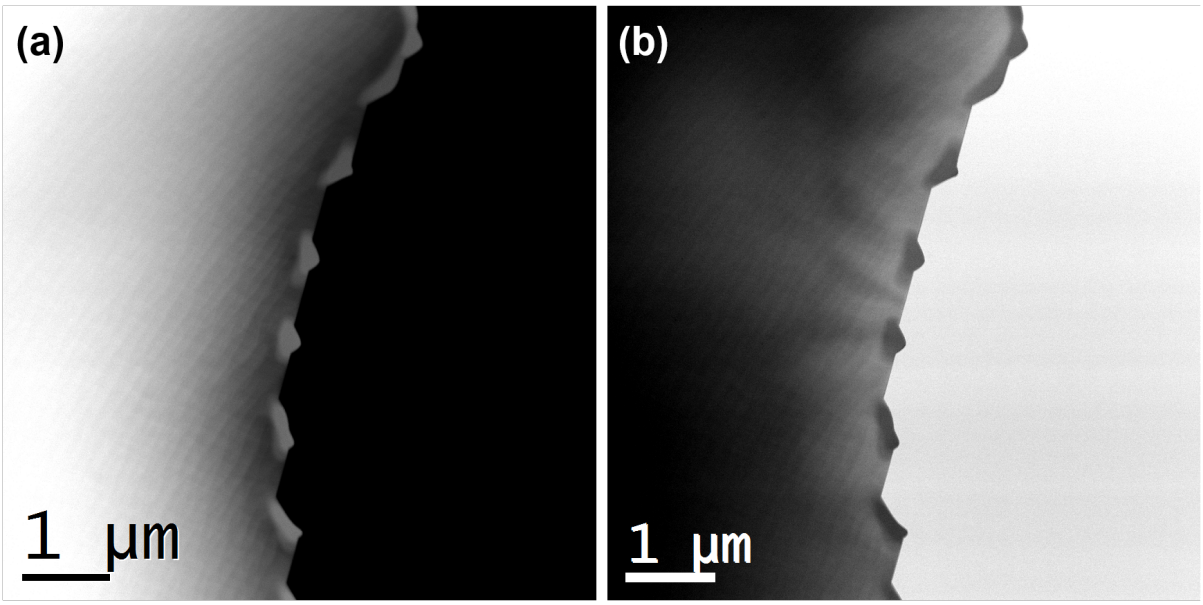

Figure 6.8. (a) LAADF and (b) ABF image of an area of a sample of (110) oriented $NdGaO_3$ showing early stages of island growth at the edge.

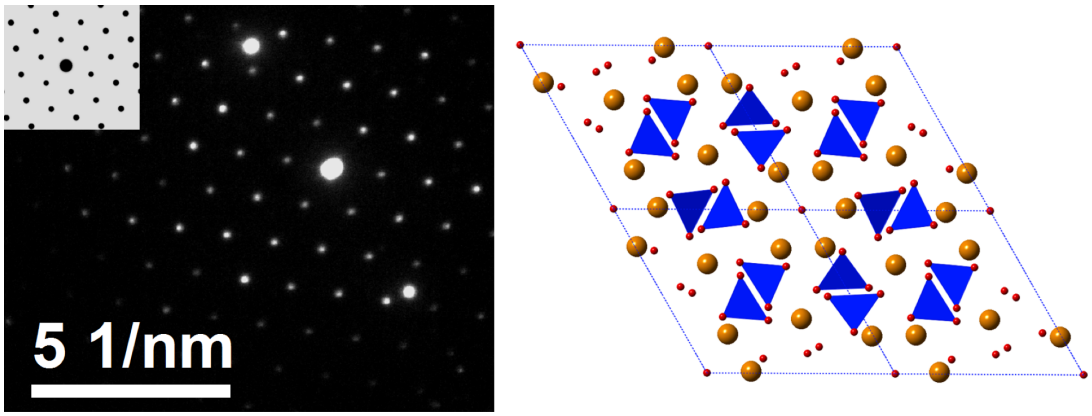

Figure 6.9. In (a) TED pattern of (001) oriented surface precipitated island of $Nd_{9.33}(SiO_4)_6O_2$ with simulated kinematical TED pattern inset. (b) Structure of $Nd_{9.33}(SiO_4)_6O_2$ along the (001) direction. (Nd atoms in yellow, SiO_4 tetrahedra in blue and O atoms in red.)

6.9b. It is a known phase and has been reported in literature [184]. Si impurity in the structure could be from either the SiC slurry used in polishing the samples or the quartz

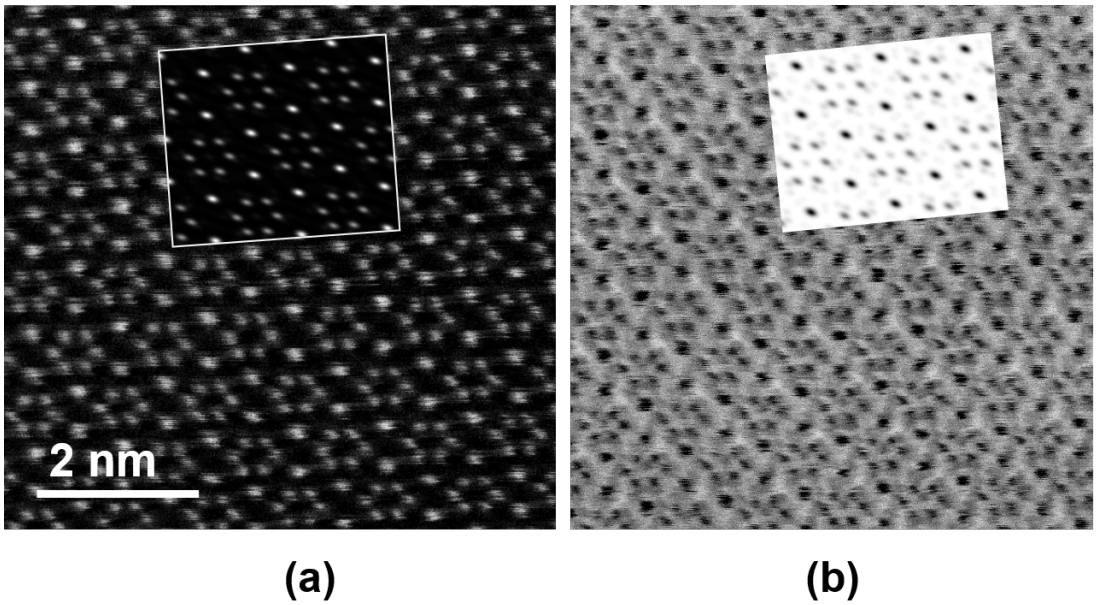

Figure 6.10. (a) HAADF and (b) ABF images of islands of $Nd_{9.33}(SiO_4)_6O_2$ on the surface of (110) oriented $NdGaO_3$ with corresponding simulations inset.

tube in which the samples were annealed. Si contamination has not posed any problems of surface segregation in samples of other materials which were prepared in the same way as $NdGaO_3$. This indicates that the contamination is facilitated by chemical reaction of the Ga deficient disordered surface with either the SiO_2 or SiC from the tube and slurry respectively.

6.4. Conclusion

Hence, surface heterogeneity observed in $NdGaO_3$ is driven by stress induced Ga loss and subsequent incorporation of Si impurities. In addition, strain induced in the sample during ion beam milling provides nucleation sites for surface segregation. Based on the evidence in $KTaO_3$ and $NdGaO_3$, it appears that surface heterogeneity in perovskite oxides

can be a general phenomenon. It is therefore essential to have a crystalline surface free of amorphous residue and disorder before subjecting the material to high temperature anneal. 30 min annealing of ion milled samples shows clear ordering of step terraces (see Figure 6.9) in areas away from the edge of the sample.

CHAPTER 7

Flexoelectric Effect in Lanthanide Scandates

7.1. Background

Many materials exhibit novel responses to external stimuli such as electromagnetic fields, deformation and temperature. These couplings between materials properties and external stimuli lead to interesting phenomena such as the well known ferroelectric effect and piezoelectric effect. A lesser known of these is the flexoelectric effect, resulting from the coupling of strain gradient and electric polarization. First observed in solids by Bursian et al.[185] the term flexoelectricity was coined in the field of liquid crystals [186] and subsequently adopted for solids [187] and also biological membranes [188]. It occurs in many materials [23, 188–190] including those that are centrosymmetric. Unlike the piezoelectric effect where the material system is non-centrosymmetric, breaking of symmetry in flexoelectric effect arises from strain gradient.

Flexoelectricty has direct applications in micro- and nano-electromechanical systems including actuators and bimorphs. It can also influence electronic imprinting [191, 192], internal bias in thin films [193], nanoferroics [194] and dead layers in ferroelectric thin films [195]. Flexoelectric coupling can change domain walls and interfaces in ferroelectrics[196, 197] and ferroelastics[198, 199] control defects [200] and change nanoindentation hardness

of ferroelectrics [201, 202]. It can also impact dielectric properties [193], photocurrents [203] and phonon spectra [204]. A number of other potential applications including flexoelectric energy harvesting [205, 206], photonic crystals [207] and strain sensors [208] have been reported. In spite of numerous applications, the theoretical understanding and experimental methods to probe the effect have not been well established.

The following sections will discuss the underlying theory of flexoelectric effect and experimental methods for the measurement flexoelectric coefficient. Finally results from exploratory surface studies conducted as a part of this thesis that led to the observation of large flexoelectric effect inside an electron microscope in lanthanide scandates will be discussed.

7.2. Theory of Flexoelectric Effect

Much of the early theoretical work on flexoelectric effect has been based on phenomenological theory. The flexoelectric effect is represented by a fourth rank tensor.

$$\mu_{klij} = \left(\frac{\partial P_i}{\partial \left(\partial u_{kl} / \partial x_j \right)} \right)_{E=0} \tag{7.1}$$

Landau phenomenological approach can be used for a mathematical treatment of the effect [23]. The potential energy density can be written as:

$$\Phi_G = \frac{1}{2\chi} P^2 + \frac{c}{2} u^2 - \nu P u - f_1 P \frac{\partial u}{\partial x} - f_2 u \frac{\partial P}{\partial x} - PE - u\sigma \tag{7.2}$$

where, χ is the dielectric susceptibility, P is the polarization, u is the displacement fields, E is the electric field, ν is the piezoelectric coefficient, f_1 and f_2 are the flexocoupling coefficients and σ is the stress.

In the absence of piezoelectric contributions ($\nu = 0$), the potential density equation given in equation 7.2 can be written as:

$$\Phi_G = \Phi - \frac{f_1 + f_2}{2}\frac{\partial(uP)}{\partial x} \tag{7.3}$$

where,

$$\Phi = \frac{1}{2\chi}P^2 + \frac{c}{2}u^2 - \frac{f}{2}\left(P\frac{\partial u}{\partial x} - u\frac{\partial P}{\partial x}\right) - PE - u\sigma \tag{7.4}$$

Application of Euler Lagrange minimization with respect to u and P leads to the constitutive equations:

$$P = \chi E + \mu\frac{\partial u}{\partial x} \tag{7.5}$$

$$\sigma = cu + \frac{\mu}{\chi}\frac{\partial P}{\partial x} \tag{7.6}$$

$$\mu \equiv \chi f \tag{7.7}$$

where, μ is the flexoelectric coefficient.

Recent theoretical understanding has advanced at the nanoscale due to dynamic polarization theory [209–212] and DFT [213, 214] as well as at the continuum level with elasticity theory [215, 216]. Additionally, there have been a number of papers analyzing the mechanics at the micron [217, 218] and nano scale [219, 220] as well as in thin films [200].

7.3. Experiemental Measurements of Flexoelectric Effect

From the experimental front, there are two commonly used methods for the measurement of the flexoelectric coefficient Both methods involve the application of an oscillatory strain gradient on the sample to induce flexoelectric polarization. The method developed by Cross et al. [221] used a speaker with one end of the sample clamped whereas the method developed by Zubko et al. [222] used a three point bending setup. Recently, piezoresponse force microscopy has also been used for the measurement of local flexoelectric response [196, 223–225].

Most experimental measurements have used small strain gradients ($\sim$0.02$-$0.1 m^{-1}) and small deviation from equilibrium position. The early work by Bursian et al. [185] observed curvature in $BaTiO_3$ films due to the application of an electric field. Even though the authors did not call this phenomena flexoelectric effect, this is the first report

of flexoelectric effect in solids. It is important to note that their observation was of the converse flexoelectric effect as they applied polarization to induce a strain gradient. A 2.5 μm thick film of $BaTiO_3$ was measured to have a curvature of 150 m^{-1}. They also predicted that in films with thickness in the nanometer regime, the curvature would be of the order of 10^6-10^{10} m^{-1}[185]. In addition to thickness, the flexoelectric effect is also strongly dependent on the dielectric function. As a result, a strong temperature dependence of flexoelectric coefficient is expected. Flexocoupling can also be enhanced around phase transition temperatures. In spite of the theoretical predictions, none of the existing literature demonstrate a direct experimental evidence of such high curvature values; there is one indirect measurement of comparable curvatures [226].

7.4. Methods

TEM samples were made from commercially-purchased [110] oriented single crystals of $DyScO_3$ using the conventional method outlined in Chapter 2. Electron transparent samples were annealed in air for 12 hours at 1050−1200°C. TEM characterization was complimented with AFM, XPS, UPS, REELS, and the surface structure was theoretically modeled using DFT calculations. DFT calculations on lanthanide scandates were carried out by Prof. Laurence Marks.

Muffin tin radii of 1.68, 1.82, and 2.02 were used for O, Sc and Dy, respectively, to minimize inclusion of tails of the O 2p density perturbing the calculation of the exact-exchange corrections inside the muffin tins for Sc and Dy. The plane-wave expansion

parameter RKMAX in the code was 6.5. Atom positions and bulk optimized lattice constants were calculated using the on-site hybrid method [227] with the PBESol functional [228]. For the surface a 70.000×7.925×7.9357 Å cell was used containing 260 atoms (92 unique) with P121/m1 symmetry and a 4×4×1 mesh. The electron density and atomic positions were simultaneously converged using a quasi-Newton algorithm 18; the numerical convergence was better than 0.01 eV $(1\times1 \text{ cell})^{-1}$ surface cell. All calculations were with ferromagnetic unit cells, which is appropriate for the samples in an electron microscope; the difference in positions for ferromagnetic and anti-ferromagnetic ordering was minimal, as would be expected since this is a weak energy term. On-site corrections of 0.80 for the Sc 3d and 0.5 and 0.30 for the Dy 5d and 4f were approximately optimum. The values of the corrections for the d electrons were critical to obtaining atomic positions close to those found experimentally; that for the 4f were not. Inclusion of spin-orbit coupling was tested and while this changed fine details of the electronic structure for the 4f electrons, it was otherwise insignificant.

7.4.1. XPS Fitting and Parameters

XPS fitting was done using the Powell method to deconvolve the peaks using a fixed Gaussian-Lorentzian (GL) mixing parameter of 30%, which is critical for addressing the asymmetries in XPS spectra. A maximum of 20,000 iterations was used to converge the fit to 1×10^{-6} counts per second. For Dysprosium, 3d peaks were used and doublets were fitted with the following constraints:

- Area of Dy $3d_{3/2}$ = 0.7 × Area of Dy $3d_{5/2}$
- Binding energy of Dy $3d_{3/2}$ = Binding energy of Dy $3d_{5/2}$ + 38 (±0.1) eV

The Sc2p doublets were fitted with the following constraints [229]:

- Area of Sc $2p_{1/2}$ = 0.50 × Area of Sc $2p_{3/2}$
- Binding energy of Sc $2p_{1/2}$ = Binding energy of Sc $2p_{3/2}$ + 4.5 (±0.1) eV

7.5. Results

The samples after annealing were studied with a Hitachi H-8100 TEM. The first session on the microscope was extremely challenging as the sample charged immensely. The sample was stabilized at very low beam flux. While focusing the electron beam on a thin rod shaped edge of the sample, the rod appeared to bend. The first thought was that the observation was an artifact of electron beam interaction with the charged sample. However, extensive characterization was done and the bending was determined to be associated with an induced polarization owing to the loss of secondary electrons; i.e. the flexoelectric effect.

This is the first direct experimental observation of large flexoelectric effect at the nanoscale. Within a transmission electron microscope, thin rods of lanthanide scandates (the first set of experiments were on $DyScO_3$) bend by up to ninety degrees with a radius of curvature of about 10 μm when charged positively by the loss of secondary electrons. The bending was reversible with the electron flu, and not associated with any dislocations, twinning or similar changes in the oxide.

As illustrated in Figure 7.1, when the electron beam was condensed onto a thin rod of $DyScO_3$ it charged positively and bent downwards with a radius of curvature of about 10 μm; if the beam was not centered on the rod it bent down and to one side.

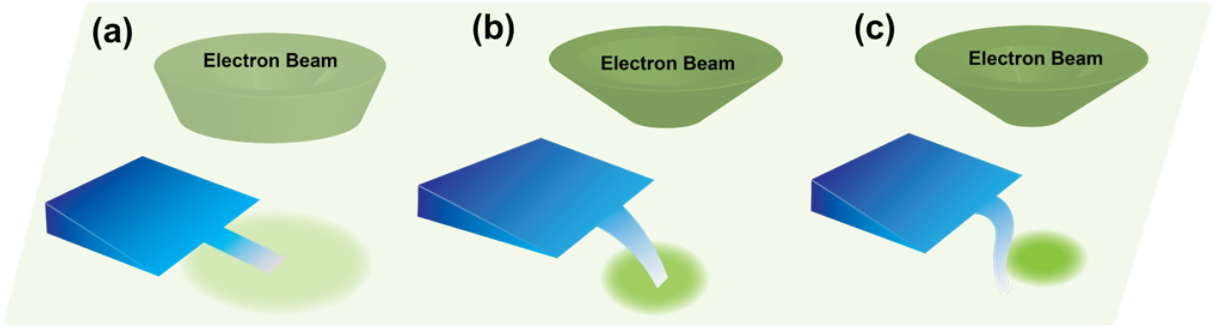

Figure 7.1. Illustrations of samples electromechanical response under the electron beam in: (a) where the sample is not bending due to low beam current, (b) where the sample is bending down with a focused beam centered on the sample and (c) where the sample is bending down and sideways with the focused beam centered on one side of the sample.

Since this work involved the use of multiple characterization techniques and theoretical calculations, the results are presented in different sections for organizational purpose. First, the experimental observations are presented and subsequent sections present detailed characterization of the material followed by discussion.

7.5.1. Bending Inside Transmission Electron Microscope

Figure 7.2 shows a number of single frames from a movie (M1) [230] where the electron beam was defocused from (b) to (h) on a thin $DyScO_3$ rod of about 50 nm thickness. The rod which was originally not bent in (a) charged and bent rapidly, and as the electron flux was reduced returned towards the original unbent form. The angles as well as the electron

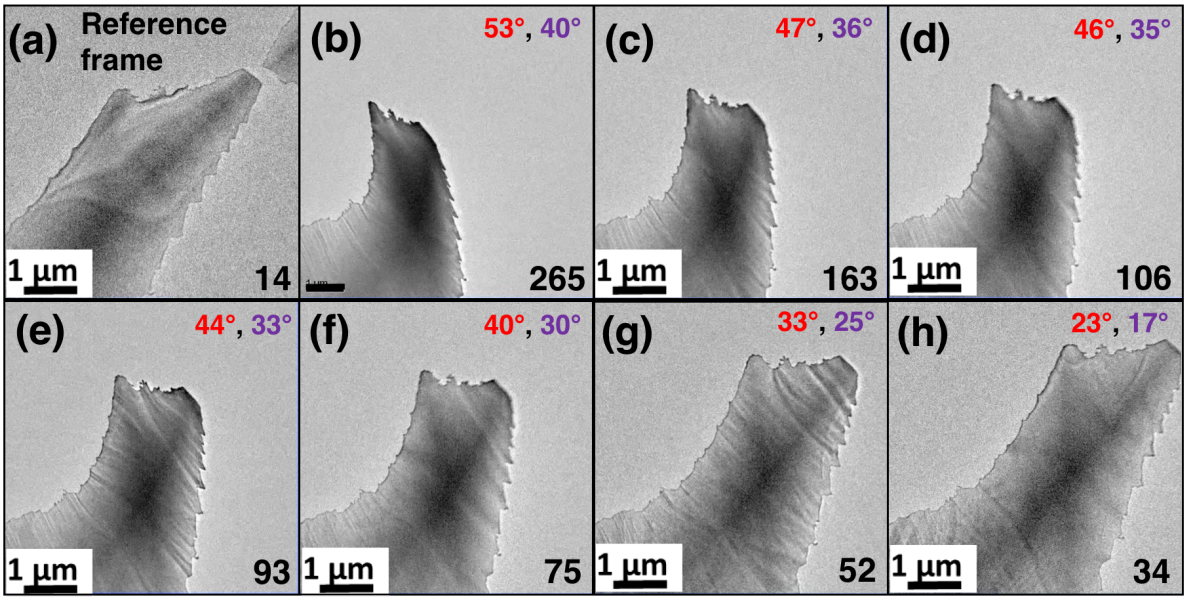

Figure 7.2. Eight frames taken from a movie showing a decrease in downward bending of the sample with a gradual spreading of the electron beam from (b) to (h). The approximate electron flux (e/nm^{2}s) calculated using a quantum yield of 0.2 is given in the bottom right corner of each frame. The corresponding bending angles along the length (in red) and width (in purple) of the rods are given at the top right corner of each frame.

fluxes are given on the Figure. The direction of the bending can be determined by the change in the Fresnel fringes at the edge that become brighter indicating downward bending. The electron fluxes were 1−100 electrons/nm^{2}s, significantly lower than $10^6 - 10^4$ electrons/nm^{2}s typically used for high resolution imaging. In many cases, the process was reversible although with too severe bending the rods could fracture (Movie M2 [230]). The same phenomenon was observed for about fifty different rods from twenty different samples, and was also observed for $TbScO_3$ and $GdScO_3$. There was no dependence upon the crystallographic direction of the rods with the caveat that the thin direction was always [110]. The process appeared to be elastic with no evidence of dislocation or phase

transition. The bending was on the time scale of the video recordings, suggesting adjustments of the charge took 10−1000 msec although there might be much faster processes taking place. However, we were limited by the slow frame rate of the camera.

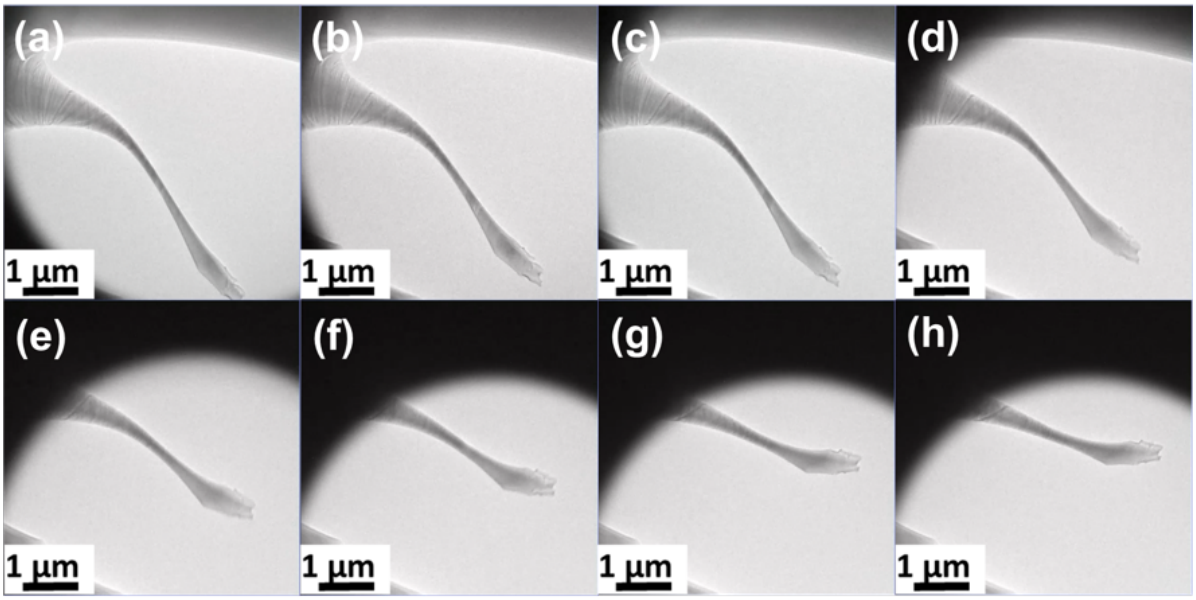

Figure 7.3. Eight frames of transmission electron microscopy images with the electron beam focused to one side of the sample. The beam is centered towards the top half of the frame in (a) and gradually shifted towards the bottom of the frame in (a) through (h). The full data is in Supplemental Movie M3.

A second set of results shown in Figure 7.3 also single frames from a movie (M3) [230], was when the electron beam was not centered on the rod, but to one side. In this case, the rod bent both down and away from the beam, reversibly in terms of the sideways motion. For the high energies used herein charging is expected be net positive, owing to the loss of secondary electrons. These results are consistent with more positive charge on

the top surface of the sample and that closest to the beam center resulting in a non-zero electrical polarization between the two surfaces.

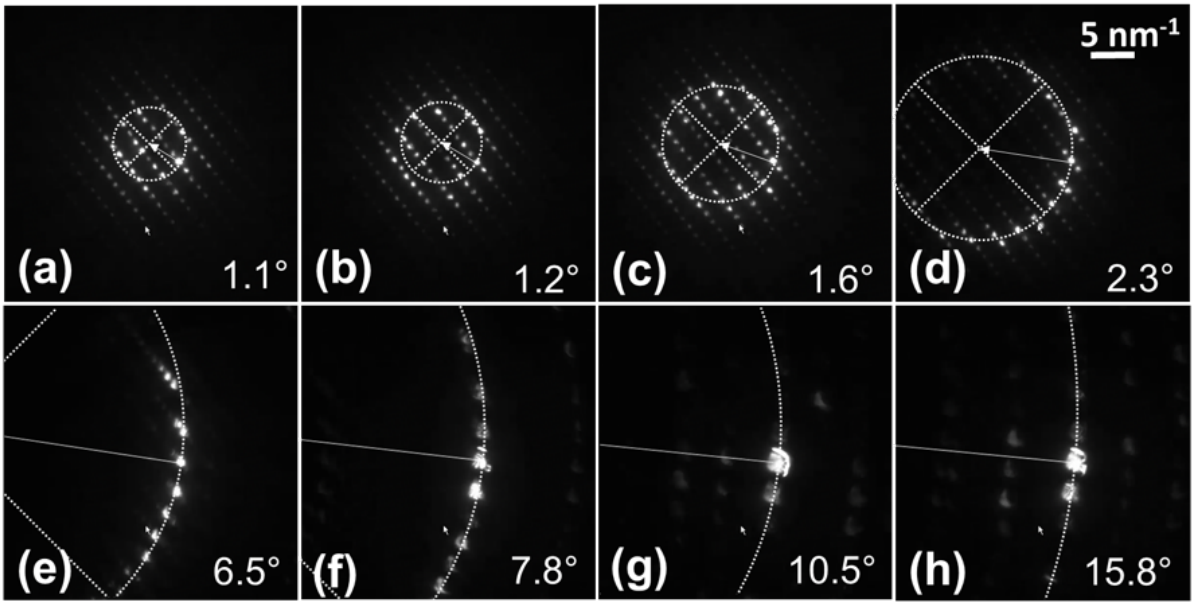

Figure 7.4. Eight frames of transmission electron diffraction pattern with the electron beam being defocused (reduced flux) from (a)−(h) showing the bending of the sample in reciprocal space. There is no discernible change (± 0.1 nm^{-1}) in the distance between the transmitted beam and the mouse pointer which was used as a stationary reference point. A solid white arrow (shown in white, off the pattern in (e)−(h)) is drawn from the transmitted beam to the center of the approximate Laue circle. Tilt angles from the [110] zone axis in degrees are given in the bottom right corner of each frame based upon fitting circles to the strong spots on the Laue circle.

Diffraction patterns were collected to test whether the incident beam was bent due to the charged sample (see Figure 7.4). The diffraction patterns in Figure 7.4 are also frames from a video [230]. For the results shown, the beam was first focused and the sample tilted by 22° to approximately the [110] zone. The sequence in Figure 7.4(a)−(h) is defocusing the beam (i.e. lowering the electron flux), and shows tilting of the sample by a total of

about 15.8°. While there was a slight deflection of the beam, it was several orders of magnitude smaller than the bending of the sample. Frames at different time intervals were used to estimate the bending. An approximate Laue circle was drawn tracing the reflections with higher intensity compared to the surrounding reflections. Subsequently, a line drawn from the direct beam to the center of the approximate circle was used to estimate radius of the circle (r) and hence the amount of bending. The bending angle, , in radians is

$$\theta = \arcsin(\lambda r) \tag{7.8}$$

where λ is the wavelength of the 200 keV electrons in nm and r is the radius of the approximate Laue circle in nm^{-1}.

For completeness, changing the microscope focus did not lead to large shifts, also consistent with only minimal bending of the electron beam.

A second possibility is that magnetic fields of approximately 2T in the microscope play a role. $DyScO_3$ is antiferromagnetic below 4K, paramagnetic above [231] and low temperature measurements [231] mentions that the magnetic force was large enough to rotate samples inside their instrument. We therefore performed experiments in electron microscopes with fields of about 5 Oersted at the sample and observed essentially the same bending (Figure 7.5), ruling out magnetic contributions as the dominant term.

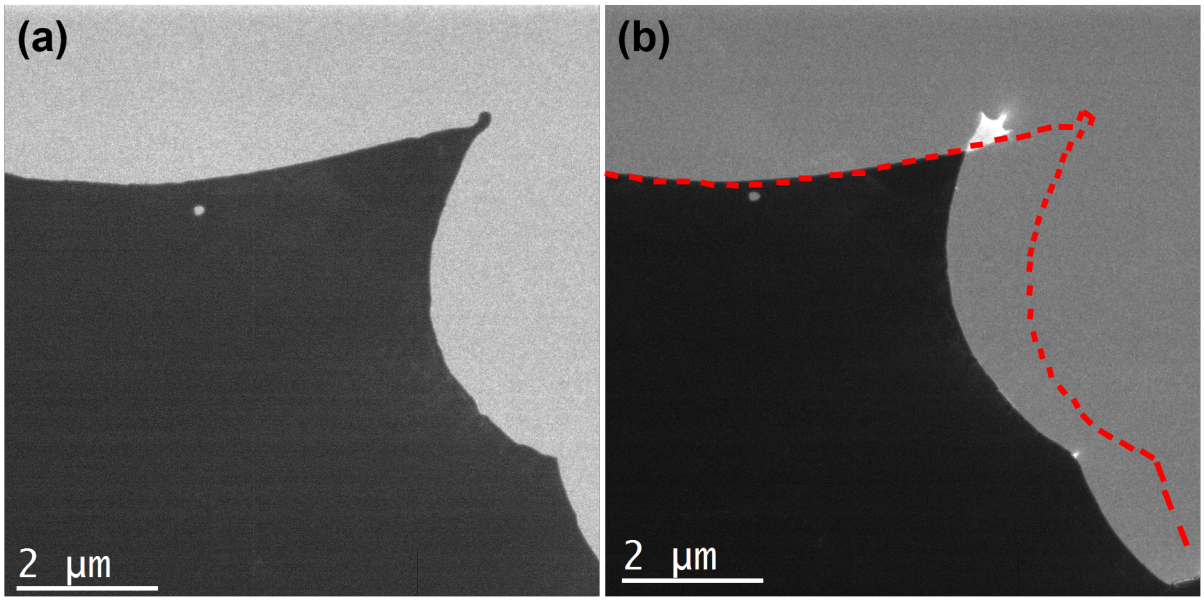

Figure 7.5. Transmission electron microscopy image of an area of a sample of $DyScO_3$ with converging beam from (a) to (b) performed in a low field (5 Oersted) microscope. Dashed red line in (b) traces the edge of the sample as it is in subfigure (a).

A third possibility is that the phenomenon depends upon the presence of occupied minority 4f states at the valence band maximum. Whereas $DyScO_3$ has two minority electrons, $TdScO_3$ has one and $GdScO_3$ none and all three showed approximately the same bending. While the minority 4f states may play a role, their presence is not required.

The diffraction patterns (Figure 7.4) showed a low diffused background with no evidence of additional reflections indicating few bulk defects and a well-ordered 1×1 surface which, from the annealing conditions, we expect to be valence neutral.

7.5.2. Surface Characterization

AFM imaging (Figure 7.6) confirmed that the surface was flat with monatomic steps of 4 nm in height. The 1×1 [110] surface of $DyScO_3$ is similar to a (2×2) [001] of a simple perovskite, so it does not have to be a simple bulk termination. Angle resolved XPS measurements indicated that the surface was scandium rich with two Sc atoms per 1×1 surface cell in the outermost layer (Figure 7.6), similar to the well-established double-layer reconstructions on $SrTiO_3$ [001]. For completeness, XPS measurements indicated that the annealed sample prior to examination had very little to no chemisorbed hydroxide on the surface (Figure 7.7).

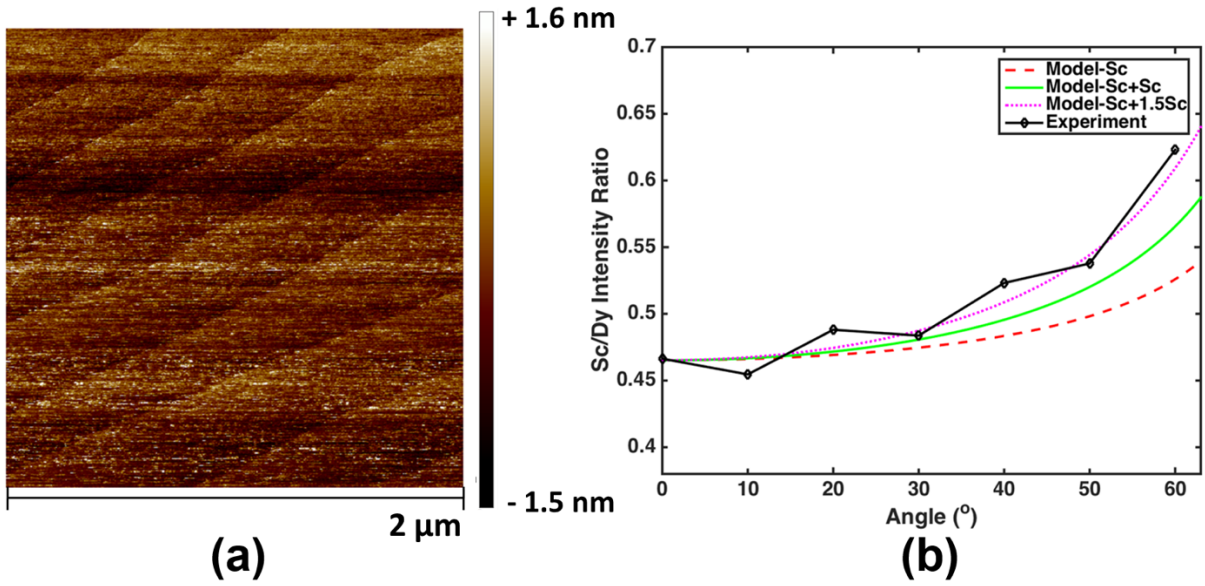

Figure 7.6. AFM image (in tapping mode) of a $2\mu m \times 2\mu m$ area in (a) of a self-supporting (3 mm diameter) TEM sample showing flat steps and terraces, and angle resolved XPS experimental data and fit in (b).

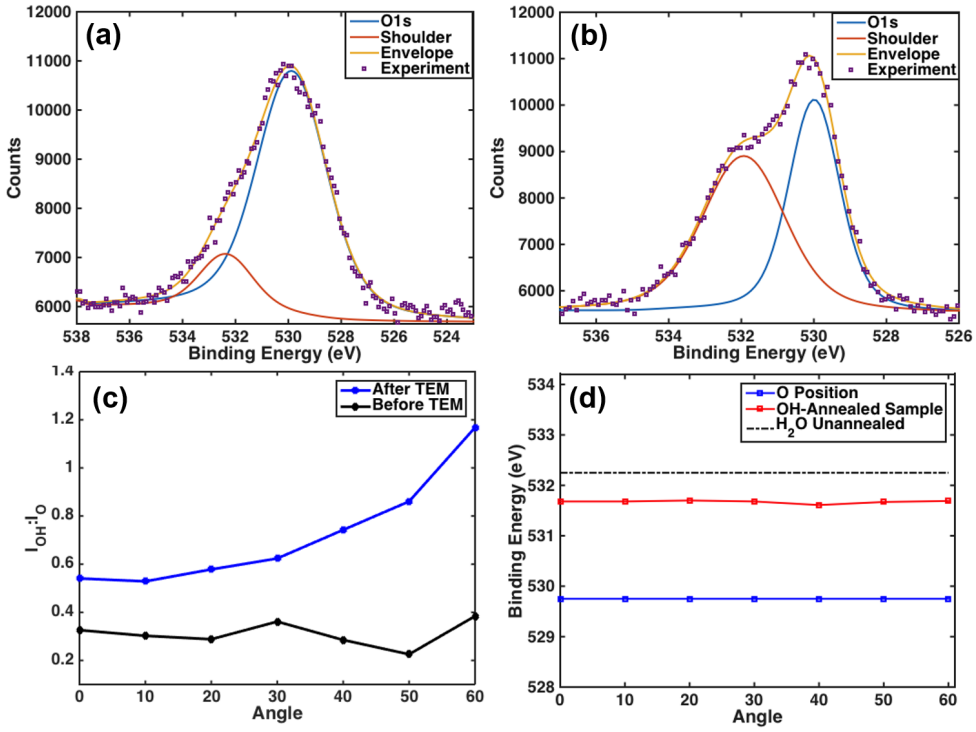

Figure 7.7. In (a), XPS spectra of the O1s peak before TEM and (b) after TEM, both collected at 60°, with angle resolved photoelectron spectroscopy of the O1s shoulder to main peak intensity for a $DyScO_3$ sample before and after TEM in (c) and the corresponding peak positions in (d). The dotted line in (d) marks the position of the shoulder for a sample with molecularly adsorbed H_2O measured only at 0° tilt. The angles are measured with respect to the surface normal.

Samples were removed from the microscope were not easy to extract from the copper cup on the holder. Instead the samples were attracted back into the cup when pushed with tweezers. This is consistent with charge retention in air after removal from the microscope. The amount of charge retained in the sample can be approximated by a force balance between the weight of the sample and the electrostatic attraction between the sample and the holder. Using such an approximation, we calculated the charge to be about 10^{-4} e/nm^2. XPS analysis of the sample after use in the electron microscope (Figure

7.7) and held in air for about 1h showed substantial adsorbed hydroxide, consistent with charge neutralization by adsorption of water.

7.5.3. Density Functional Theory Calculations

Using the surface composition obtained from angle resolved XPS, DFT calculations were carried out for different possibilities. These calculations indicated that the lowest energy structure contained three rows along [001] as shown in Figure 7.8.

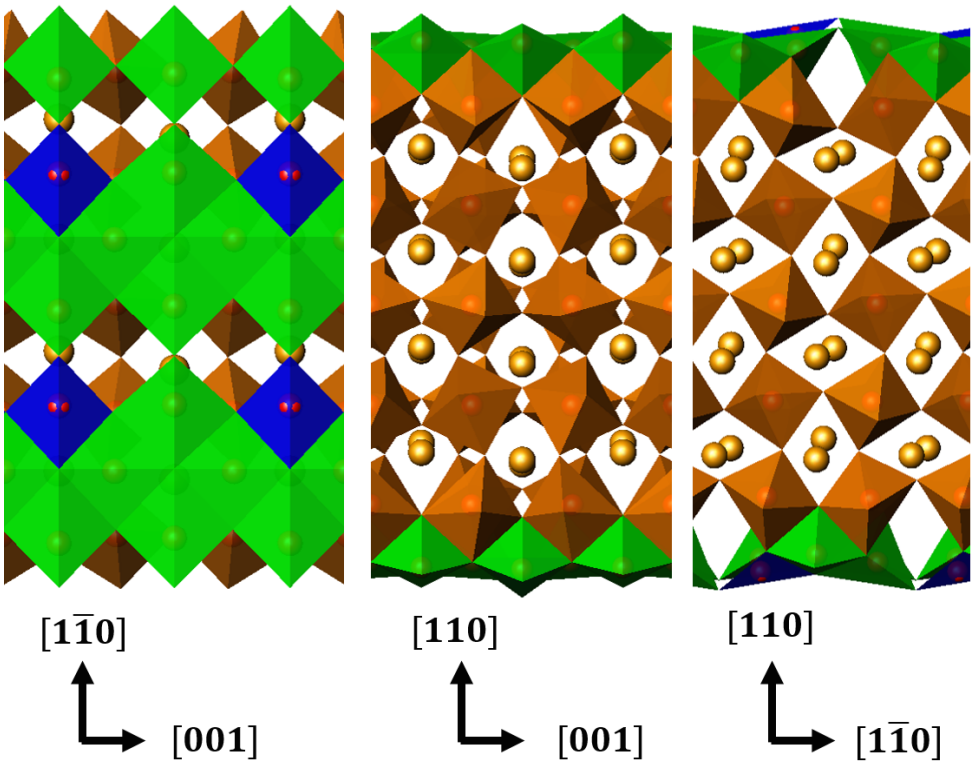

Figure 7.8. DFT relaxed structure of $DyScO_3$ with 2.5 surface ScO_2 layer from three different orientations. ScO_4 tetrahedra are in blue, ScO_5 octahedra with an unoccupied oxygen site are in green and ScO_6 octahedra are in brown.

7.5.4. Ex-Situ Measurement of Flexoelectric Coefficient

Flexoelectric coefficient measurements were performed using a three-point bending configuration similar to the one described in Zubko et al. [222] by a fellow graduate student Christopher Mizzi.

Table 7.1. Measured flexoelectric coefficient over a number of different measurements across different days with variation in static force and oscillation frequency for [110] oriented $DyScO_3$ showing little variation in the values.

Flexoelectric Coefficient [nC/m]	Static Force (gm)	Frequency [Hz]
10.7	300	33
6.09	200	33
8.73	250	33
8.15	150	33
7.98	200	33
8.68	200	33
9.21	300	23
9.23	200	17
8.11	200	33
10.7	200	7
8.03	100−250	23, 33
5.57	100−200	33
7.49	150	33

Commercially available single crystalline substrates (MTI Corp, Richmond, CA) were cut into samples with typical dimensions of 10×10×0.5 mm and 10×5×0.5 mm^3. Approximately 50 nm Au electrodes were deposited using a sputter coater. Ag paste was used to attach Cu wires to the Au electrodes. Samples were annealed at 300°C for approximately 2 hours to improve mechanical stability and electrical conductivity. Measurements were made with and without scraping wire to expose Cu from oxidized Cu. This had minimal impact on measurements.

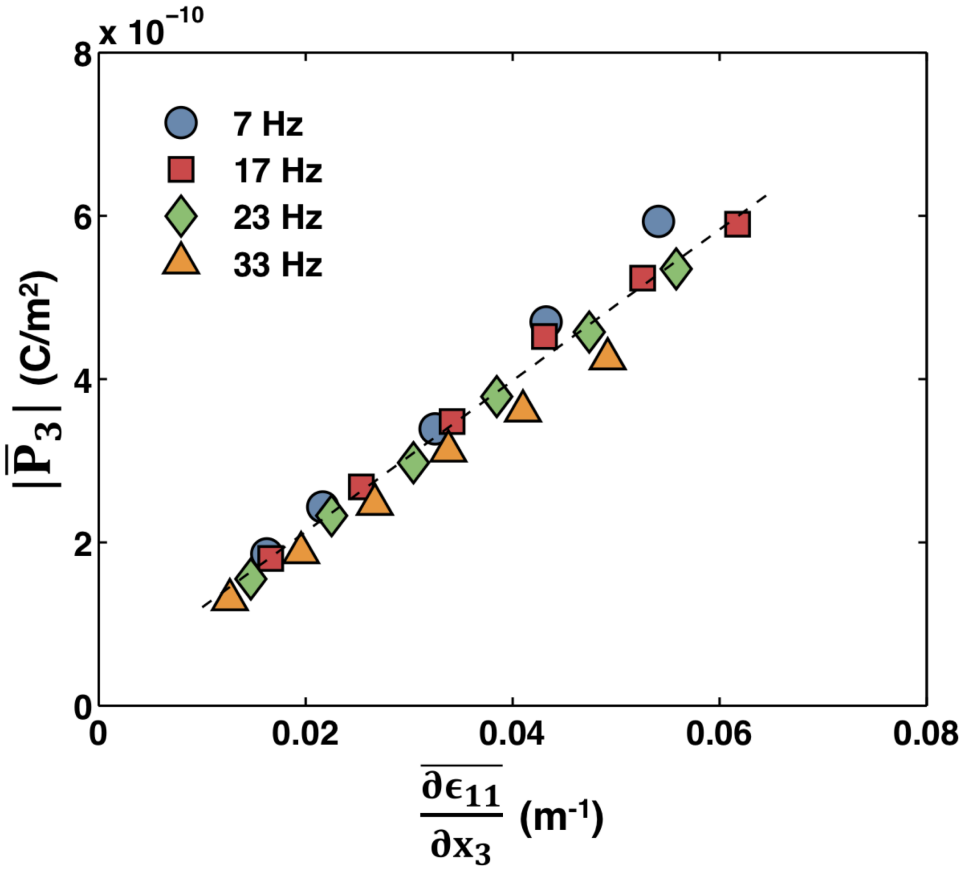

Figure 7.9. Polarization versus strain gradient for a series of measurements performed at different oscillatory frequencies for [110] oriented $DyScO_3$. The dotted line indicates a linear fit between strain gradient and polarization. The slope of such a line is the flexoelectric coefficient.

A dynamic mechanical analyzer (DMA) was used to bend the sample at a specified frequency. A variety of static forces and frequencies were used (typically in the 10−40 Hz range). Static forces were chosen to be small enough to avoid any piezoelectric contributions. The sample sat on two alumina rods spaced 8.4125 mm apart which were held in a custom machined sample holder. A lock-in amplifier was used to measure the current that was generated due to the flexoelectric effect. Displacements were calculated using

the elastic moduli [232] and force measurements from the DMA. Flexoelectric coefficient as a function of different static forces and oscillation frequencies for [110] oriented $DyScO_3$ given in Table 7.1 and Figure 7.9. The flexoelectric coefficient was measured to be about 8 nC/m which corresponds to a flexocoupliing voltage of 42 V. The flexocoupling voltage is the ratio of the flexoelectric coefficient and the dielectric constant of the material. It is therefore a normalized measure of flexoelectric response in materials that can be compared across materials with a wide range of dielectric constant. This clearly shows that the flexoelectric coefficient is independent of both of static force and oscillation frequency in our measurement regime.

These measurements establish that flexoelectric effect in lanthanide scandates are significant and support the observations inside TEM. The observations made with TEM however are of the converse flexoelectric effect as the samples bend due to the presence of polarization resulting from the charging of samples.

7.6. Charging and Bending in Lanthanide Scandates

To understand the cause of high charge accumulation in lanthanide scandates, we probed the electronic structure with UPS and REELS. UPS results (Figure 7.10) indicated that the material had a work function of 5.8 eV ($\pm$ 0.1). REELS experiments (Figure 7.10) showed no energy loss events below 5.7 eV ($\pm$ 0.1), which is our experimental measurement of the band gap. DFT calculations indicated values of 5.4 eV and 5.8 eV for the band gap and work function, respectively. These results explain the severe charging;

secondary electron produced by inelastic scattering in the bulk have sufficient energy to escape, and almost no bulk traps to fall into.

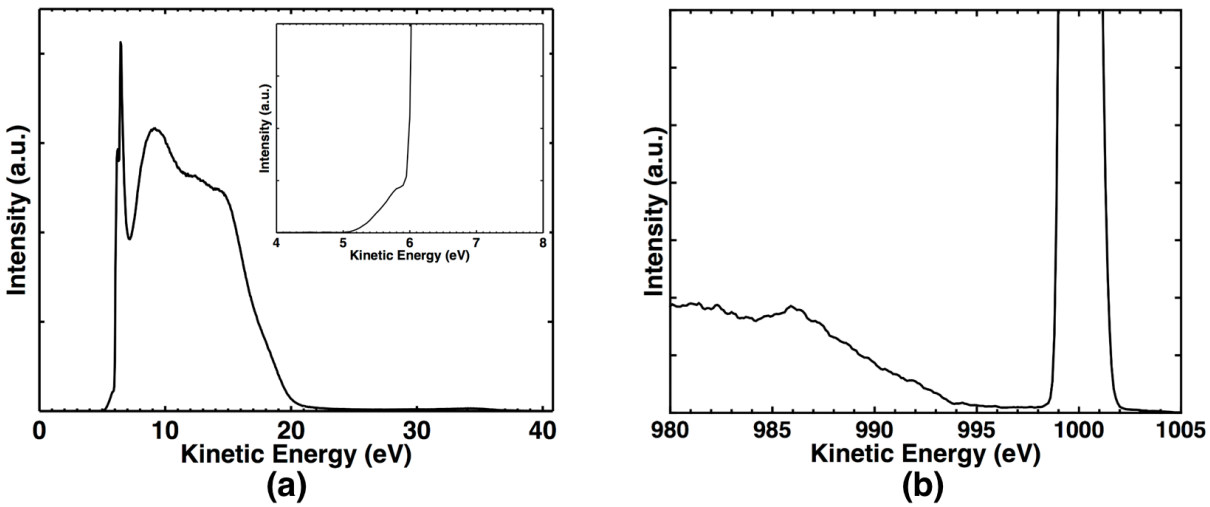

Figure 7.10. (a) UPS of the well annealed (2.5 surface Sc layer) sample along with an embedded sub-panel showing the fine details of the edge. (b) REELS with an incident energy of 1 keV showing no energy loss events up to the vacuum level. The dotted lines in green and red are the linear extrapolations of the experimental data. The small peak in (a) around 6eV has in integrated intensity about a thousand time smaller than that of the main UPS peak.

For completeness, ion milled samples and samples coated with a thin layer of carbon showed minimal charging and bending. Therefore, charging and bending are linked in our observations inside the microscope.

A number of studies [233–237] have measured charge on materials using electron holography. A recent study on MgO smoke particles [238] measured surface charge density to be about 1.751×10^{-3} electrons/nm^2 using electron holography. The amount of charge

accumulated on a material can be used to calculate the bending due to flexoelectric effect (see equation 7.9).

$$\zeta = f\frac{12\sigma(1-\nu^2)}{Gd^2} \tag{7.9}$$

where, ζ is the curvature, f is the flexocoupling voltage, G is the Young's modulus, σ is the surface charge density, d is the film thickness and ν is the Poisson's ratio.

Assuming an identical field as would be produced by the amount of surface charge density measured for MgO smoke particles along with the experimentally measured value of the flexocoupling voltage f = 42 Volts [239], yields a curvature of about 1.4×10^3 m^{-1}, which is one order of magnitude smaller than the measured value of 3×10^4 m^{-1} for $DyScO_3$. The curvature along both the length and the width of the rod are comparable. Experimentally the amount of charging in $DyScO_3$ is substantially larger than for comparable well annealed MgO single crystals [240]. The charging is so severe that the lanthanide scandate samples retained charge even when removed from the microscope (Movie M5 [230]). Inverting equation 7.9, the surface charge density on the sample was calculated to be 0.03 electrons/nm^2. We believe this is not an unreasonable estimate given the severity of charging in these materials.

For completeness, temperature dependent in-situ bending experiments were also carried out. The beam was first focused on to a thin rod of $DyScO_3$ causing the rod to

bend. Subsequently, the sample was heated inside the microscope. The amount of bending observed gradually reduced with increasing temperature, also indicating a reduction in charging and polarization across the sample (see Figure 7.11).

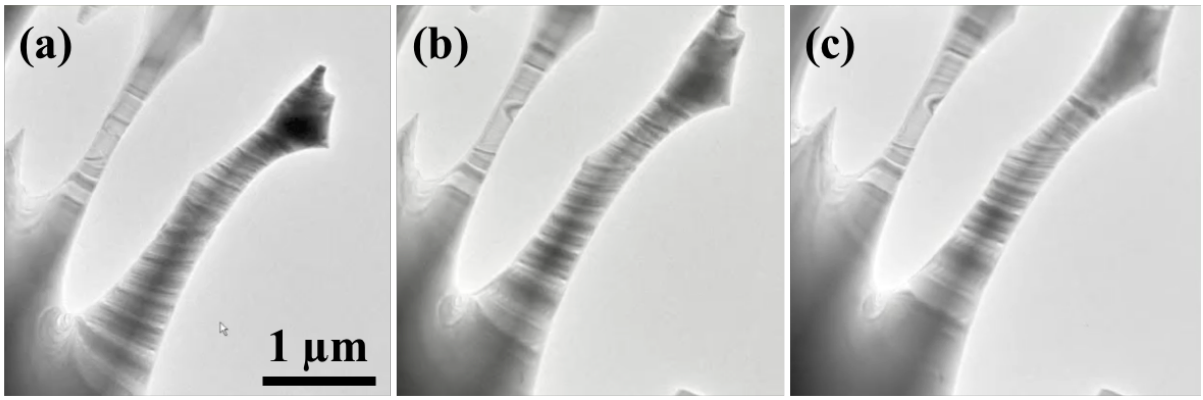

Figure 7.11. TEM images of a rod of $DyScO_3$ bending under the electron beam. The sequence of frames from (a) through (c) show reduction in bending with increasing temperature. Frames (a)−(c) were taken at temperatures of 185°C, 215°C and 250°C, respectively. The electron beam flux was held constant throughout the experiment.

7.7. Discussion

It is unclear as to what physical phenomena dominate in contributions to the observed flexoelectric effect. There are several contributions to flexoelectric effect which include the static and dynamic components of both surface and bulk. Surface piezoelectricity is also significant in thin samples [23]. Tilting of the octahedra (which is large in these scandates) may strongly couple into the different contributions. Tilts in the relevant surface structure of $DyScO_3$ with 2.5 ScO_x layer is large. Adding to this there is the issue of what role the 4f states play.

It is also not clear as to what the relative contributions of electronic and ionic polarizations are. It is usually assumed that the flexoelectric effect scales with the dielectric constant. As a result, high-K dielectric materials and ferroelectrics have been extensively studied for the presence of flexoelectric response as ionic contributions are dominant. However, this is true only in the transverse acoustic wave regime. In the longitudinal acoustic wave regime the electronic contributions are significant. In addition, the electronic contributions do not scale with the dielectric constant. These contributions could provide an answer for the large flexocoupling in lanthanide scandates and provide insight into the role of 4f electrons in these observations. Hence, the lanthanide scandates warrant further exploration.

CHAPTER 8

Work in Progress

8.1. Electronic Structure Studies of Lanthanide Scandates

8.1.1. Introduction

Lanthanide scandates, particularly $DyScO_3$, have been extensively used as substrates for thin film growth [241–245]. Although it is known that interfacial structure can lead to novel properties (e.g. the 2D electron gas at the $LaAlO_3/SrTiO_3$ interface [21]), studies using lanthanide scandates as substrates have assumed simple bulk truncation and treated the lanthanide scandates as inert substrates which only provide a lattice parameter for the growth. Recent observations of polar phonons [246], magnetic anisotropy [231], and an unexpectedly large flexoelectric response [239] in lanthanide scandates indicate a knowledge gap in the physics of these materials. Certain electronic structure details, including the position and hybridization of 4f states in the valence band, are not clear. There are other materials where it is known that the hybridization of 4f states with the O2p states can have strong implications on electronic properties [247–249]; understanding this in the lanthanide scandates is of potential technological relevance.

A few papers have looked at lanthanide scandates using XPS and conventional LDA+U DFT calculations [250, 251]. As we will see later, the interpretation of the valence band

region XPS in this literature is open to question since hybridization effects and the large scattering cross-section of the 4f states compared to oxygen or scandium have not been fully considered.

In this work, we report details of valence band electronic structure of lanthanide scandates. Both the XPS and DFT indicate that the 4f electrons are not spectators, but have comparable energies to the oxygen states at the valence band edge and are an active part of the occupied electronic states of these materials. This means that the 4f states can play an important role in the electronic properties of these materials with consequences for systems where they have been used as substrates for thin film growth of other oxides.

8.1.2. Sample Preparation

Commercially available 10×10×0.5 mm single crystalline substrates of [110] oriented $LnScO_3$ (Ln=Dy, Tb, Gd) with space group Pbnm were purchased from MTI Corp, Richmond, CA. These substrates were annealed at 1050°C for 10 hours in air to promote surface ordering and a second $DyScO_3$ substrate was left unannealed for comparison. For distinction, unannealed $DyScO_3$ is referred to hereafter as as-received. Following the 1050°C anneal, the color of $DyScO_3$ changed from yellow to brown, whereas the other lanthanide scandates did not change color. Prior to XPS measurements, all samples were baked at 600°C for 6 hours in air to minimize surface contamination and placed in a high vacuum chamber to degas overnight. No color change was observed following the 600°C bake.

8.1.3. X-ray Photoelectron Spectroscopy

Most of the XPS measurements were taken on an ESCALAB 250Xi. The details of the instrument have been discussed in Chapter 2. High resolution valence band spectra (VBS) were acquired with a pass energy of 20 eV, step size of 0.1 eV, spot size of 650 μm and averaged over 10 scans. VBS spectra for a given sample were normalized and smoothed for comparison across different temperatures.

8.1.4. Density Functional Theory Calculations

DFT calculations of the electronic structure of lanthanide scnadates were performed by Prof. Laurence Marks with the all-electron augmented plane wave + local orbitals WIEN2K code [252]. A number of approaches were tested. Conventional LDA+U correction methods are plausible for the 4f states; however, if a large enough HubbardU was used to move the unoccupied 4f states for a reasonable band-gap, this led to highly-confined, essentially atomic 4f occupied states which disagrees with the experimental data. This was true independent of whether a PBE [253], PBEsol [228] or mBJ [254] functional was used. Improved results were obtained using an on-site hybrid [227, 255] method. This calculates an exact-exchange hybrid correction within the muffin-tins, then applies it similar to a Hubbard U, but also quite different. For instance, with this hybrid correction approach the potential applied to the unoccupied states and the resulting energy change is typically much larger than that for the occupied ones. For the calculations here, muffin tin radii of 1.68, 1.82, and 2.02 were used for O, Sc and Dy, respectively, to minimize inclusion

of tails of the O2p density perturbing the calculation of the exact-exchange corrections inside the muffin tins for Sc and Dy. The plane-wave expansion parameter RKMAX was 6.5.

A subtle question with corrections such as LDA+U or an on-site hybrid is the Hubbard U value or the fraction of on-site hybrid to use. It is now well established that the hybrid fraction is not a universal factor, but should vary [227, 256]. To determine what values to use, the atomic positions and bulk optimized lattice constants were calculated using the on-site hybrid method with the PBESol functional and the hybrid fraction was varied to minimize the forces on the atoms when in the known bulk positions [173]. This led to on-site corrections of 0.800 for the Sc3d and 0.500 and 0.325 for the Dy5d and Dy4f states, respectively. We note that a larger Dy4f on-site correction value when spin-orbit coupling was included led to a change in the spin-state which would disagree with the known magnetic moment for Dy in $DyScO_3$ [251]. This provided an upper bound for the Dy4f on-site correction value. The electron density and all atomic positions were simultaneously converged using a quasi-Newton algorithm [257]; the numerical convergence was better than 0.01 eV per 1×1 surface cell. All calculations were performed with a ferromagnetic ordering; the energy difference between ferromagnetic and anti-ferromagnetic orderings was minimal, as would be expected since this is a weak energy term in lanthanide scandates.

8.1.5. Results

8.1.5.1. Valence band electronic structure of lanthanide scandates. Valence band XPS of three lanthanide scandates acquired using Al K-alpha is given in Figure 8.1. The spectra have been aligned with respect to the Sc3p peak at 30.8 eV. The peaks in the $20 - 25$ eV range are from a combination of O2s and Dy5p states. The major differences between the three spectra in Figure 8.1 is found in the $0 - 10$ eV range. As mentioned earlier, many papers put the rare earth Dy4f, O2p and Sc3d states in this region [251, 258] with little to no hybridization between the Dy4f and O2p states. The extent of hybridization and position of these states is however open to question.

We therefore turn to understanding the details of the VBS in the $0 - 10$ eV range. Partial density of states (PDOS) of the valence band region obtained from DFT calculations (Figure 8.2) show major contributions from Dy4f, O2p states and a small density of Sc3d states. These results also indicate that the 4f states are at the valence band edge are strongly hybridized with the O2p states in both $TbScO_3$ and $DyScO_3$. In the case of $GdScO_3$, the overlap between Gd4f states and O2p states is significantly less. This is qualitatively consistent with the Gd4f states being half filled.

8.1.6. Work in Progress

(1) **XPS Simulations**: A majority of XPS simulations reported in literature have scaled the PDOS by the corresponding scattering cross sections for comparison with experimental XPS data [251, 259, 260]. For proper energy scaling and

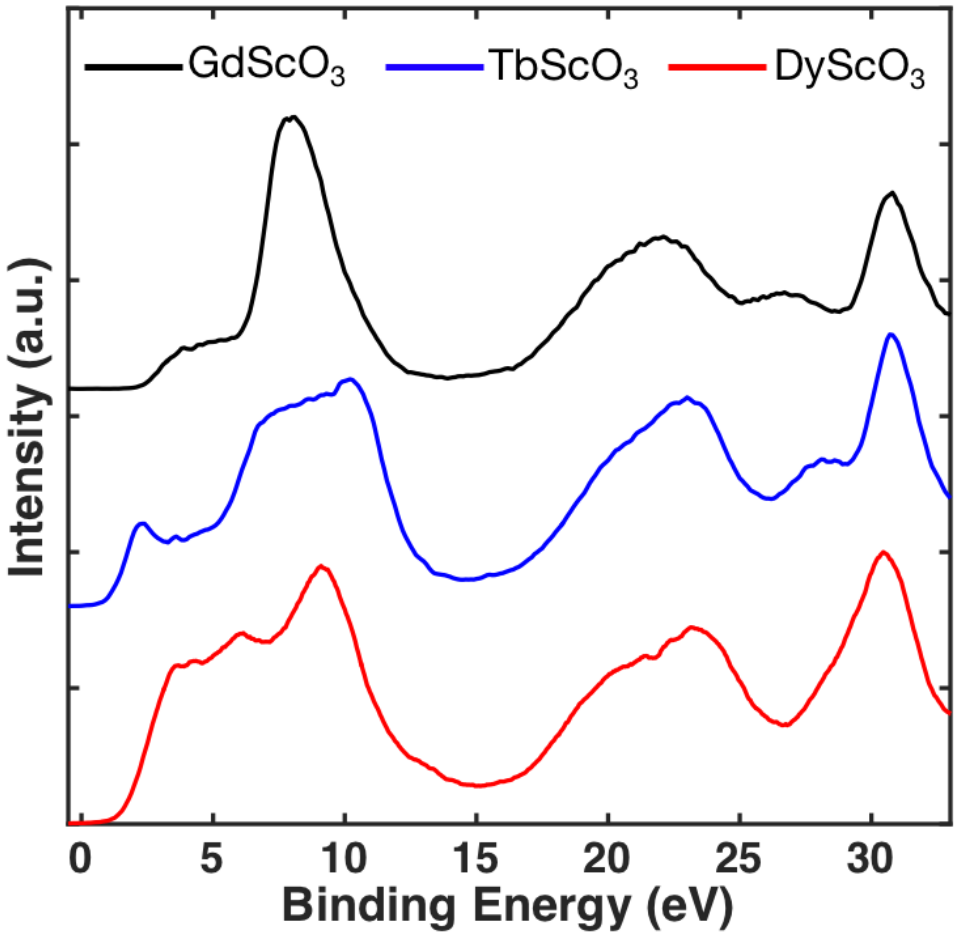

Figure 8.1. Valence band X-ray photoelectron spectra of $ReScO_3$ (Re = Gd, Tb, Dy) acquired using Al K-alpha.

width of XPS peaks, final state effects and hybridization in the valence band region should be accounted for. More accurate DFT calculations are currently being pursued.

(2) **Temperature dependent XPS**: VBS of the lanthanide scandates show significant changes with temperature (see Figure 8.3) in both peak structure and the

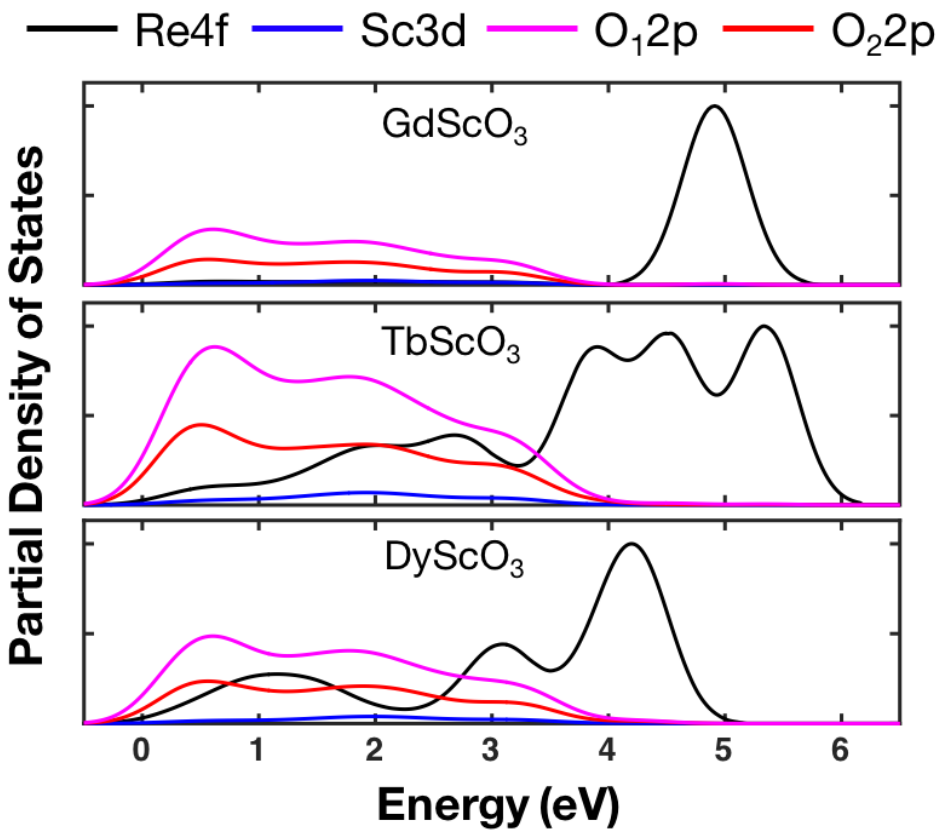

Figure 8.2. Valence band partial density of states of $ReScO_3$ (Re = Gd, Tb, Dy). (O_1 and O_2 given in the legend are the two inequivalent O in the unit cell.)

amount of charging under X-ray illumination. The mechanism of these changes are currently being explored.

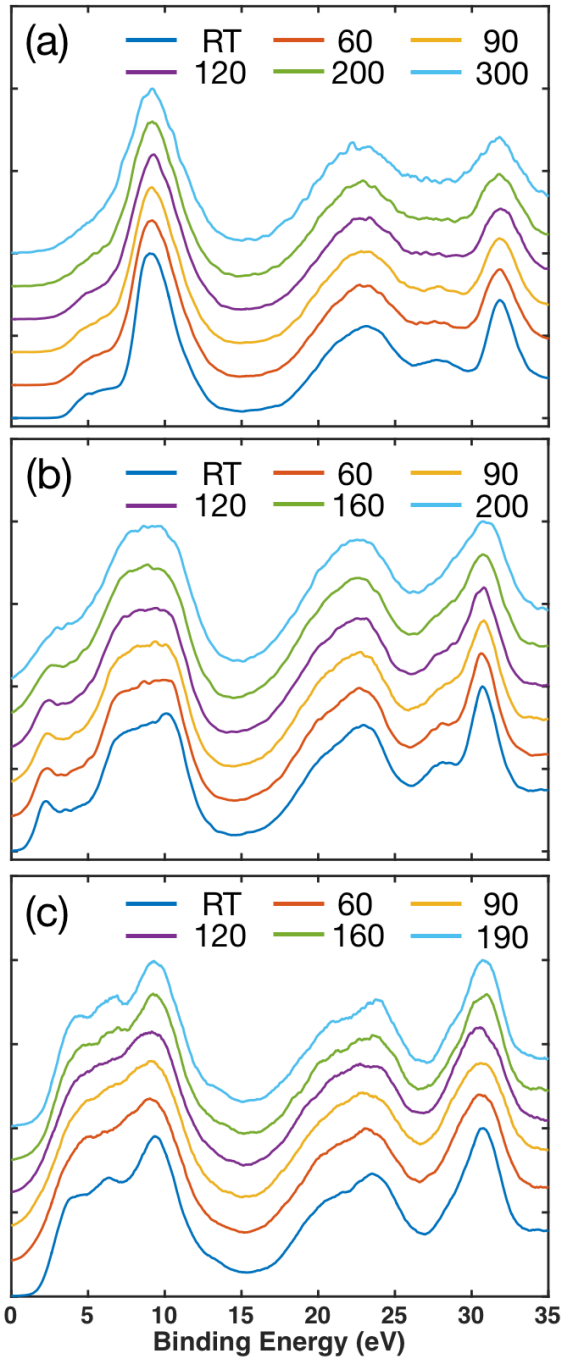

Figure 8.3. Temperature dependent valence band XPS of (a) $GdScO_3$, (b) $TbScO_3$, and (c) $DyScO_3$. Temperature is given in degrees Celsius.

8.2. Surface of Lanthanum Aluminate

Lanthanum aluminate has been extensively used as a substrate for growth [261–264]. Its interface with $SrTiO_3$ [21, 265–267] has received significant attention due to the occurrence of a 2D electron gas. Therefore, it is imperative to understand the surface of $LaAlO_3$ for growth and electronic applications. Two reconstructions, $(\sqrt{5} \times \sqrt{5})$R26.6° [12] on the (001) surface and (3×1) on the (110) surface, have been solved. A (2×1) surface reconstruction has been observed on $LaAlO_3$ (110) and is currently being studied for detailed atomic structure.

8.2.1. Sample Preparation

TEM samples of (110) oriented $LaAlO_3$ were prepared using the conventional technique described in Chapter 2 and annealed in flowing oxygen for 8 hours at 1100°C.

8.2.2. Results

BF TEM image of an ion milled sample showed bend contours and strain (see Figure 8.4). The amorphous ring seen in diffraction pattern in Figure 8.4 is indicative of surface disorder. The sample after annealing showed discrete thickness fringes owing to a flat and ordered surface (see Figure 8.5). The damage from ion beam bombardment was also significantly reduced. The corresponding TED pattern (see Figure 8.5) showed ordered spots corresponding to a (2×1) surface reconstruction.

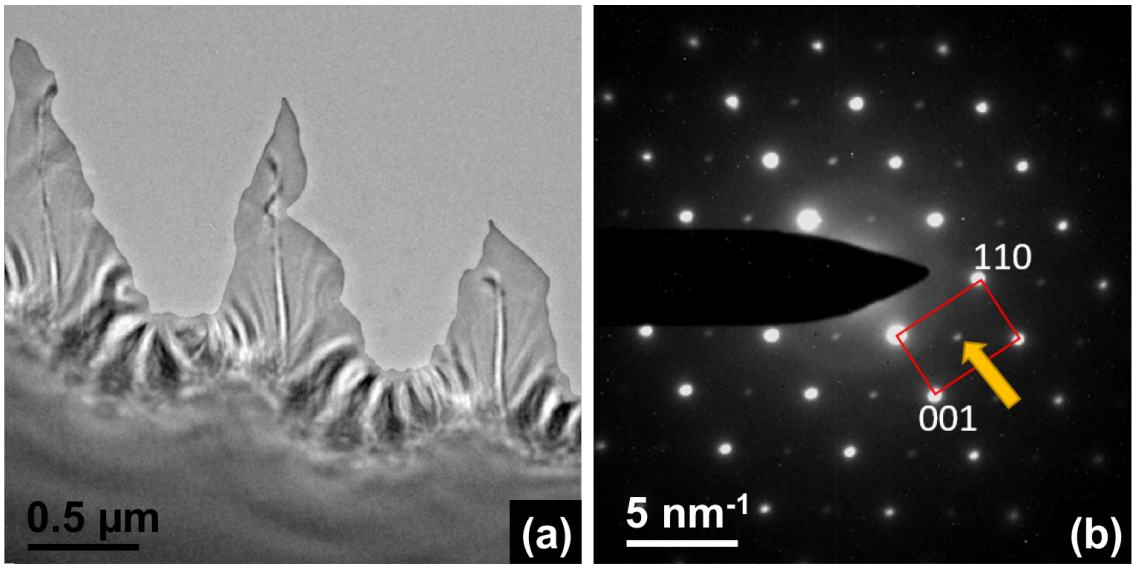

Figure 8.4. In (a) bright field TEM image and (b) TED of a sample of $LaAlO_3$ (110) after ion beam milling. (The pseudocubic bulk lattice has been outlined in red and the spot corresponding to distortions in the rhombohedral lattice has been indicated with an arrow.)

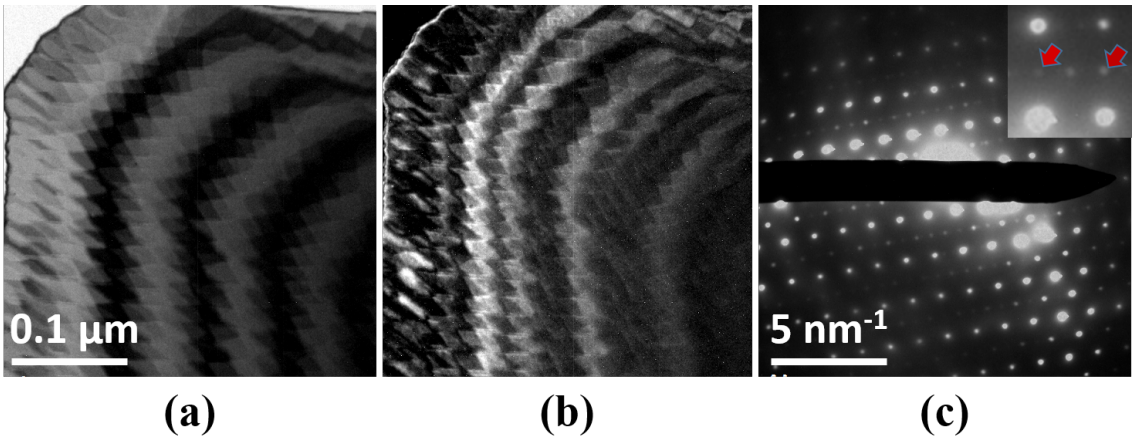

Figure 8.5. In (a) bright field and (b) darkfield TEM images of a sample of $LaAlO_3$ (110) after annealing. The corresponding diffraction pattern in (c) shows a (2×1) surface periodicity. The surface spots are marked with red arrows in the zoomed inset.

Angle resolved XPS was performed and fitted with a layer model [25] outlined in Chapter 2. The signal was integrated over a thickness equivalent to five times the inelastic mean free path. The experimental data is consistent with one Al per surface (1×1). The intensity ratio of O1s shoulder to main peak ratio does not increase with grazing angle indicating a dry surface.

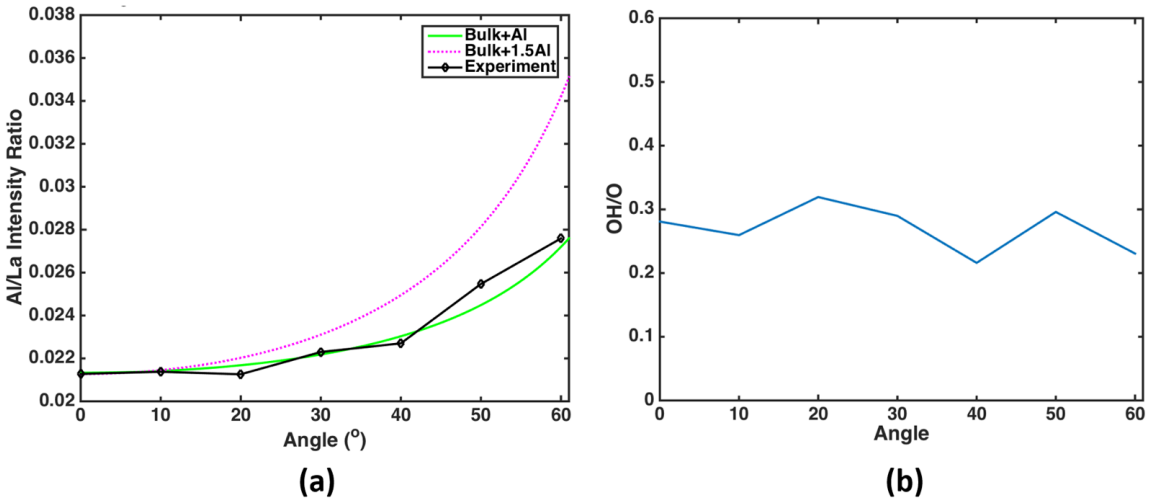

Figure 8.6. Angle resolved XPS data in (a) experimental surface composition and fit with a layer model and in (b) O1s shoulder to main peak ratio as a function of angle.

The stacking sequence in the [110] direction is LaAlO/2O/LaAlO/2O with +4/-4 alternation of the valence. For a (2×1) surface reconstruction, 2 Al atoms and 5 oxygen atoms satisfy valence neutrality. With constraints on the surface termination and composition, several possible structures are being relaxed using DFT calculations.

References

[1]C. N. R. Rao, "Transition metal oxides", Annual Review of Physical Chemistry **40**, 291–326 (1989).

[2]M. Kargarian and G. A. Fiete, "Topological crystalline insulators in transition metal oxides", Phys. Rev. Lett. **110**, 156403 (2013).

[3]D. G. Schlom, L.-Q. Chen, C.-B. Eom, K. M. Rabe, S. K. Streiffer, and J.-M. Triscone, "Strain tuning of ferroelectric thin films", Annual Review of Materials Research, Annual Review of Materials Research **37**, 589–626 (2007).

[4]V. M. Goldschmidt, "Die gesetze der krystallochemie", Naturwissenschaften **14**, 477–485 (1926).

[5]H. D. Megaw, "Origin of ferroelectricity in barium titanate and other perovskite-type crystals", Acta Crystallographica **5**, 739–749 (1952).

[6]G. Shirane, J. D. Axe, J. Harada, and J. P. Remeika, "Soft ferroelectric modes in lead titanate", Phys. Rev. B **2**, 155–159 (1970).

[7]D. M. Kienzle, A. E. Becerra-Toledo, and L. D. Marks, "Vacant-Site Octahedral Tilings on $SrTiO_3$ (001), the $(\sqrt{13} \times \sqrt{13})$R33.7 Surface, and Related Structures", Physical Review Letters **106**, 176102 (2011).

[8]J. Ciston, H. G. Brown, a. J. D'Alfonso, P. Koirala, C. Ophus, Y. Lin, Y. Suzuki, H. Inada, Y. Zhu, L. J. Allen, and L. D. Marks, "Surface determination through atomically resolved secondary-electron imaging", Nature Communications **6**, 7358 (2015).

[9]L. D. Marks, a. N. Chiaramonti, S. U. Rahman, and M. R. Castell, "Transition from Order to Configurational Disorder for Surface Reconstructions on $SrTiO_3$ (111)", Physical Review Letters **114**, 1–6 (2015).

[10]N. Erdman, K. R. Poeppelmeier, M. Asta, O. Warschkow, D. E. Ellis, and L. D. Marks, "The structure and chemistry of the TiO_2-rich surface of $SrTiO_3$ (001).", Nature **419**, 55–58 (2002).

[11]N. Erdman, O. Warschkow, M. Asta, K. R. Poeppelmeier, D. E. Ellis, and L. D. Marks, "Surface Structures of $SrTiO_3$ (001): A TiO_2-rich Reconstruction with a c(4×2) Unit Cell", Journal of the American Chemical Society **125**, 10050–10056 (2003).

[12]C. Lanier, A. van de Walle, N. Erdman, E. Landree, O. Warschkow, A. Kazimirov, K. Poeppelmeier, J. Zegenhagen, M. Asta, and L. Marks, "Atomic-scale structure of the $SrTiO_3$(001)-c(6x2) reconstruction: Experiments and first-principles calculations", Physical Review B **76**, 45421 (2007).

[13]J. A. Enterkin, A. K. Subramanian, B. C. Russell, M. R. Castell, K. R. Poeppelmeier, and L. D. Marks, "A homologous series of structures on the surface of $SrTiO_3$ (110)", Nature Materials **9**, 245–248 (2010).

[14]J. Ciston, "Crystallographic perturbations to valence charge density and hydrogen-surface interactions", Doctor of Philosophy (Northwestern University, Evanston, IL, 2009).

[15]P. Gao, H.-J. Liu, Y.-L. Huang, Y.-H. Chu, R. Ishikawa, B. Feng, Y. Jiang, N. Shibata, E.-G. Wang, and Y. Ikuhara, "Atomic mechanism of polarization-controlled surface reconstruction in ferroelectric thin films", Nature Communications **7**, 11318 (2016).

[16]A. Puzder, A. J. Williamson, F. A. Reboredo, and G. Galli, "Structural stability and optical properties of nanomaterials with reconstructed surfaces", Phys. Rev. Lett. **91**, 157405 (2003).

[17]D. Kan, T. Terashima, R. Kanda, A. Masuno, K. Tanaka, S. Chu, H. Kan, A. Ishizumi, Y. Kanemitsu, Y. Shimakawa, and M. Takano, "Blue-light emission at room temperature from Ar^+ irradiated $SrTiO_3$", Nature Materials **4**, 816–819 (2005).

[18]G. A. Somorjai, "Surface reconstruction and catalysis", Annual Review of Physical Chemistry **45**, 721–751 (1994).

[19]A. Baratoff and G. Binnig, "Mechanism of superconductivity in $SrTiO_3$", Physica B+C **108**, 1335–1336 (1981).

[20]J. A. Enterkin, W. Setthapun, J. W. Elam, S. T. Christensen, F. A. Rabuffetti, L. D. Marks, P. C. Stair, K. R. Poeppelmeier, and C. L. Marshall, "Propane Oxidation over $Pt/SrTiO_3$ Nanocuboids", ACS Catalysis **1**, 629–635 (2011).

[21]A. Ohtomo and H. Y. Hwang, "A high-mobility electron gas at the $LaAlO_3/SrTiO_3$ heterointerface.", Nature **427**, 423–426 (2004).

[22]Z. Q. Liu, C. J. Li, W. M. Lu, X. H. Huang, Z. Huang, S. W. Zeng, X. P. Qiu, L. S. Huang, A. Annadi, J. S. Chen, J. M. D. Coey, T. Venkatesan, and Ariando, "Origin of the Two-Dimensional Electron Gas at $LaAlO_3/SrTiO_3$ Interfaces: The Role of Oxygen Vacancies and Electronic Reconstruction", Phys. Rev. X **3**, 021010 (2013).

[23]P. Zubko, G. Catalan, and A. K. Tagantsev, "Flexoelectric Effect in Solids", Annual Reviews **43**, 387–421 (2013).

[24]M. Kawasaki, A. Ohtomo, T. Arakane, K. Takahashi, M. Yoshimoto, and H. Koinuma, "Atomic control of $SrTiO_3$ surface for perfect epitaxy of perovskite oxides", Applied Surface Science **107**, 102–106 (1996).

[25]E. McCafferty and J. Wightman, "An x-ray photoelectron spectroscopy sputter profile study of the native air-formed oxide film on titanium", Applied Surface Science **143**, 92–100 (1999).

[26]W. Cochran, "Relations between the Phases of Structure Factors", Acta Crystallographica **8**, 473–478 (1955).

[27]C. J. Gilmore, L. D. Marks, D. Grozea, C. Collazo, E. Landree, and R. D. Twesten, "Direct Solutions of the Si (111) 7×7 Structure", Surface Science **381**, 77–91 (1997).

[28]C. Gilmore, W. Dong, and G. Bricogne, "A Multisolution Method of Phase Determination by combined Maximization of Entropy and Likelihood. VI. The Use of Error-Correcting Codes as a Source of Phase Permutation and their Application to the Phase Problem in Powder, Electron and Macromolecular Crystallography", Acta Crystallographica **A55**, 70–83 (1999).

[29]D. Harker and J. S. Kasper, "Phases of Fourier Coefficients Directly from Crystal Diffraction Data", Acta Crystallographica **1**, 70–75 (1948).

[30]J. Karle and H. Hauptman, "A Theory of Phase Determination for the Four Types of Non-Centrosymmetric Space Groups $1P222$, $2P22$, $3P_12$, $3P_22$", Acta Crystallographica **9**, 635–651 (1956).

[31]E. Landree, C. Collazo-Davila, and L. D. Marks, "Multi-Solution Genetic Algorithm Approach to Surface Structure Determination Using Direct Methods", Acta Crystallographica **B53**, 916–922 (1997).

[32]L. D. Marks, E. Bengu, D. Grozea, E. Landree, C. Leslie, and W. Sinkler, "Direct Methods for Surfaces", Surface Review and Letters **5**, 1087–1106 (1998).

[33]L. D. Marks and E. Landree, "A Minimum-Entropy Algorithm for Surface Phasing Problems", Acta Crystallographica **A54**, 296–305 (1998).

[34]L. D. Marks, "General Solution for Three-dimensional Surface Structures Using Direct Methods", Physical Review B **60**, 2771–2780 (1999).

[35]L. D. Marks, N. Erdman, and A. K. Subramanian, "Crystallographic Direct Methods for Surfaces", Journal of Physics: Condensed Matter **13**, 10677–10688 (2001).

[36]D. Sayre, "The Squaring Method: A New Method for Phase Determination", Acta Crystallographica **5**, 60–65 (1952).

[37]W. Sinkler, E. Bengu, and L. D. Marks, "Application of Direct Methods to Dynamical Electron Diffraction Data for Solving Bulk Crystal Structures", Acta Crystallographica **A54**, 591–605 (1998).

[38]Y. Tanishiro and K. Takayanagi, "Validity of the Kinematical Approximation in Transmission Electron Diffraction for the Analysis of Surface Structures", Ultramicroscopy **27**, 1–8 (1989).

[39]M. M. Woolfson, "Direct Methods - from Birth to Maturity", Acta Crystallographica **A43**, 593–612 (1987).

[40]P. Xu, G. Jayaram, and L. D. Marks, "Cross-Correlation Method for Intensity Measurement of Transmission Electron Diffraction Patterns", Ultramicroscopy **53**, 15–18 (1994).

[41]P. Xu and L. D. Marks, "Intensities of Surface Diffraction Spots in Plan View", Ultramicroscopy **45**, 155–157 (1992).

[42]R. Kilaas, L. D. Marks, and C. Own, "EDM 1.0: Electron Direct Methods", Ultramicroscopy **102**, 233–237 (2005).

[43]A. Howie and M. J. Whelan, Proceedings of the Royal Society A, London **263**, 217–237 (1961).

[44]L. M. Peng, S. L. Dudarev, and M. J. Whelan, *High-Energy Electron Diffraction and Microscopy* (Oxford Science Publications, Oxford, UK, 2003).

[45]J. M. Cowley and A. F. Moodie, Acta Crystallographica **10**, 609 (1957).

[46]K. Ishizuka and N. Uyeda, "A New Theoretical and Practical Approach to the Multislice Method", Acta Crystallographica **A**, 33 (1977).

[47]J. P. Perdew and W. Yue, "Accurate and simple density functional for the electronic exchange energy: generalized gradient approximation", Phys. Rev. B **33**, 8800–8802 (1986).

[48]J. P. Perdew, K. Burke, and Y. Wang, "Generalized gradient approximation for the exchange-correlation hole of a many-electron system", Physical Review B **54**, 16533–16539 (1996).

[49]P. Blaha, K. Schwarz, G. Madsen, and J. Luitz, *WIEN2k: An Augmented Plane Wave plus Local Orbitals Program for Calculating Crystal Properties*, 2016.

[50]W. J. Burke and R. J. Pressley, "Stress Induced Ferroelectricity in $SrTiO_3$", Solid State Communications **9**, 191–195 (1971).

[51]H. Uwe and T. Sakudo, "Stress-Induced Ferroelectricity and Soft Phonon Modes in $SrTiO_3$", Physical Review B **13**, 271–286 (1976).

[52]N. A. Pertsev, A. K. Tagantsev, and N. Setter, "Phase Transitions and Strain-Induced Ferroelectricity in $SrTiO_3$ Epitaxial Thin Films", Physical Review B **61**, R825–R829 (2000).

[53]J. G. Bednorz and K. A. Muller, "$Sr_{1-x}Ca_xTiO_x$: An XY Quantum Ferroelectric with Transition to Randomness", Physical Review Letters **52**, 2289–2292 (1984).

[54]K. Szot, W. Speier, G. Bihlmayer, and R. Waser, "Switching the electrical resistance of individual dislocations in single-crystalline $SrTiO_3$", Nature Materials **5**, 312–20 (2006).

[55]A. Chen, Z. Yu, J. Scott, A. Loidl, R. Guo, A. S. Bhalla, and L. E. Cross, "Dielectric Polarization Processes in Bi:$SrTiO_3$", Journal of Physics and Chemistry of Solids **61**, 191–196 (2000).

[56]I. Pallecchi, F. Telesio, D. Marre, D. Li, S. Gariglio, J.-M. Triscone, and A. Filippetti, "Large phonon-drag enhancement induced by narrow quantum confinement at the $laalo_3$/$srtio_3$ interface", Phys. Rev. B **93**, 195309 (2016).

[57]J. H. Haeni, P. Irvin, W. Chang, R. Uecker, P. Reiche, and Y. L. Li, "Room-Temperature Ferroelectricity in Strained $SrTiO_3$", Nature **430**, 758–761 (2004).

[58]S. N. Klimin, J. Tempere, J. T. Devreese, and D. van der Marel, "Interface Superconductivity in $LaAlO_3$-$SrTiO_3$ Heterostructures", Physical Review B **89**, 184514 (2014).

[59]M. Jourdan, N. Blumer, and H. Adrian, "Superconductivity of $SrTiO_{3-\delta}$", The European Physical Journal B **33**, 25–30 (2003).

[60]M. R. Castell, "Nanostructures on the $SrTiO_3$ (001) surface studied by STM", Surface Science **516**, 33–42 (2002).

[61]K. Johnston, M. Castell, A. Paxton, and M. Finnis, "$SrTiO_3$(001)(2×1) reconstructions: First-principles calculations of surface energy and atomic structure compared with scanning tunneling microscopy images", Physical Review B **70**, 085415 (2004).

[62]S.-h. Phark, Y. J. Chang, and T. Won Noh, "Selective growth of perovskite oxides on $SrTiO_3$ (001) by control of surface reconstructions", Applied Physics Letters **98**, 161908 (2011).

[63]R. Shimizu, K. Iwaya, T. Ohsawa, S. Shiraki, T. Hasegawa, T. Hashizume, and T. Hitosugi, "Effect of oxygen deficiency on $SrTiO_3$(001) surface reconstructions", Applied Physics Letters **100**, 263106 (2012).

[64]O. Warschkow, M. Asta, N. Erdman, K. R. Poeppelmeier, D. E. Ellis, and L. D. Marks, "TiO_2-rich reconstructions of $SrTiO_3$(001): a theoretical study of structural patterns", Surface Science **573**, 446–456 (2004).

[65]J. E. T. Andersen and P. J. Moller, "Impurity-induced 900°C (2×2) surface reconstruction of $SrTiO_3$ (100)", Applied Physics Letters **56**, 1847 (1990).

[66]S. Gerhold, Z. Wang, M. Schmid, and U. Diebold, "Stoichiometry-driven switching between surface reconstructions on $SrTiO_3$(001)", Surface Science **621**, L1–L4 (2014).

[67]T. Kubo and H. Nozoye, "Surface structure of $SrTiO_3$(100)", Surface Science **542**, 177–191 (2003).

[68]Y. Lin, A. E. Becerra-Toledo, F. Silly, K. R. Poeppelmeier, M. R. Castell, and L. D. Marks, "The (2×2) reconstructions on the $SrTiO_3$ (001) surface: A combined scanning tunneling microscopy and density functional theory study", Surface Science **605**, L51–L55 (2011).

[69]T. Nishimura, A. Ikeda, H. Namba, T. Morishita, and Y. Kido, "Structure change of TiO_2 -terminated $SrTiO_3$ (001) surfaces by annealing in O_2 atmosphere and ultrahigh vacuum", Surface Science **421**, 273–278 (1999).

[70]T. Ohsawa, K. Iwaya, R. Shimizu, T. Hashizume, and T. Hitosugi, "Thickness-dependent local surface electronic structures of homoepitaxial $SrTiO_3$ thin films", Journal of Applied Physics **108**, 073710 (2010).

[71]F. Silly, D. T. Newell, and M. R. Castell, "$SrTiO_3$ (001) reconstructions: the (2×2) to c(4×4) transition", Surface Science **600**, L219–L223 (2006).

[72]M. S. Gonzalez, M. H. Aguirre, E. Mora, and M. C. Asensio, "In situ reduction of (100) $SrTiO_3$", Solid State Sciences **2**, 519–524 (2000).

[73]T. Kubo and H. Nozoye, "Surface Structure of $SrTiO_3$(100)-($\sqrt{5} \times \sqrt{5}$)-R26.6°", Physical Review Letters **86**, 1801–1804 (2001).

[74]D. Newell, A. Harrison, F. Silly, and M. Castell, "$SrTiO_3$(001)-(5×5)-R26.6° reconstruction: A surface resulting from phase separation in a reducing environment", Physical Review B **75**, 205429 (2007).

[75]M. R. Castell, "Scanning tunneling microscopy of reconstructions on the $SrTiO_3$(001) Surface", Surface Science **505**, 1–13 (2002).

[76]D. Jiang and J. Zegenhagen, "c(6×2) and c(4×2) reconstructions of the $SrTiO_3$ (001)", Surface Science **425**, 343–354 (1999).

[77]H. L. Marsh, D. S. Deak, F. Silly, a. I. Kirkland, and M. R. Castell, "Hot STM of nanostructure dynamics on $SrTiO_3$ (001).", Nanotechnology **17**, 3543–3548 (2006).

[78]D. S. Deak, F. Silly, D. T. Newell, and M. R. Castell, "Ordering of TiO2-Based Nanostructures on $SrTiO_3$(001) Surfaces.", The Journal of Physical Chemistry B **110**, 9246–9251 (2006).

[79]T. Beck, A. Klust, M. Batzill, U. Diebold, C. Di Valentin, and A. Selloni, "Surface Structure of TiO_2 (011)-(2×1)", Physical Review Letters **93**, 036104 (2004).

[80]F. Bottin, F. Finocchi, and C. Noguera, "Facetting and (n×1) reconstructions of $SrTiO_3$ (110) surfaces", Surface Science **574**, 65–76 (2005).

[81]Y. Cao, S. Wang, S. Liu, Q. Guo, and J. Guo, "Electronic structures of the $SrTiO_3$(110) surface in different reconstructions", The Journal of Chemical Physics **137**, 044701 (2012).

[82]A. N. Chiaramonti, C. H. Lanier, L. D. Marks, and P. C. Stair, "Time, temperature, and oxygen partial pressure-dependent surface reconstructions on $SrTiO_3$(111): A systematic study of oxygen-rich conditions", Surface Science **602**, 3018–3025 (2008).

[83]J. Feng, X. Zhu, and J. Guo, "Reconstructions on $SrTiO_3$(111) surface tuned by Ti/Sr deposition", Surface Science **614**, 38–45 (2013).

[84]B. C. Russell and M. R. Castell, "Surface of Sputtered and Annealed Polar $SrTiO_3$(111): TiO_x-Rich (n×n) Reconstructions", The Journal of Physical Chemistry C **112**, 6538–6545 (2008).

[85]B. Russell and M. Castell, "(13×13)R13.9 and (7×7)R19.1 reconstructions of the polar $SrTiO_3$(111) surface", Physical Review B **75**, 155433 (2007).

[86]L. M. Liborio, C. G. Sanchez, A. T. Paxton, and M. W. Finnis, "Stability of Sr adatom model structures for $SrTiO_3$ (001) surface reconstructions", Journal of Physics: Condensed Matter **17**, L223–L230 (2005).

[87]Y. Zhu, H. Inada, K. Nakamura, and J. Wall, "Imaging single atoms using secondary electrons with an aberration-corrected electron microscope", Nature Materials **8**, 808–812 (2009).

[88]L. Wu, R. F. Egerton, and Y. Zhu, "Image Simulation for Atomic Resolution Secondary Electron Image.", Ultramicroscopy **123**, 66–73 (2012).

[89]H. Brown, A. D'Alfonso, and L. Allen, "Secondary Electron Imaging at Atomic Resolution Using a Focused Coherent Electron Probe", Physical Review B **87**, 054102 (2013).

[90]M. P. Seah and W. A. Dench, "Quantitative electron spectroscopy of surfaces: a standard data base for electron inelastic mean free paths in solids", Surface and Interface Analysis **1**, 2–11 (1979).

[91]C. Hogan, M. Palummo, and R. D. Sole, "Theory of dielectric screening and electron energy loss spectroscopy at surfaces", Comptes Rendus Physique **10**, 560–574 (2009).

[92]K. X. Hu and I. P. Jones, "Low electron energy-loss spectroscopy study of the electronic structure of matrix and $\Sigma 9$, $\Sigma 13$ boundaries in $SrTiO_3$", Journal of Physics D: Applied Physics **38**, 183 (2005).

[93]E. Bengu, R. Plass, L. Marks, T. Ichihashi, P. Ajayan, and S. Iijima, "Imaging the Dimers in Si(111)-(7×7).", Physical Review Letters **77**, 4226–4228 (1996).

[94]P. J. Moller, A. Komolov, and F. Lazneva, "Selective growth of a MgO (100) -c(2×2) superstructure on a $SrTiO_3$ (100)-(2×2) substrate", Surface Science **425**, 15–21 (1999).

[95]D. S. Deak, F. Silly, K. Porfyrakis, and M. R. Castell, "Controlled surface ordering of endohedral fullerenes with a $SrTiO_3$ template.", Nanotechnology **18**, 75301 (2007).

[96]J. Feng, X. Zhu, and J. Guo, "Reconstructions on $SrTiO_3$(111) surface tuned by Ti/Sr deposition", Surface Science **614**, 38–45 (2013).

[97]a. Pancotti, N. Barrett, L. F. Zagonel, and G. M. Vanacore, "Multiple scattering x-ray photoelectron diffraction study of the $SrTiO_3$(100) surface", Journal of Applied Physics **106**, 34104 (2009).

[98]O. Bunk, G. Falkenberg, J. H. Zeysing, L. Lottermoser, and R. L. Johnson, "Structure determination of the indium-induced Si(111)-(4×1) reconstruction by surface x-ray diffraction", Phys. Rev. B **59**, 12228–12231 (1999).

[99]J. Cheng, P. Regreny, L. Largeau, G. Patriarche, O. Mauguin, K. Naji, G. Hollinger, and G. Saint-Girons, "Influence of the surface reconstruction on the growth of InP on $SrTiO_3$ (001)", Journal of Crystal Growth **311**, 1042–1045 (2009).

[100]M. Naito and H. Sato, "Reflection High-Energy Electron Diffraction Study on the $SrTiO_3$ Surface Structure", Physica C **229**, 1–11 (1994).

[101]D. N. Dunn, P. Xu, and L. D. Marks, "UHV transmission electron microscopy of Ir (001) I. Microstructure of the (1×1) and the reconstructed (5×1) surfaces", Surface Science **294**, 308–321 (1993).

[102]S. Li, R. Li, R. Guan, H. Ye, and J. Zhu, "Plan-view Imaging of Oxygen-induced Reconstruction on Ag(110) Surface. I. The Possibility of Imaging Surface Oxygen", Journal of Electron Microscopy **49**, 163–172 (2000).

[103]L. D. Marks, "Registry and UHV Transmission Electron Diffraction of Surfaces", Ultramicroscopy **45**, 145–154 (1992).

[104]L. D. Marks, P. Xu, and D. N. Dunn, "UHV Transmission Electron-Microscopy of Ir(001) .II. Atomic Positions of the (5×1) Reconstructed Surface from HREM and R-Factor Refinements", Surface Science **294**, 322–332 (1993).

[105]L. D. Marks, "Rigor, and Plan-view Simulation of Surfaces", Ultramicroscopy **38**, 325–332 (1991).

[106]L. D. Marks and R. Plass, "Atomic Structure of Si(111)-(5×2)-Au from High Resolution Electron Microscopy and Heavy-Atom Holography", Phys. Rev. Lett. **75**, 2172–2175 (1995).

[107]P. Xu and L. D. Marks, "Intensities of Surface Diffraction Spots in Plan View", Ultramicroscopy **45**, 155–157 (1992).

[108]N. Ikarashi, K. Kobayashi, H. Koike, H. Hasegawa, and K. Yagi, Ultramicroscopy **26**, 195–203 (1988).

[109]M. A. Gribelyuk, P. J. F. Harris, and J. L. Hutchison, Philosophical Magazine Part B **69**, 655–669 (1994).

[110]P. Xu, D. N. Dunn, J. P. Zhang, and L. D. Marks, "Atomic Imaging of Surfaces in Plan View", Surface Science Letters **285**, L479–L485 (1993).

[111]L. D. Marks, V. Heine, and D. J. Smith, "Direct observation of elastic and plastic deformations at the Au(111) Surfaces", Phys. Rev. Lett. **52**, 656–658 (1984).

[112]L. D. Marks, "Direct atomic imaging of solid surfaces I. Image Simulation and Interpretation", Surface Science **139**, 281–298 (1984).

[113]L. D. Marks, "Surface structure and energetics of multiply twinned particles", Philosophical Magazine A **49**, 81–93 (1984).

[114]L. D. Marks and D. J. Smith, "Direct atomic imaging of solid surfaces II. Gold (111) surfaces during and after in situ carbon etching", Surface Science **143**, 495–508 (1984).

[115]D. J. Smith and L. Marks, "Direct atomic imaging of solid surfaces III. Small particles and extended Au surfaces", Ultramicroscopy **16**, 101–114 (1985).

[116]L. D. Marks and D. J. Smith, "Direct Atomic Imaging of Solid Surfaces IV. Dislocations on Au(100)", Surface Science Letters **157**, 367–372 (1985).

[117]L. D. Marks, "Direct Imaging of Carbon-Covered and Clean Gold (110) Surfaces", Phys. Rev. Lett. **51**, 1000–1002 (1983).

[118]L. D. Marks and D. J. Smith, "High resolution studies of small particles of gold and silver I. Multiply-twinned particles", Journal of Crystal Growth **54**, 425–432 (1981).

[119]D. Smith and L. Marks, "High resolution studies of small particles of gold and silver: II. Single crystals, lamellar twins and polyparticles", Journal of Crystal Growth **54**, 433–438 (1981).

[120]L. D. Marks and A. Howie, "Multiply-twinned particles in silver catalysts", Nature **282**, 196–198 (1979).

[121]A. Howie, L. D. Marks, and S. J. Pennycook, "New Imaging Methods for Catalyst Particles", Ultramicroscopy **8**, 163–174 (1982).

[122]Y. Lin, J. Wen, L. Hu, R. M. Kennedy, P. C. Stair, K. R. Poeppelmeier, and L. D. Marks, "Synthesis-dependent atomic surface structures of oxide nanoparticles", Physical Review Letters **111**, 1–5 (2013).

[123]Y. Lin, Z. Wu, J. Wen, K. R. Poeppelmeier, and L. D. Marks, "Imaging the Atomic Surface Structures of CeO_2 Nanoparticles", Nano Letters **14**, 191–196 (2014).

[124]J. L. Hutchison and N. A. Briscoe, Ultramicroscopy **18**, 435–438 (1985).

[125]A. K. Datye and D. J. Smith, "The Study of Heterogeneous Catalysts by High-Resolution Transmission Electron Microscopy", Catalysis Reviews **34**, 129–178 (1992).

[126]L. C. Gontard, L. Y. Chang, C. J. Hetherington, A. I. Kirkland, D. Ozkaya, and R. E. Dunin-Borkowski, "Aberration-corrected imaging of active sites on industrial catalyst nanoparticles", Angew Chem Int Ed Engl **46**, 3683–3685 (2007).

[127]P. L. Hansen, J. B. Wagner, S. Helveg, J. R. Rostrup-Nielsen, B. S. Clausen, and H. Topsoe, "Atom-resolved imaging of dynamic shape changes in supported copper nanocrystals", Science **295**, 2053–2055 (2002).

[128]D. A. Jefferson and P. J. F. Harris, "Direct imaging of an adsorbed layer by high-resolution electron microscopy", Nature **332**, 617–620 (1988).

[129]J. O. Bovin, R. Wallenberg, and D. J. Smith, "Imaging of atomic clouds outside the surfaces of gold crystals by electron microscopy", Nature **317**, 47–49 (1985).

[130]D. J. Smith and L. D. Marks, "Direct lattice imaging of small metal particles", Philosophical Magazine A **44**, 735–740 (1981).

[131]L. D. Marks and D. J. Smith, "Direct surface imaging in small metal particles", Nature **303**, 316–317 (1983).

[132]C. J. Gilmore, L. D. Marks, D. Grozea, C. Collazo, E. Landree, and R. D. Twesten, "Direct Solutions of the Si (111) 7×7 Structure", Surface Science **381**, 77–91 (1997).

[133]R. Kilaas, *MacTempasX*, 2015.

[134]R. Kilaas, L. D. Marks, and C. S. Own, "EDM 1.0: electron direct methods", Ultramicroscopy **102**, 233–237 (2005).

[135]R. Plass and L. D. Marks, "UHV Transmission Electron-Microscopy Structure Determination of the Si(111)-($\sqrt{3} \times \sqrt{3}$)-R30°-Au Surface", Surface Science **342**, 233–249 (1995).

[136]C. Collazo-Davila, D. Grozea, E. Landree, and L. D. Marks, "Transmission electron diffraction determination of the Ge(001)- (2×1) surface structure", Surface Science **375**, 293–301 (1997).

[137]C. Collazo-Davila, D. Grozea, and L. D. Marks, "Determination and refinement of the Ag/Si(111)-(3×1) surface structure", Physical Review Letters **80**, 1678–1681 (1998).

[138]M. E. Lines and A. M. Glass, *"Principles and Application of Ferroelectrics and Related Materials"* (Claredon Press, Oxford, 1977).

[139]R. G. Geyer, B. Riddle, J. Krupka, and L. A. Boatner, "Microwave dielectric properties of single-crystal quantum paraelectrics $KTaO_3$ and $SrTiO_3$ at cryogenic temperatures", Journal of Applied Physics **97**, 104111 (2005).

[140]T. Ishihara, H. Nishiguchi, K. Fukamachi, and Y. Takita, "Effects of Acceptor Doping to $KTaO_3$ on Photocatalytic Decomposition of Pure H_2O", The Journal of Physical Chemistry B **103**, 1–3 (1999).

[141]H. Hayashi and Y. Hakuta, "Hydrothermal epitaxy of $KTaO_3$ thin films under supercritical water conditions", Journal of Materials Science **43**, 2342–2347 (2007).

[142]E. Specht, H. Christen, D. Norton, and L. Boatner, "X-ray diffraction measurement of the effect of layer thickness on the ferroelectric transition in epitaxial $KTaO_3/KNbO_3$ multilayers", Physical Review Letters **80**, 4317–4320 (1998).

[143]J. Sigman, D. Norton, H. Christen, P. Fleming, and L. Boatner, "Antiferroelectric behavior in symmetric $KNbO_3/KTaO_3$ superlattices", Physical Review Letters **88**, 097601 (2002).

[144]J. G. Fisher, A. Bencan, J. Holc, M. Kosec, S. Vernay, and D. Rytz, "Growth of potassium sodium niobate single crystals by solid state crystal growth", Journal of Crystal Growth **303**, 487–492 (2007).

[145]O. Aktas, S. Crossley, M. A. Carpenter, and E. K. H. Salje, "Polar correlations and defect-induced ferroelectricity in cryogenic $KTaO_3$", Physical Review B **90**, 165309 (2014).

[146]W. S. Baer, "Faraday Rotation in $KTaO_3$", Physical Review Letters **16**, 729–731 (1966).

[147]W. R. Hosler and H. P. R. Frederikse, "Magnetoresistive effects in $KTaO_3$", Solid State Communications **7**, 1443–1449 (1969).

[148]K. W. Johnson and D. H. Olson, "Electron Tunneling into $KTaO_3$ Schottky Barrier Junctions", Physical Review B **3**, 1244–1248 (1971).

[149]P. Kim, K. T. Kang, G. Go, and J. H. Han, "Nature of orbital and spin Rashba coupling in the surface bands of $SrTiO_3$ and $KTaO_3$", Physical Review B **90**, 205423 (2014).

[150]G. Shirane, R. Nathans, and V. J. Minkiewicz, "Temperature Dependence of the Soft Ferroelectric Mode in $KTaO_3$", Physical Review **157**, 396–399 (1967).

[151]V. Skoromets, C. Kadlec, H. Nemec, D. Fattakhova-Rohlfing, and P. Kuzel, "Tunable dielectric properties of $KTaO_3$ single crystals in the terahertz range", Journal of Physics D: Applied Physics **49**, 065306 (2016).

[152]S. Triebwasser, "Study of Ferroelectric Transitions of Solid-Solution Single Crystals of $KNbO_3$-$KTaO_3$", Physical Review **114**, 63–70 (1959).

[153]K. Ueno, I. H. Inoue, T. Yamada, H. Akoh, Y. Tokura, and H. Takagi, "Field-effect transistor based on $KTaO_3$ perovskite", Applied Physics Letters **84**, 3726 (2004).

[154]L. Wu, H. Li, L. Jiang, C. Ding, Q. Sheng, X. Ding, and J. Yao, "Modulation of dielectric properties of $KTaO_3$ in terahertz region via 532nm continuous-wave laser", Optical Materials Express **4**, 2595–2601 (2014).

[155]Y. Yang, C.-S. Lin, J.-F. Chen, L. Hu, and W.-D. Cheng, "Ferromagnetic-nonmagnetic and metal-insulator phase transitions at the interfaces of $KTaO_3$ and $PbTiO_3$", Journal of Applied Physics **116**, 153709 (2014).

[156]M. Marchelek, B. Bajorowicz, P. Mazierski, A. Cybula, T. Klimczuk, M. Winiarski, N. Fijalkowska, and A. Zaleska, "$KTaO_3$-based nanocomposites for air treatment", Catalysis Today **252**, 47–53 (2015).

[157]K. Zou, S. Ismail-Beigi, K. Kisslinger, X. Shen, D. Su, F. J. Walker, and C. H. Ahn, "$LaTiO_3/KTaO_3$ interfaces: A new two-dimensional electron gas system", APL Materials **3**, 036104 (2015).

[158]I. Golovina, S. Kolesnik, V. Bryksa, V. Strelchuk, I. Yanchuk, I. Geifman, S. Khainakov, S. Svechnikov, and A. Morozovska, "Defect driven ferroelectricity and magnetism in nanocrystalline $KTaO_3$", Physica B: Condensed Matter **407**, 614–623 (2012).

[159]P. A. Fleury and J. M. Worlock, "Electric-Field-Induced Raman Scattering in $SrTiO_3$ and $KTaO_3$", Physical Review **174**, 613–623 (1968).

[160]A. I. Lebedev, "Quasi-two-dimensional Ferroelectricity in $KNbO_3$-$KTaO_3$ Superlattices", Physics of the Solid State **53**, 2463–2467 (2011).

[161]E. a. Eliseev, M. D. Glinchuk, and a. N. Morozovska, "Appearance of Ferroelectricity in Thin Films of Incipient Ferroelectric", Physica Status Solidi (B) **244**, 3660–3672 (2007).

[162]C. Fisher, C. auf der Horst, P. Voigt, S. Kapphan, and J. Zhao, "Luminicence and optical second harmonic generation by dipolar microregions in $KTaO_3$", Radiation Effects and Defects in Solids **136**, 85 (1995).

[163]J. Li, E. Akhadov, J. Baker, L. Boatner, D. Bonart, J. Fritsch, S. Safron, U. Schroder, J. Skofronick, and T. Trelenberg, "Surface structure and dynamics of KTaO3 (001)", Physical Review B **68**, 045402 (2003).

[164]Y. B. Xu, Y. L. Tang, Y. Liu, X. L. Ma, and Y. L. Zhu, "Atomically resolved precipitates/matrix interfaces in $KTaO_3$ crystals", Philosophical Magazine **96**, 486–497 (2016).

[165]A. A. Awadalla and B. M. Gatehouse, "Crystal structures of some niobium and tantalum oxides. III $K_6Ta_10.8O_30$ - A partially Filled tetragonal tungsten bronze-like structure", Journal of Solid State Chemistry **23**, 349–355 (1978).

[166]R. H. Lamoreaux and D. L. Hildenbrand, "High Temperature Vaporization Behavior of Oxides. I. Alkali Metal Binary Oxides", Journal of Physical and Chemical Reference Data **13**, 151–173 (1984).

[167]H.-j. Bae, J. Sigman, D. Norton, and L. Boatner, "Surface treatment for forming unit-cell steps on the (001) $KTaO_3$ substrate surface", Applied Surface Science **241**, 271–278 (2005).

[168]X. T. Zeng and H. K. Wong, "Epitaxial growth of single-crystal (LaCa)MnO_3 thin films", Applied Physics Letters **66**, 3371–3373 (1995).

[169]X. Tan, G. Gao, P. Chen, H. Xu, B. Zhi, F. Jin, F. Chen, and W. Wu, "Enhancing the orthorhombicity and antiferromagnetic-insulating state in epitaxial $La_{0.67}Ca_{0.33}MnO_3$-$NdGaO_3$(001) films by inserting a $SmFeO_3$ buffer layer", Journal of Applied Physics **116**, 203706 (2014).

[170]C. Ma, D. Han, M. Liu, G. Collins, H. Wang, X. Xu, Y. Lin, J. Jiang, S. Zhang, and C. Chen, "Anisotropic Strain Induced Directional Metallicity in Highly Epitaxial $LaBaCo_2O_{5.5+\delta}$ Thin Films on (110) $NdGaO_3$", Scientific Reports **6**, 37337 (2016).

[171]M. Liu, Q. Zou, C. Ma, G. Collins, S.-B. Mi, C.-L. Jia, H. Guo, H. Gao, and C. Chen, "Strain-Induced Anisotropic Transport Properties of $LaBaCo_2O_{5.5+\delta}$ Thin Films on $NdGaO_3$ Substrates", ACS Applied Materials & Interfaces **6**, 8526–8530 (2014).

[172]V. M. Orera, L. E. Trinkler, R. I. Merino, and A. Larrea, "The optical properties of the Nd^{3+} ion in $NdGaO_3$ and $LaGaO_3$:Nd: temperature and concentration dependence", Journal of Physics: Condensed Matter **7**, 9657 (1995).

[173]M. Schmidbauer, A. Kwasniewski, and J. Schwarzkopf, "High-precision absolute lattice parameter determination of $SrTiO_3$, $DyScO_3$ and $NdGaO_3$ single crystals", Acta Crystallogr B **68**, 8–14 (2012).

[174]C. Li, Q. Xu, Z. Wen, S. Zhang, A. Li, and D. Wu, "The metallic interface between insulating $NdGaO_3$ and $SrTiO_3$ perovskites", Applied Physics Letters **103**, 201602 (2013).

[175]X. K. Lian, F. Chen, X. L. Tan, P. F. Chen, L. F. Wang, G. Y. Gao, S. W. Jin, and W. B. Wu, "Anisotropic-strain-controlled metal-insulator transition in epitaxial $NdNiO_3$ films grown on orthorhombic $NdGaO_3$ substrates", Applied Physics Letters **103**, 172110 (2013).

[176]R. L. Sandstrom, E. A. Giess, W. J. Gallagher, A. Segmuller, E. I. Cooper, M. F. Chisholm, A. Gupta, S. Shinde, and R. B. Laibowitz, "Lanthanum Gallate Substrates

for Epitaxial High Temperature Superconducting Thin Films", Applied Physics Letters **53**, 1874–1876 (1988).

[177]T. Konaka, M. Sato, H. Asano, and S. Kubo, "Relative permittivity and dielectric loss tangent of substrate materials for high-tc superconducting film", Journal of Superconductivity **4**, 283–288 (1991).

[178]V. Leca and E. Andronescu, "Improved Surface Morphology of (110) $NdGaO_3$ Substrates by Thermal and Chemical Treatments", Revista Romana de Materiale-Romanian Journal of Materials **41**, 127–131 (2011).

[179]R. Dirsyte, J. Schwarzkopf, G. Wagner, J. Lienemann, M. Busch, H. Winter, and R. Fornari, "Surface termination of the $NdGaO_3$(110)", Applied Surface Science **255**, 8685–8687 (2009).

[180]A. Cavallaro, G. F. Harrington, S. J. Skinner, and J. a. Kilner, "Controlling the surface termination of $NdGaO_3$ (110): the role of the gas atmosphere.", Nanoscale **6**, 7263–73 (2014).

[181]W. Boettinger, C. Johnson, L. Bendersky, K.-W. Moon, M. Williams, and G. Stafford, "Whisker and hillock formation on sn, sn-cu and sn-pb electrodeposits", Acta Materialia **53**, 5033–5050 (2005).

[182]K. N. Tu, "Irreversible processes of spontaneous whisker growth in bimetallic cu-sn thin-film reactions", Phys. Rev. B **49**, 2030–2034 (1994).

[183]J. Ham, W. Shim, D. H. Kim, K. H. Oh, P. W. Voorhees, and W. Lee, "Watching bismuth nanowires grow", Applied Physics Letters **98**, 043102 (2011).

[184]S. Nakayama, M. Sakamoto, M. Higuchi, K. Kodaira, M. Sato, S. Kakita, T. Suzuki, and K. Itoh, "Oxide ionic conductivity of apatite type $Nd_{9.33}(SiO_4)_6O_2$ single crystal", Journal of the European Ceramic Society **19**, 507–510 (1999).

[185]E. V. Bursian and Zaikovsk.Oi, "Changes in Curvature of a Ferroelectric Film Due to Polarization", Soviet Physics Solid State **10**, 1121 (1968).

[186]R. B. Meyer, "Piezoelectric Effects in Liquid Crystals", Physical Review Letters **22**, 918–921 (1969).

[187]V. L. Indenbom, E. B. Loginov, and M. A. Osipov, "Flexoelectric Effect and Crystal-Structure", Kristallografiya **26**, 1157–1162 (1981).

[188]A. G. Petrov, "Flexoelectricity of model and living membranes", Biochim Biophys Acta **1561**, 1–25 (2002).

[189]A. K. Tagantsev, "Piezoelectricity and flexoelectricity in crystalline dielectrics", Phys Rev B Condens Matter **34**, 5883–5889 (1986).

[190]P. V. Yudin and A. K. Tagantsev, "Fundamentals of flexoelectricity in solids", Nanotechnology **24**, 432001 (2013).

[191]K. Abe, S. Komatsu, N. Yanase, K. Sano, and T. Kawakubo, "Asymmetric ferroelectricity and anomalous current conduction in heteroepitaxial $BaTiO_3$ thin films", Japanese Journal of Applied Physics Part 1-Regular Papers Short Notes & Review Papers **36**, 5846–5853 (1997).

[192]A. Tagantsev, L. E. Cross, and J. Fousek, *Domains in Ferroic Crystals and Thin Films* (Springer New York, 2010).

[193]G. Catalan, L. J. Sinnamon, and J. M. Gregg, "The effect of flexoelectricity on the dielectric properties of inhomogeneously strained ferroelectric thin films", Journal of Physics-Condensed Matter **16**, 2253–2264 (2004).

[194]E. A. Eliseev, A. N. Morozovska, M. D. Glinchuk, and R. Blinc, "Spontaneous flexoelectric/flexomagnetic effect in nanoferroics", Physical Review B **79**, 10 (2009).

[195]M. S. Majdoub, R. Maranganti, and P. Sharma, "Understanding the origins of the intrinsic dead layer effect in nanocapacitors", Physical Review B **79**, 115412 (2009).

[196]A. Gruverman, B. J. Rodriguez, A. I. Kingon, R. J. Nemanich, A. K. Tagantsev, J. S. Cross, and M. Tsukada, "Mechanical stress effect on imprint behavior of integrated ferroelectric capacitors", Applied Physics Letters **83**, 728–730 (2003).

[197]E. A. Eliseev, A. N. Morozovska, G. S. Svechnikov, P. Maksymovych, and S. V. Kalinin, "Domain wall conduction in multiaxial ferroelectrics", Physical Review B **85**, 45312 (2012).

[198]E. A. Eliseev, A. N. Morozovska, Y. J. Gu, A. Y. Borisevich, L. Q. Chen, V. Gopalan, and S. V. Kalinin, "Conductivity of twin-domain-wall/surface junctions in ferroelastics: Interplay of deformation potential, octahedral rotations, improper ferroelectricity, and flexoelectric coupling", Physical Review B **86**, 85416 (2012).

[199]A. N. Morozovska, E. A. Eliseev, M. D. Glinchuk, L. Q. Chen, and V. Gopalan, "Interfacial polarization and pyroelectricity in antiferrodistortive structures induced by a flexoelectric effect and rotostriction", Physical Review B **85**, 94107 (2012).

[200]D. Lee, B. C. Jeon, A. Yoon, Y. J. Shin, M. H. Lee, T. K. Song, S. D. Bu, M. Kim, J. S. Chung, J. G. Yoon, and T. W. Noh, "Flexoelectric control of defect formation in ferroelectric epitaxial thin films", Adv Mater **26**, 5005–5011 (2014).

[201]M. Gharbi, Z. H. Sun, P. Sharma, and K. White, "The origins of electromechanical indentation size effect in ferroelectrics", Applied Physics Letters **95**, 142901 (2009).

[202]C. R. Robinson, K. W. White, and P. Sharma, "Elucidating the mechanism for indentation size-effect in dielectrics", Applied Physics Letters **101**, 122901 (2012).

[203]K. Chu, B. K. Jang, J. H. Sung, Y. A. Shin, E. S. Lee, K. Song, J. H. Lee, C. S. Woo, S. J. Kim, S. Y. Choi, T. Y. Koo, Y. H. Kim, S. H. Oh, M. H. Jo, and C. H. Yang, "Enhancement of the anisotropic photocurrent in ferroelectric oxides by strain gradients", Nat Nanotechnol **10**, 972–979 (2015).

[204]A. N. Morozovska, Y. M. Vysochanskii, O. V. Varenyk, M. V. Silibin, S. V. Kalinin, and E. A. Eliseev, "Flexocoupling impact on the generalized susceptibility and soft phonon modes in the ordered phase of ferroics", Physical Review B **92**, 94308 (2015).

[205]Q. Deng, M. Kammoun, A. Erturk, and P. Sharma, "Nanoscale flexoelectric energy harvesting", International Journal of Solids and Structures **51**, 3218–3225 (2014).

[206]X. N. Jiang, W. B. Huang, and S. J. Zhang, "Flexoelectric nano-generator: Materials, structures and devices", Nano Energy **2**, 1079–1092 (2013).

[207]C. C. Liu, S. L. Hu, and S. P. Shen, "Effect of Flexoelectricity on Band Structures of One-Dimensional Phononic Crystals", Journal of Applied Mechanics-Transactions of the Asme **81**, 6 (2014).

[208]W. B. Huang, S. R. Yang, N. Y. Zhang, F. G. Yuan, and X. N. Jiang, "Direct Measurement of Opening Mode Stress Intensity Factors Using Flexoelectric Strain Gradient Sensors", Experimental Mechanics **55**, 313–320 (2015).

[209]W. H. Ma, "A study of flexoelectric coupling associated internal electric field and stress in thin film ferroelectrics", Physica Status Solidi B-Basic Solid State Physics **245**, 761–768 (2008).

[210]R. Resta, "Towards a bulk theory of flexoelectricity", Physical Review Letters **105**, 127601 (2010).

[211]R. Resta, "Electrical polarization and orbital magnetization: the modern theories", J Phys Condens Matter **22**, 123201 (2010).

[212]M. Stengel, "Surface control of flexoelectricity", Physical Review B **90**, 5 (2014).

[213]I. Ponomareva, A. K. Tagantsev, and L. Bellaiche, "Finite-temperature flexoelectricity in ferroelectric thin films from first principles", Physical Review B **85**, 104101 (2012).

[214]M. Stengel, "Unified ab initio formulation of flexoelectricity and strain-gradient elasticity", Phys. Rev. B **93**, 245107 (2016).

[215]M. Stengel, "Microscopic response to inhomogeneous deformations in curvilinear coordinates", Nat Commun **4**, 2693 (2013).

[216]S. Mao and P. K. Purohit, "Insights Into Flexoelectric Solids From Strain-Gradient Elasticity", Journal of Applied Mechanics-Transactions of the Asme **81**, 10 (2014).

[217]W. B. Huang, K. Kim, S. J. Zhang, F. G. Yuan, and X. N. Jiang, "Scaling effect of flexoelectric (Ba,Sr)TiO3 microcantilevers", Physica Status Solidi-Rapid Research Letters **5**, 350–352 (2011).

[218]H. Lu, C. W. Bark, D. Esque de los Ojos, J. Alcala, C. B. Eom, G. Catalan, and A. Gruverman, "Mechanical writing of ferroelectric polarization", Science **336**, 59–61 (2012).

[219]T. D. Nguyen, S. Mao, Y. W. Yeh, P. K. Purohit, and M. C. McAlpine, "Nanoscale flexoelectricity", Adv Mater **25**, 946–974 (2013).

[220]W. H. Ma and L. E. Cross, "Flexoelectric polarization of barium strontium titanate in the paraelectric state", Applied Physics Letters **81**, 3440–3442 (2002).

[221]L. E. Cross, "Flexoelectric effects: Charge separation in insulating solids subjected to elastic strain gradients", Frontiers of Ferroelectricity: A Special Issue of the Journal of Materials Science **41**, 53–63 (2006).

[222]P. Zubko, G. Catalan, A. Buckley, P. R. Welche, and J. F. Scott, "Strain-gradient-induced polarization in SrTiO3 single crystals", Physical Review Letters **99**, 167601 (2007).

[223]A. Kholkin, I. Bdikin, T. Ostapchuk, and J. Petzelt, "Room temperature surface piezoelectricity in SrTiO3 ceramics via piezoresponse force microscopy", Applied Physics Letters **93**, 3 (2008).

[224]G. Catalan, A. Lubk, A. H. G. Vlooswijk, E. Snoeck, C. Magen, A. Janssens, G. Rispens, G. Rijnders, D. H. A. Blank, and B. Noheda, "Flexoelectric rotation of polarization in ferroelectric thin films", Nature Materials **10**, 963–967 (2011).

[225]U. K. Bhaskar, N. Banerjee, A. Abdollahi, Z. Wang, D. G. Schlom, G. Rijnders, and G. Catalan, "A flexoelectric microelectromechanical system on silicon", Nat Nanotechnol **11**, 263–266 (2015).

[226]D. Lee, A. Yoon, S. Y. Jang, J. G. Yoon, J. S. Chung, M. Kim, J. F. Scott, and T. W. Noh, "Giant flexoelectric effect in ferroelectric epitaxial thin films", Physical Review Letters **107**, 57602 (2011).

[227]P. Novak, J. Kunes, L. Chaput, and W. E. Pickett, "Exact exchange for correlated electrons", Physica Status Solidi B-Basic Solid State Physics **243**, 563–572 (2006).

[228]J. P. Perdew, A. Ruzsinszky, G. I. Csonka, O. A. Vydrov, G. E. Scuseria, L. A. Constantin, X. Zhou, and K. Burke, "Restoring the density-gradient expansion for exchange in solids and surfaces", Physical Review Letters **100**, 136406 (2008).

[229]M. C. Biesinger, L. W. M. Lau, A. R. Gerson, and R. S. C. Smart, "Resolving surface chemical states in XPS analysis of first row transition metals, oxides and hydroxides: Sc, Ti, V, Cu and Zn", Applied Surface Science **257**, 887–898 (2010).

[230]P. Koirala, *Supplementary Videos* $DyScO_3$. `http://www.numis.northwestern.edu/Research/Projects/flexo/`.

[231]X. Ke, C. Adamo, D. G. Schlom, M. Bernhagen, R. Uecker, and P. Schiffer, "Low temperature magnetism in the perovskite substrate $DyScO_3$", Applied Physics Letters **94**, 152503 (2009).

[232]M. Janovska, P. Sedlak, H. Seiner, M. Landa, P. Marton, P. Ondrejkovic, and J. Hlinka, "Anisotropic elasticity of $DyScO_3$ substrates", J Phys Condens Matter **24**, 385404 (2012).

[233]W. D. Rau, P. Schwander, F. H. Baumann, W. Hoppner, and A. Ourmazd, "Two-dimensional mapping of the electrostatic potential in transistors by electron holography", Physical Review Letters **82**, 2614–2617 (1999).

[234]J. W. Chen, G. Matteucci, A. Migliori, G. F. Missiroli, E. Nichelatti, G. Pozzi, and M. Vanzi, "Mapping of microelectrostatic fields by means of electron holography: Theoretical and experimental results", Phys Rev A **40**, 3136–3146 (1989).

[235]M. T. Woodside and P. L. McEuen, "Scanned probe imaging of single-electron charge states in nanotube quantum dots", Science **296**, 1098–1101 (2002).

[236]M. J. Yoo, T. A. Fulton, H. F. Hess, R. L. Willett, L. N. Dunkleberger, R. J. Chichester, L. N. Pfeiffer, and K. W. West, "Scanning Single-Electron Transistor Microscopy: Imaging Individual Charges", Science **276**, 579–582 (1997).

[237]S. Chung, R. A. Berechman, M. R. McCartney, and M. Skowronski, "Electronic structure analysis of threading screw dislocations in 4H-SiC using electron holography", Journal of Applied Physics **109**, 34906 (2011).

[238]C. Gatel, A. Lubk, G. Pozzi, E. Snoeck, and M. Hytch, "Counting elementary charges on nanoparticles by electron holography", Physical Review Letters **111**, 25501 (2013).

[239]P. Koirala, C. Mizzi, and L. Marks, "Direct observation of large flexoelectric bending at the nanoscale in Lanthanide Scandates", arXiv:1511.07791v2 (2016).

[240]J. Ciston, A. Subramanian, and L. D. Marks, "Water-driven structural evolution of the polar MgO (111) surface: An integrated experimental and theoretical approach", Physical Review B **79**, 085421 (2009).

[241]M. D. Biegalski, Y. Jia, D. G. Schlom, S. Trolier-McKinstry, S. K. Streiffer, V. Sherman, R. Uecker, and P. Reiche, "Relaxor ferroelectricity in strained epitaxial $SrTiO_3$ thin films on $DyScO_3$ substrates", Applied Physics Letters **88**, 192907 (2006).

[242]S. Karimoto and M. Naito, "Electron-doped infinite-layer thin films with Tc over 40 K grown on $DyScO_3$ substrates", Applied Physics Letters **84**, 2136–2138 (2004).

[243]C. Kadlec, V. Skoromets, F. Kadlec, H. Nemec, J. Hlinka, J. Schubert, G. Panaitov, and P. Kuzel, "Temperature and electric field tuning of the ferroelectric soft mode in a strained SrTiO3/DyScO3 heterostructure", Physical Review B **80**, 174116 (2009).

[244]P. Kuzel, F. Kadlec, J. Petzelt, J. Schubert, and G. Panaitov, "Highly tunable $SrTiO_3$-$DyScO_3$ heterostructures for applications in the terahertz range", Applied Physics Letters **91**, 232911 (2007).

[245]P. Kuzel, C. Kadlec, F. Kadlec, J. Schubert, and G. Panaitov, "Field-induced soft mode hardening in $SrTiO_3$/$DyScO_3$ multilayers", Applied Physics Letters **93**, 52910 (2008).

[246]S. Kamba, V. Goian, D. Nuzhnyy, V. Bovtun, M. Kempa, J. Prokleska, M. Bernhagen, R. Uecker, and D. G. Schlom, "Polar phonon anomalies in single-crystalline $TbScO_3$", Phase Transitions **86**, 206–216 (2013).

[247]J. Goraus and A. Slebarski, "Onsite hybridization between Ce 4f and 5d states as the indicator of the transition from Kondo insulator to metallic state in CeRhSb", Physics Letters A **375**, 3469–3473 (2011).

[248]K. Iwasa, L. Hao, K. Kuwahara, M. Kohgi, S. R. Saha, H. Sugawara, Y. Aoki, and H. Sato, "Drastic evolution of 4f-electron states in the metal-insulator transition of $PrRu_4P_{12}$", Physica B: Condensed Matter **359-361**, 833–835 (2005).

[249]D. Malterre, M. Grioni, P. Weibel, B. Dardel, and Y. Baer, "Temperature Dependence of the 4f Spectral Function in the Kondo System $CeSi_2$: Evidence of the Kondo Resonance Smearing", Europhysics Letters (EPL) **20**, 445–450 (1992).

[250]C. Derks, K. Kuepper, M. Raekers, A. V. Postnikov, R. Uecker, W. L. Yang, and M. Neumann, "Band-gap variation in $RScO_3$ (R=Pr, Nd, Sm, Eu, Gd, Tb, and Dy): X-ray absorption and O K-edge x-ray emission spectroscopies", Physical Review B **86**, 155124 (2012).

[251]M. Raekers, K. Kuepper, S. Bartkowski, M. Prinz, A. V. Postnikov, K. Potzger, S. Zhou, A. Arulraj, N. Stusser, R. Uecker, W. L. Yang, and M. Neumann, "Electronic and magnetic structure of $RScO_3$ (R=Sm,Gd,Dy) from x-ray spectroscopies and first-principles calculations", Phys. Rev. B **79**, 125114 (2009).

[252]P. Blaha, K. Schwarz, G. Madsen, D. Kvasnicka, and J. Luitz, *Wien2k, an augmented plane wave + local orbitals program for calculating crystal properties*, Techn. Universitat Wien, Austria, 2001.

[253]J. Perdew, K. Burke, and M. Ernzerhof, "Generalized Gradient Approximation Made Simple.", Physical review letters **77**, 3865–3868 (1996).

[254]A. D. Becke and E. R. Johnson, "A simple effective potential for exchange", J Chem Phys **124**, 221101 (2006).

[255]F. Tran, J. Kunes, P. Novak, P. Blaha, L. D. Marks, and K. Schwarz, "Force calculation for orbital-dependent potentials with FP-(L)APW plus lo basis sets", Computer Physics Communications **179**, 784–790 (2008).

[256]L. J. Bennett and G. Jones, "The influence of the hubbard u parameter in simulating the catalytic behaviour of cerium oxide", Phys. Chem. Chem. Phys. **6**, 21032–21038 (2014).

[257]L. D. Marks, "Fixed-Point Optimization of Atoms and Density in DFT", Journal of Chemical Theory and Computation **9**, 2786–2800 (2013).

[258]R. T. Haasch, L. W. Martin, and E. Breckenfeld, "Single Crystal Rare-earth Scandate Perovskites Analyzed Using X-ray Photoelectron Spectroscopy: 5. $DyScO_3$ (110)", Surface Science Spectra **21**, 165–172 (2014).

[259]A. Walsh, G. W. Watson, D. J. Payne, R. G. Edgell, J. Guo, P.-A. Glans, T. Learmonth, and K. E. Smith, "Electronic structure of the α and δ phases of Bi_2O_3: A combined ab initio and x-ray spectroscopy study", Phys. Rev. B **73**, 235104 (2006).

[260]Y. Dou, R. G. Egdell, D. S. L. Law, N. M. Harrison, and B. G. Searle, "An experimental and theoretical investigation of the electronic structure of cdo", Journal of Physics: Condensed Matter **10**, 8447 (1998).

[261]W.-H. Yang, D.-S. Hou, C.-Z. Li, H. Fan, and H. Y. Zhang, "$LaAlO_3$ single crystal substrate for epitaxial superconducting thin films", Solid State Communications **75**, 421–424 (1990).

[262]C. B. Azzouz, A. Akremi, M. Derivaz, J. L. Bischoff, M. Zanouni, and D. Dentel, "Two dimensional Si layer epitaxied on $LaAlO_3$ (111) substrate: RHEED and XPS investigations", Journal of Physics: Conference Series **491**, 012003 (2014).

[263]M. Zanouni, C. B. Azzouz, M. Derivaz, D. Dentel, E. Denys, M. Diani, A. Aouni, F. M. Morales, J. M. Manuel, R. Garcia, and J.-L. Bischoff, "Epitaxial growth of Fe islands on $LaAlO_3$ (001) substrates", Journal of Crystal Growth **391**, 121–129 (2014).

[264]L. Hao, Z. Zhang, X. Xie, H. Wang, Q. Yu, and H. Zhu, "Preparation of $SrCoO_x$ thin films on $LaAlO_3$ substrate and their reversible redox process at moderate temperatures", Journal of Crystal Growth **427**, 36–41 (2015).

[265]J. L. Maurice, C. Carretero, M. J. Casanove, K. Bouzehouane, S. Guyard, E. Larquet, and J. P. Contour, "Electronic conductivity and structural distortion at the interface between insulators $SrTiO_3$ and $LaAlO_3$", Physica Status Solidi a-Applications and Materials Science **203**, 2209–2214 (2006).

[266]Ariando, X. Wang, G. Baskaran, Z. Q. Liu, J. Huijben, J. B. Yi, A. Annadi, A. R. Barman, A. Rusydi, S. Dhar, Y. P. Feng, J. Ding, H. Hilgenkamp, and T. Venkatesan,

"Electronic phase separation at the $LaAlO_3/SrTiO_3$ interface", Nature Communications **2** (2011) 10.1038/ncomms1192.

[267]A. Brinkman, M. Huijben, M. van Zalk, J. Huijben, U. Zeitler, J. C. Maan, W. G. van der Wiel, G. Rijnders, D. H. A. Blank, and H. Hilgenkamp, "Magnetic effects at the interface between non-magnetic oxides", Nat Mater **6**, 493–496 (2007).